PRE-PRINT ARTICLE

Global Forest Monitoring

Forest Carbon Diligence: Digital MRV for Jurisdictional and Voluntary Offsets Markets

Christopher B. Anderson[1] | Maxwell B. Joseph[1] | Camile Söthe[1] | Flávia de Souza Mendes[1] | Thomas Maschler[1] | Ryan C. McCarthy[1] | Joseph Mascaro[3] | Tara O'Shea[2] | Amy Rosenthal[1] | David C. Marvin[1]

[1]Planet Labs PBC, San Francisco, CA, USA

[2]Woods Institute for the Environment, Stanford University, Stanford, CA USA

[3]Brown University, Providence, RI, USA

Correspondence
Christopher B. Anderson
Email: christopher@planet.com

Funding information
All funding provided by Planet Labs PBC

Forest Carbon Diligence is a digital MRV system for mapping forest structure and forest carbon over time. This manuscript describes the qualities of the Diligence datasets — annual maps of canopy cover, canopy height, aboveground carbon density, change detection, and their uncertainties — and quantifies performance across multiple MRV contexts. Canopy height and canopy cover regression metrics were high (height $r^2 = 0.83$, cover $r^2 = 0.79$ over NEON), as were aboveground carbon metrics (GEDI L4A $r^2 = 0.64$ at 30 m, GEDI L4B $r^2 = 0.82$ at 1 km). Carbon intercomparisons found strong agreement among 8 independent datasets. Agreement was highest with GEDI, showing strong correlations at multiple scales ($r = 0.92$ for $1km$ comparisons, and $r = 0.98$ for 1°, ecoregion, and national scales). Diligence and CCI were correlated in mid-latitude ($r = 0.89$) and high-latitude ecoregions ($r = 0.88$). Country-level agreement with FAO data was high ($r = 0.76$), as was agreement with field- and project-based carbon estimates from FIA ($r = 0.86$) and CARB ($r = 0.76$). Correlations were lower in pixel-level comparisons at NEON field plots ($r = 0.58$) and in Central Africa ($r = 0.71$), identifying a negative bias in carbon-dense forests. These results demonstrate how Forest Carbon Diligence can support policy and market needs by providing scientific, well-calibrated, and consistent estimates of aboveground forest carbon stocks.

KEYWORDS
Forest Carbon, Earth Observation, Jurisdictional Carbon Markets

Abbreviations: ACD: Aboveground Carbon Density | AGB(D): Aboveground Biomass (Density) | CARB: California Air Resources Board | CCI: ESA Climate Change Initiative | FAO: U.N. Food and Agriculture Organization | FIA: U.S. Forest Inventory and Analysis | GEDI: Global Ecosystem Dynamics Investigation | LiDAR: Light Detection and Ranging | MRV: Measurement, Reporting and Verification | NEON: National Ecological Observatory Network

1 | INTRODUCTION

Land use change accounts for 13-21% of global anthropogenic greenhouse gas emissions, with deforestation responsible for 45% of land use change emissions (IPCC, 2023). These emissions can be mitigated by preventing forest loss, restoring forests in previously degraded landscapes, or altering land management practices, primarily to increase carbon sequestration rates or reduce the probability of high-severity wildfire (Griscom et al., 2017; Marvin et al., 2023). Implementing these natural climate solutions (NCS) at scale requires large financial and institutional investments as well as tools for monitoring their effectiveness. These investments can originate from many sources: jurisdictions like state and national governments; international lending institutions like regional development banks or the World Bank; or private sources like carbon project finance or philanthropic finance (Steckel et al., 2017; Bhandary et al., 2021). In order to quantify both the climate and the financial benefits of these investments, digital MRV technologies that remotely automate or enhance traditional MRV will play a central role in how debtors, creditors, and regulators alike evaluate and justify NCS.

Satellite data are well-positioned to address the primary design goals of digital MRV for NCS. These goals include: 1) assessing the effects of NCS implementations, 2) comparing implementation outcomes across organizations and regions, 3) assessing aggregate action towards shared goals, 4) evaluating alternative implementation designs, 5) facilitating cross-organizational linking, and 6) enabling adaptive learning (Weiner, 2015). Earth observation (EO) satellites provide repeat, spatially continuous, and well-calibrated measurements of the Earth's surface, which can be processed to provide globally consistent maps of the world's forests, and how they are changing. Although many satellite data products have been developed to quantify carbon stocks in the world's forests, few satisfy these MRV design goals.

Methods for mapping global forest structure and aboveground forest carbon with satellites proliferated around 2010 following the launch of ICESAT-GLAS, a spaceborne LiDAR instrument (Wang et al., 2011; Lefsky, 2010; Saatchi et al., 2011; Baccini et al., 2012, 2017; Santoro, 2018). The launches of the multi-modal Copernicus constellation by ESA and of the NASA-GEDI instrument — another spaceborne LiDAR sensor — provided the foundation for the next generation of global models, mapping forests with higher spatial resolution and precision (Dubayah et al., 2020; Potapov et al., 2021; Duncanson et al., 2022; Dubayah et al., 2022b; Lang et al., 2023; Santoro et al., 2023). These new methods have rapidly advanced the field by addressing fundamental technical challenges such as signal saturation, model generalization, and uncertainty characterization (Patterson et al., 2019; Mutanga et al., 2023; Lang et al., 2022; Pauls et al., 2024).

Yet some key technical gaps limit the applicability of these global datasets in MRV contexts. First, there is often little consistency among datasets (Avitabile et al., 2016; Zhang et al., 2019), and between satellite- and field-derived datasets (Mitchard et al., 2014; Réjou-Méchain et al., 2019). Some have interpreted this to suggest that satellites provide near-null predictive power for aboveground carbon mapping (Ploton et al., 2020), while others suggest this represents a general challenge for generating geographically out of distribution model predictions (Meyer and Pebesma, 2022). Few model performance benchmarks and intercomparison results make it difficult to compare carbon stocks across regions and reporters, which rely on an array of data sources like field plots, national forest inventories, and global datasets (Hunka et al., 2023). Second, these global datasets rarely utilize multi-temporal observations to estimate changes in forest structure and carbon over time; data are typically provided for a single time range. Yet, quantifying project outcomes and climate benefits requires measuring change over time (Coffield et al., 2022). This often requires users to reconcile continuous variables with categorical change products, which are produced with different assumptions (Harris et al., 2021). Despite these technical hurdles, satellite data products are still expected to be foundational building blocks for NCS digital MRV (Weiner, 2015; Mitchell et al., 2017).

This manuscript describes a new data product — Forest Carbon Diligence — that was designed to meet the

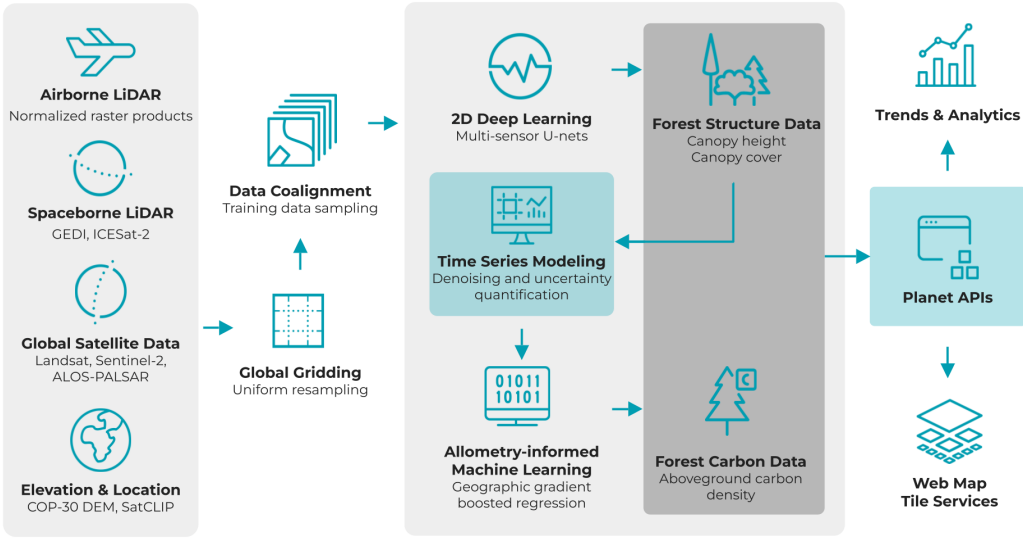

FIGURE 1 Forest Carbon Diligence workflow diagram illustrating the flow of data from source to delivery. Canopy cover, canopy height, and aboveground carbon density metrics used as response data. Multispectral optical data, radar data, elevation data, and location embeddings were sourced as feature data. All datasets were spatially resampled to a global grid. Geographically independent train, validation, and test splits were sampled across the extents of each response dataset. Height and cover samples consist of square patches of data which, co-aligned with satellite feature data, were the inputs to a 2-D U-Net model. AGBD models were fit using spaceborne LiDAR, with modeled canopy cover, canopy height, elevation, and location embeddings as features. AGBD was modeled using gradient boosting regression, then converted from biomass density to carbon density during inference. Pixel-level (30 *m*) uncertainties were quantified for each metric using conformal inference.

digital MRV needs for NCS. Diligence data quantify the density of carbon stored in trees, the area occupied by trees, mean canopy height, and change detections across the terrestrial land surface at a 30 *m* scale on an annual cadence, starting in 2013. These estimates were produced from machine learning models trained on historical satellite observations, airborne LiDAR data, and spaceborne LiDAR data. This manuscript demonstrates the suitability of Diligence data products for jurisdictional and voluntary carbon monitoring applications by conducting a multiscale, multimethod quality assessment using a combination of intercomparison and validation approaches. This medium-resolution, historical carbon product builds the foundation for the next generation of digital MRV technologies.

2 | METHODS

The Forest Carbon Diligence products were created using multiscale, publicly available EO data (Fig. 1). These datasets were modeled in a stepwise process to balance the strengths and limitations of each dataset.

Airborne LiDAR data were used to model forest structure because the relationships between forest structure and satellite feature data were expected to generalize beyond the geographically limited training data. However, there are no globally general methods for estimating woody biomass from airborne LiDAR, as some form of local calibration is required. This means estimating out-of-distribution biomass and its uncertainty is not straightforward. Spaceborne LiDAR data, on

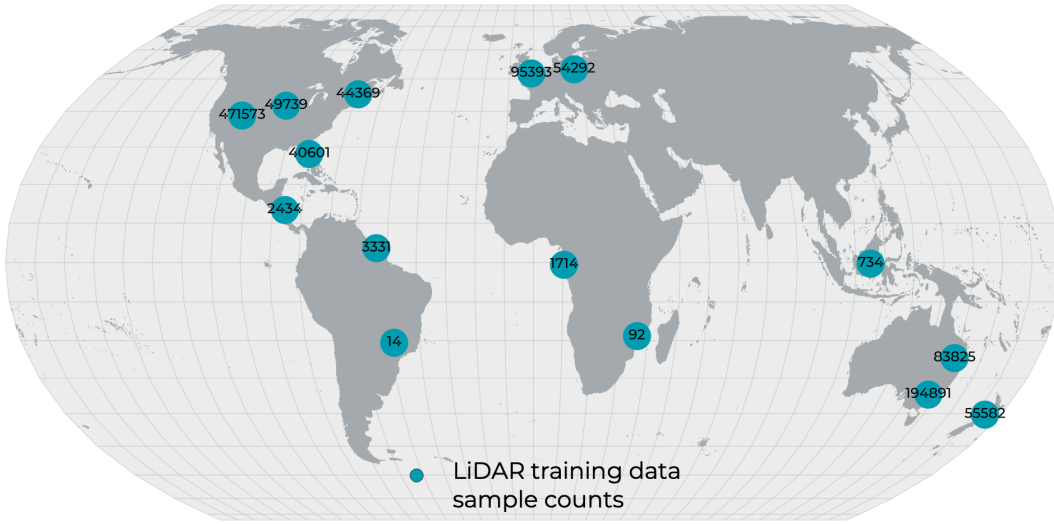

FIGURE 2 Clustered counts of airborne LiDAR samples used in model training, where each sample represents a 128x128 pixel tile. Numerical labels represent the number of samples within a 2,000 km radius of the centroid.

the other hand, provide near-global estimates of aboveground biomass, which were fit using region- and biome-specific equations relating forest structure to biomass (Dubayah et al., 2022b; Montesano et al., 2024).

This method — modeling forest structure from airborne LiDAR, optical, and radar satellite data, then using the estimated structure data to predict biomass — retains the benefits of high-quality, labeled forest structure data and the simplicity of an allometry-informed approach to estimating biomass from structure.

2.1 | SOURCE DATA

2.1.1 | AIRBORNE LiDAR

Point cloud data were accessed from a series of open data sources (Appendix A.1), reprojected to a consistent coordinate system (EPSG:6933) and normalized in the Z dimension to height above ground. Ground point classifications provided in the source data were used for normalization. Buildings, bridges, noise, and other non-vegetation classes were removed from processing using the point classifications provided in the source data, when present. For datasets without prior classifications, custom building and noise classifiers were used. Canopy height and canopy cover were rasterized from the normalized point cloud data at 1 m nominal resolution (see Section 2.2 for grid details). Overall, 2,234,400 km^2 of LiDAR data were processed and extracted for model training and evaluation (Fig. 2).

Canopy height, measured in meters, was calculated as the highest point within each grid cell using a modified pit free canopy height model algorithm (Khosravipour et al., 2014). This calculation is not technically restricted to trees as there is no height or size threshold for inclusion. The height of the tallest vegetation at each grid cell is recorded, be it grass, shrub, or tree.

Canopy cover, also referred to as canopy density in LiDAR contexts, is measured in percent and is calculated as the number of LiDAR returns 5 m and above divided by the total number of returns within each grid cell. This threshold tracks overstory vegetation cover and can be interpreted as a proxy for canopy closure;

cover increases in proportion to overstory branch and foliage volumes. It has also been interpreted as the complement of the canopy gap fraction ($CC = 1 - GF$; Coomes et al. (2017)).

Canopy height and canopy cover rasters were average resampled to 30 m prior to model training, and the pixel values represent the mean canopy height and cover among all $1m$ pixels used in resampling. Average resampling to a coarser resolution reduces the range of values, narrowing the range of observed and predicted canopy height values to approximately $0 - 40$ m. It does not represent the height of the tallest tree within a pixel, and it can include bare ground observations in resampling, meaning the values are typically lower on average than metrics like RH98 or Lorey's height (Fig. 3).

Mean canopy height was selected because it can be consistently retrieved across LiDAR instruments and is directly correlated with aboveground biomass (Asner and Mascaro, 2014) (Section B.1). Metrics derived from vertical profiles like RH80 or mean canopy profile height, in contrast, are highly sensitive to laser power and require additional modeling to ensure consistency across instruments (Lefsky et al., 2002; Ni-Meister et al., 2010; Zhu et al., 2022). Mean canopy height also implicitly weights subcanopy height measurements by crown area, and the combination of height and crown size is highly correlated with aboveground biomass across ecosystems (Jucker et al., 2017).

2.1.2 | SPACEBORNE LiDAR

AGBD estimates from GEDI v2.1 (Dubayah et al., 2022b) and ICESat-2 ATLAS (Montesano et al., 2024) were downloaded, merged, and organized into a harmonized dataset using a global equal area tile grid (see 2.2). These two sources of AGBD estimates are complementary, with overlap, as GEDI provides coverage over mid latitudes (<51.6° N, >51.6° S) and ICESat-2 provides coverage for high latitudes (>44.4° N) (Appendix B.2).

Like all EO data, spaceborne LiDAR data include noise and uncertainty, which vary based on instrument hardware and observation conditions. Recently, methods for identifying the highest-quality GEDI observations have proliferated (Moudry et al. 2024). We applied a series of quality filters to the GEDI observations, selecting observations from power beams, collected at night, excluding steep slopes, and excluding orbits with high geolocation error (Appendix B.2). The ICESat-2 data were filtered for quality by the data providers (Montesano et al., 2024).

An additional outlier filter was applied to the GEDI and ICESat-2 observations. The purpose of this filter was to identify and remove anomalously tall RH98 observations, particularly in sparsely arbored areas.

Overall, 586 million GEDI observations and 15 million ICESat-2 observations were retained after filtering (30% and 99% of the original observations, respectively). A final spatially balanced random sampling step yielded 81.6 million waveforms to be used for training and evaluation, reducing bias in oversampled regions and better approximating a geographically uniform random sample (Meyer and Pebesma, 2022).

2.1.3 | SURFACE REFLECTANCE

Multispectral surface reflectance data provided 6 of the 9 feature bands used for the forest structure models. Surface reflectance is sensitive to vegetation growth and structure patterns, with optical variation driven by a combination of leaf-level and canopy-level growth and structure metrics (Jordan, 1969; Knipling, 1970; Asner, 1998).

The full scene archives of Landsat-8, Landsat-9, Sentinel-2A and Sentinel-2B were downloaded from public cloud storage. Each scene was processed to nadir BRDF-adjusted surface reflectance using the FORCE atmospheric correction and normalization algorithm (Frantz, 2019). FORCE produces a scene-level QA mask classifying cloud, shadow, haze, water, and snow using a modified version of FMask (Frantz et al., 2018; Skakun et al., 2022). Sentinel-2 scenes were average resampled to match Landsat's resolution. To reduce false negative cloud detections, a custom cloud and shadow mask was applied to update each scene's QA mask (Appendix B.3). Only the six bands shared across instruments were retained: [B, G, R, NIR, SWIR-1, SWIR-2].

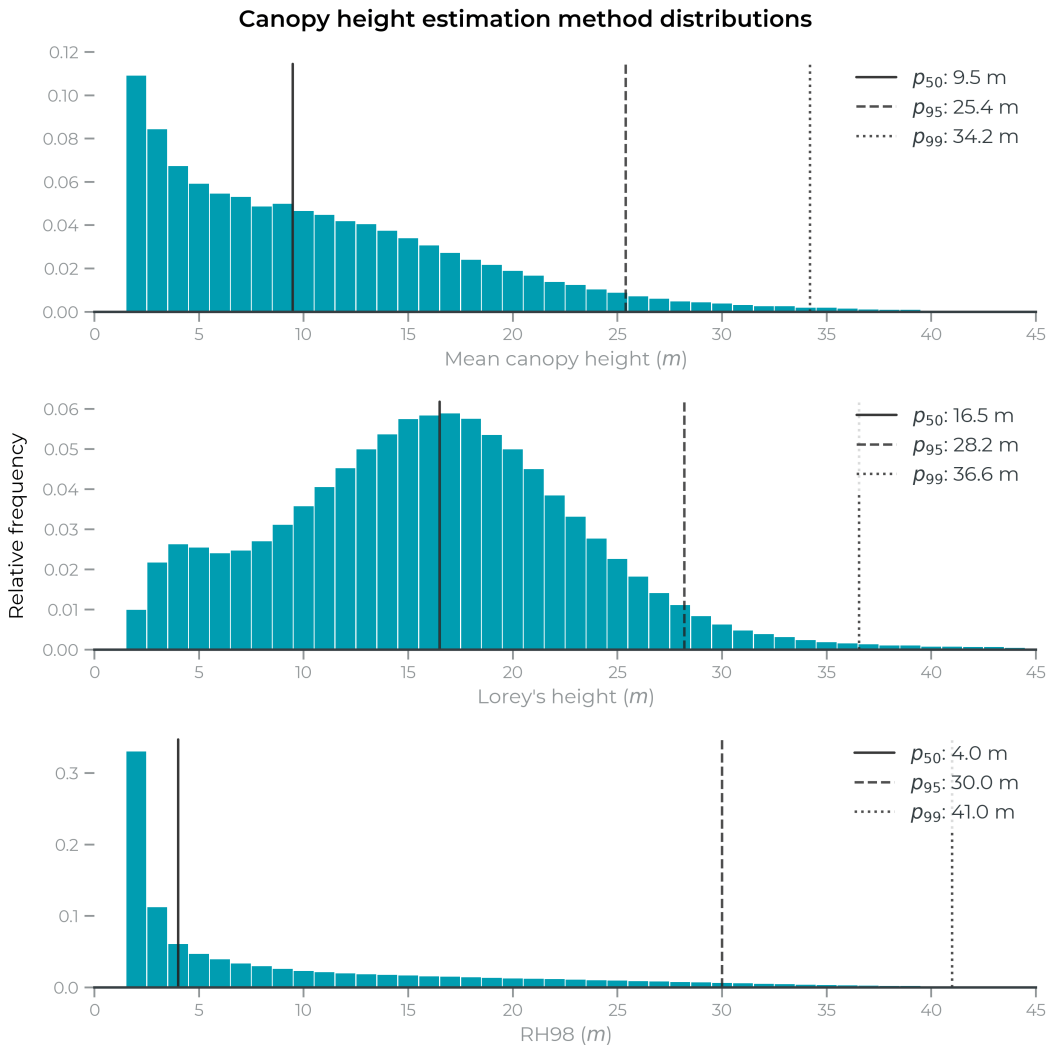

FIGURE 3 Canopy height histograms derived from three measurement approaches. Top: airborne LiDAR-derived mean canopy height. Middle: field-derived Lorey's height. Bottom: spaceborne LiDAR-derived RH98. Mean canopy height values at 30 m resolution are lower than Lorey's height and RH98 values on average. Mean canopy height and RH98 show exponential distributions, representing a more uniform geographic distribution of height values compared to Lorey's height, as field plot locations are often biased towards intact forests (Marvin et al., 2014; Réjou-Méchain et al., 2019). Histograms were computed for all locations with $height \geq 2m$ to remove bare ground. Source data used for the field plots and RH98 values is described in Appendices A.2 and B.2

Annual surface reflectance mosaics were created beginning in 2013, which marks the launch of Landsat-8 (Roy et al., 2014). These mosaics were created using a custom best-available-pixel compositing method, adapted from (White et al., 2014), and described in detail in Appendix B.4. Best-pixel methods show strong

temporal consistency compared to percentile-based composites, though this may come at the expense of radiometric uniformity (Matasci et al., 2018; Qiu et al., 2023).

The pixel composite method addressed three needs. The first was to maximize consistency in the observation conditions for each pixel. The compositor included scoring factors based on sun angle, expected time of peak greenness, distance to clouds, aerosol density, and instrument type. Pixel quality increased as solar elevation increased, at times closest to peak greenness, as aerosol content decreased, and for Sentinel-2 observations over Landsat-8/9 observations. The second goal of the compositor was to provide a quantitative flag for observation quality. Pixel quality scores provide information on the expected reliability of each observation, allowing users to filter or weight observations based on pixel quality. Finally, the compositor records the Julian day of the best pixel, providing a timestamp for when each observation occurred.

2.1.4 | L-BAND RADAR, WOOD DENSITY, AND ELEVATION DATA

Dual polarization mosaics from ALOS-PALSAR-2 L-band SAR (HH and HV) comprised 2 of the 9 total predictor bands used for the forest structure models. Active microwave measurements are directly sensitive to aboveground plant water content. L-band measurements are typically sensitive to the water content of the large woody components of biomass, like tree trunks and branches, indirectly measuring key components of stand-level vegetation structure (Konings et al., 2019; Ottinger and Kuenzer, 2020). L-band backscatter data — HV polarization in particular — are effective in estimating patterns of basal area and aboveground biomass, though the signal appears to saturate in high biomass forests (Mitchard et al., 2009; Bouvet et al., 2018; Williams et al., 2022).

Annual, radiometrically balanced ALOS-PALSAR-2 HH/HV mosaics were accessed directly from JAXA and used without additional transformation, aside from standardizing data types and harmonizing `no data` values across tiles (Shimada et al., 2009). Years 2013 and 2014 were backfilled with 2015 observations since ALOS-2 was launched in 2014, and data were not provided until 2015.

A global map of wood density was the final predictor for the forest structure models. This layer was included as a metric representing plant community biogeography, and is described in Appendix B.5. It was included to model nonstationary relationships between satellite data and forest structure data, which were expected to vary as a function of vegetation type (Hawkins, 2012; Takougoum Sagang et al., 2024). Although a static wood density map was not expected to be a mechanistic predictor of forest structure, it derived a single, ecologically meaningful metric from a series of soil, terrain, and climate variables that are known to drive global variation in canopy height (Liu et al., 2025). Compressing these data into one normalized variable provided contextual ecological information while reducing overfitting risk and reducing runtime.

Elevation data were used as a predictor for the aboveground carbon density model. This allowed the model to learn nonstationary carbon-topography relationships at local and regional scales, capturing fine-scale topoedaphic drivers of carbon storage in slopes and floodplains (Marvin et al., 2014; Taylor et al., 2015; Jucker et al., 2018) and along elevation gradients (Asner et al., 2014a; Malhi et al., 2017; Marifatul Haq et al., 2022). Elevation data were primarily sourced from the Global 30 m Copernicus Digital Elevation Model (European Space Agency and Airbus, 2022). Since this dataset does not include data over Armenia and Azerbaijan, values for those countries were derived from the ALOS World-3D DEM (Tadono et al., 2014).

2.2 | GLOBAL GRIDDING

A multi-scale, hierarchical, global equal area grid system was developed to standardize data storage, processing and analysis. Every map projection includes some form of geographic distortion — in shape, angle, distance, or area — and selecting a global projection requires making tradeoffs regarding which distortions are most tolerable

Grid Level	Decimation	Pixel Size (m)	Rows	Columns
1	1	0.383	19683	19683
2	3	1.149	6561	6561
3	9	3.447	2187	2187
4	27	10.340	729	729
5	81	31.020	243	243
6	243	93.062	81	81
7	729	279.185	27	27
8	2187	837.555	9	9
9	6561	2512.664	3	3
10	19683	7537.991	1	1

TABLE 1 Hierarchical grid specification describing pixel and tile sizes at each level in the 3^n-based nonary tree.

for a given use case. There were four design goals to balance for Diligence:

- Minimize distortions relevant to forest structure and forest carbon mapping
- Minimize data loss when resampling from commonly used data products
- Minimize costs for processing and storage
- Minimize friction between user and data (i.e. does not require bespoke tooling to use)

Following an analysis of multiple conformal and equal area projections, the EASE-Grid 2.0 cylindrical equal area projection projection was selected (Brodzik et al., 2012). An equal area projection satisfied the first criteria because the canopy cover, mean canopy height, and aboveground carbon density datasets are all area-based. Canopy cover estimates the percent area occupied by canopy vegetation in each grid cell. Mean canopy height estimates the average height of all vegetation in a grid cell. The carbon model is area-based — not tree-based (Coomes et al., 2017) — and is normalized to report carbon density in $MgC \cdot ha^{-1}$. Conserving area was more important than preserving shape or distance.

A nonary tree layout was selected, which defines a grid with a base decimation of 3^n. This differs from common quad tree layouts like Web Mercator that are decimated with a base of 2^n. The nonary layout supports hierarchical scale definitions that align with common global satellite data products (Table 1). This minimizes data loss when reprojecting Landsat or GEDI data to grid level 5, for example, and supports exact resampling of LiDAR data from level 2 to level 5. The grid layout specifications are as follows:

- CRS: EPSG:6933
- Projected extent: (-17367530, -27612800, 17367530, 7122260)
- Geographic extent: (-180, NaN, 180, 76)
- Tile shape: 4608x4608
- Internal tile shape: 512x512

The square grid extent was defined by the east-west extent of the EASE-Grid projection. The extent was shifted downward to snap the upper bound of the grid to the 76° northern parallel to maximize the amount of valid pixels (the northern bounds of viable tree cover). The southern bound was extended beyond the valid geographic extent to form a perfect square since the geographic coordinate system represents a rectangular extent. Specifying coordinates south of -90° simply defines a square grid; no data from these areas were produced or analyzed.

This global grid specification provides an efficient layout for processing and storage, requiring 40% fewer pixels than a comparable geographic grid (EPSG:4326), and 50% fewer than a comparable World Mercator grid (EPSG:3395), both of which highly distort area.

2.3 | MODEL TRAINING

Airborne LiDAR provides high-precision measurements of forest structure and has been used to train models from satellite data to map national-scale forest structure using multiscale frameworks (Asner et al., 2014b; Anderson, 2018; Matasci et al., 2018; Takougoum Sagang et al., 2024). Airborne LiDAR has also been used to map aboveground biomass patterns within approximately 10% uncertainty relative to field measurements at a 1 ha scale (Mascaro et al., 2011; Chen et al., 2016). However, public LiDAR data coverage is geographically sparse and biased: opportunistic collections do not representatively sample the plant communities of the world. While there is evidence that a tropics-wide approach to estimating biomass from LiDAR might emerge (Asner et al., 2012), an out-of-distribution analysis found that local calibrations are still required to estimate carbon density from LiDAR (Jucker et al., 2018). This makes airborne LiDAR an untenable training dataset for a global carbon estimation product.

Sparsely sampled but global aboveground biomass data are now available from GEDI and ICESat-2, which are an ideal training data source for a global product. Although optical EO data are often used to directly estimate and upscale biomass predictions over large areas (Asner et al., 2014b; Baccini et al., 2017; Campbell et al., 2021; Valle et al., 2025), others have questioned the feasibility of directly estimating biomass from optical EO data in a way that generalizes geographically (Ploton et al., 2020). The Diligence products address this challenge by first estimating canopy height and canopy cover from satellite data, which has a strong mechanistic basis and a long history in the literature (Lefsky, 2010; Kellndorfer et al., 2010; Simard et al., 2011; Hansen et al., 2013; Potapov et al., 2021), then estimating carbon density as a function of forest structure and topography from a global sample of biomass estimates.

The Diligence approach is therefore grounded in two related assumptions: a) forest structure and topography largely explain spatial patterns of biomass density, and b) the relationships between forest structure, topography, and biomass vary across ecosystems. Canopy height is a critical input to biomass allometry, and model error is typically minimized when region-specific parameters are estimated (Feldpausch et al., 2012; Jucker et al., 2017). For canopy cover, Coomes et al. (2017) found that the canopy gap fraction is highly correlated with basal area. They also found that area-based allometry using canopy height and gap fraction-derived basal area minimized error and bias and outperformed tree-based allometry. Since canopy cover is effectively the complement to gap fraction, it can serve as an effective proxy for basal area and improve biomass predictions when paired with canopy height (Li et al., 2014; Singh et al., 2016).

2.3.1 | CANOPY HEIGHT AND CANOPY COVER MODELS

Deep learning regression models were trained to predict mean canopy height and canopy cover independently at 30 m nominal resolution using surface reflectance, HH/VV backscatter, and wood density data as feature variables, and airborne LiDAR data as response variables. The feature and response variables were normalized to a common range using robust scaling. Forward and inverse transformations were applied on the fly at training and inference time, meaning the input and output data are stored in their natural units.

U-Net convolutional neural network architectures were selected for their robust performance in mapping ecological patterns from EO data (Ronneberger et al., 2015; Brodrick et al., 2019; Kattenborn et al., 2021; Wagner et al., 2023). The base architecture was modified to include dense blocks, ResNet blocks, attention blocks, and a series of network-in-network connections, where each block contained 64 filters (Vaswani et al., 2017; Zeng et al., 2019; Li et al., 2023). L2 kernel regularization ($\alpha = 1e^{-4}$) and 2-D dropout layers ($rate = 0.25$) were used to improve generalization (Phaisangittisagul, 2016). Mean squared error loss was minimized using the Nadam optimizer with a learning rate of $3e^{-4}$ for 30 epochs and a batch size of 32 tiles (Dozat, 2016). Mean absolute error (MAE), root mean squared error ($RMSE$) and coefficient of determination (r^2) scores were calcu-

lated as metrics at runtime, but were not used as loss functions.

Training data were generated by randomly sampling 128x128 pixel tiles from regions with coincident airborne LiDAR data. The year of the satellite data closest to the LiDAR acquisition was used for temporal matching. A total of 1,099,559 samples were extracted at an average sample density of 2 $points \cdot km^{-2}$ using uniform random geographic sampling. Samples were randomly assigned to training/validation sets (67%) or interval calibration/testing (33%) sets. The training/validation data were then randomly split 70/30%, and the interval calibration/testing data were randomly split 20/80%. NEON data were withheld from these sets and used instead for estimating time series model hyperparameters.

Training data were used to fit model parameters. Validation data were used to approximate out of sample predictive performance during training. Interval calibration data were used in conformal inference to generate 90% prediction intervals. Finally, test data were used to evaluate predictive performance.

2.3.2 | TIME SERIES MODELS

Time series analysis with EO data has rapidly evolved in tandem with increased access to standardized data products and cloud computing platforms (Gorelick et al., 2017; Woodcock et al., 2020). Algorithms such as LandTrendr and CCDC simplified change detection, trend analysis, and land cover classification by directly estimating these patterns from multispectral EO, although the algorithms themselves are more general that the multispectral use case (Kennedy et al., 2010; Zhu and Woodcock, 2014; Pasquarella et al., 2022). The Diligence time series model applies similar concepts — identifying trends and changes in forest structure — using the forest structure maps as input instead of the raw EO data. Estimating change parameters for these data, and runtime cost considerations, merited the use of a simple denoising model.

The Diligence U-net models predict height and cover independently for each year, and these predictions contain nonstructural variation related to phenology, illumination, and sensor calibration. This residual prediction variation was minimized using statistical models (Fig. 4). For each pixel, three models were fitted:

- A constant-in-time model, which represents stability
- A spline model, which represents gradual change
- A change point model, which represents fast change

The constant-in-time model assumes that all variation in the predictions is due to noise. This model is expected to perform well when height or cover remains stable over time or when changes are minimal relative to the noise in the predictions (e.g. slow growth that is not detectable over a few years).

The spline and change point models were designed to capture slow and fast changes, respectively. Regularized β-splines were used to estimate nonlinear trends, while the change point model included an additional discrete change point parameter at the timestep with the greatest change in predicted height or cover.

The preferred model for each pixel was selected using Akaike's Information Criteria (AIC). An additional heuristic was applied to reduce noise: if the coefficient of variation (CV) over time for the selected model's predictions is below a threshold, the constant-in-time model was selected. This CV threshold is a hyperparameter tuned along with the AIC threshold. Once a preferred model was selected for each pixel, predictions were generated and standard errors were used to quantify pixel-level uncertainty for height and cover.

The hyperparameters of the time series model were optimized using multiyear airborne LiDAR time series data from NEON DP1.30003.001 product (NEON, 2025). These hyperparameters — regularization λ, degrees of freedom, AIC threshold, and CV threshold — were tuned via Bayesian optimization using Optuna (Akiba et al., 2019). $RMSE$ was minimized for both height and cover, computed across all valid pixels within the NEON time series. Although a categorical objective function evaluating year-to-year change (e.g. cross-entropy loss) would have maximized agreement with fast changes, $RMSE$ maximized agreement with contin-

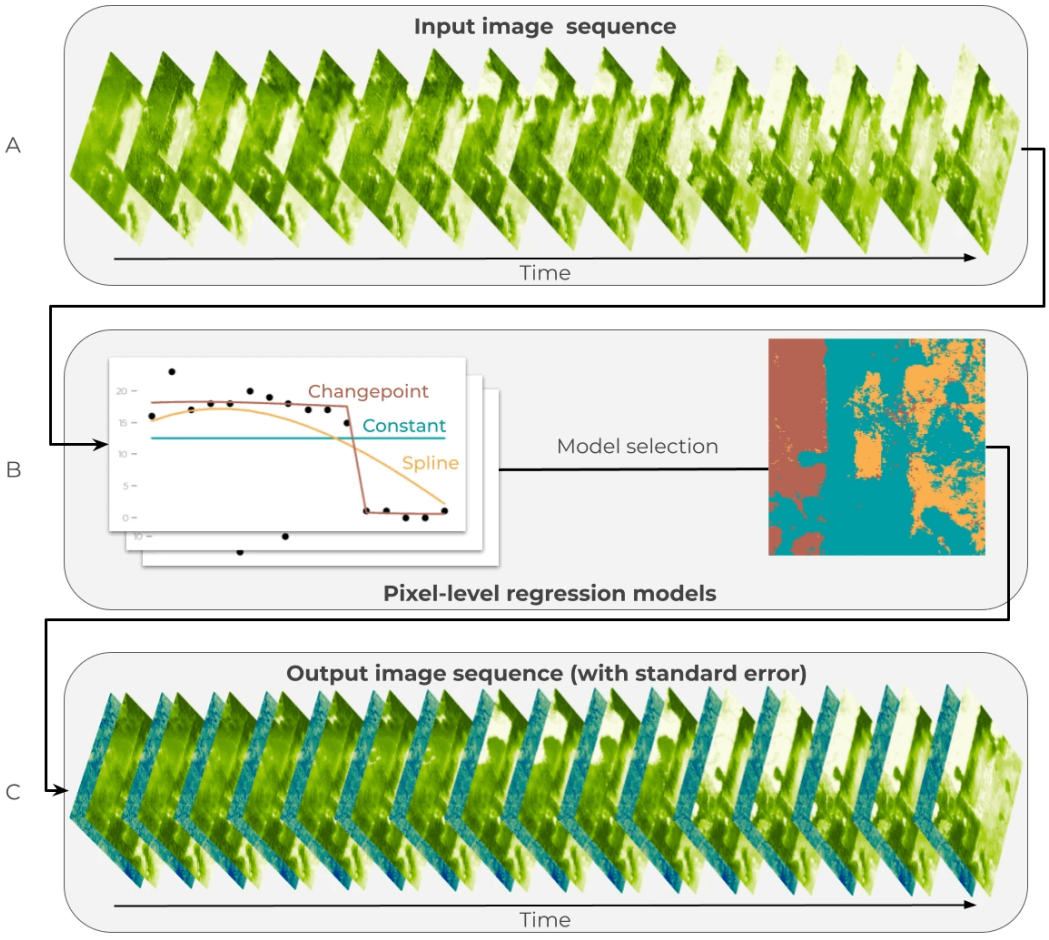

FIGURE 4 Statistical model for estimating canopy height and canopy cover over time. (A) First, a time series is generated from the raw predictions for times $t = 1, \ldots T$. (B) Three linear models are fit for each pixel: a constant model to represent the mean (blue), a change point model to represent sudden change (red), and a spline model to represent gradual change (orange). A model is selected for each pixel using AIC. (C) The preferred model for each pixel is used to generate denoised predictions for each time step: expected values (green color ramp) and standard errors (blue color ramp).

uous height and cover values over the full time series, which is sensitive to loss, growth, and stability.

Time series outputs for each year are provided as an additional data asset, with categorical classes mapping no change, fast change, and gradual change (classes $[0, 1, 2]$, respectively). The quality of the fast-change assets for mapping forest loss is not evaluated in this manuscript, but is described in Söthe et al. (in prep.).

2.3.3 | CANOPY HEIGHT AND CANOPY COVER UNCERTAINTY

Standard errors from the height and cover time series models were used to construct 90% prediction intervals:

$$[y_{pred} - \hat{q} \cdot \sigma_{pred}, y_{pred} + \hat{q} \cdot \sigma_{pred}] \quad (1)$$

Where y_{pred} is a predicted value from the time series model, σ_{pred} is the standard error of the prediction, and $\hat{q}$ is a parameter estimated using withheld data via split conformal inference (Eq. 1).

Split conformal inference uses disjoint partitions of a dataset to produce well-calibrated prediction intervals. These are 90% prediction intervals that contain the true value approximately 90% of the time (Angelopoulos and Bates, 2021).

Interval calibration data, which was 20% of the withheld testing data, were used to estimate $\hat{q}$, a scalar quantity that determines the width of the interval relative to the standard error to achieve 90% coverage. After generating predictions with $\hat{q}$, empirical interval coverage is quantified using the remaining withheld samples.

2.3.4 | ABOVEGROUND CARBON DENSITY MODEL

Light gradient-boosting machine (LightGBM) regression models were trained to predict GEDI L4A and ICESat-2 aboveground biomass as a function of predicted mean canopy height, canopy cover, elevation, and location. Location data was encoded using SatCLIP positional embeddings (Klemmer et al., 2025).

The relationships between forest structure and aboveground biomass vary across plant communities, biomes, and topographic gradients, and these shifting relationships are explicitly encoded in the GEDI L4A biomass algorithm (Jucker et al., 2018; Duncanson et al., 2022; Ma et al., 2023; Kellner et al., 2023). Incorporating location features into a tree-based regression model can represent multiple non-stationary relationships: specifically, between predictors and both the mean biomass density and its associated uncertainty (Hawkins, 2012). This approach captures strong geographic variation in the relationships among vegetation structure, elevation, and aboveground carbon density, allowing region-specific biomass models to be empirically derived from a single global dataset.

10-fold spatial cross validation was used to assess out-of-sample predictive performance, where each of the 7,408 tiles containing GEDI or ICESat-2 biomass estimates was assigned to one of ten partitions (Wenger and Olden, 2012; Meyer and Pebesma, 2022). Furthermore, for each fold, 5% of the training data was randomly withheld for uncertainty calibration.

Model hyperparameters were evaluated using Bayesian optimization of cross-validation $RMSE$ on a random 25% of data. The number of trees, the leaves in each tree, as well as both L1 and L2 regularization were modified. Final hyperparameter selection was additionally informed by visual inspection of predictions and external intercomparisons.

Uncertainty was quantified with conformalized quantile regression, which yielded 90% prediction intervals where interval widths vary nonlinearly as a function of model predictors (Romano et al., 2019). In particular, LightGBM quantile regressors were fit to estimate the 5% and 95% quantiles, then conformalized to obtain prediction intervals with strong coverage guarantees on unseen data (Angelopoulos and Bates, 2021).

Conformalized quantile regression was selected for two reasons. First, nonstationary errors were expected to vary nonlinearly as a function of model inputs, including location. Second, reported uncertainties for footprint-level biomass estimates generally underestimate on-orbit uncertainties that arise from error in relative height estimates (Duncanson et al., 2022). Prediction intervals from conformal inference, in contrast, reflect the empirical distribution of on-orbit data, propagating both measurement- and model-based sources of uncertainty.

Finally, AGBD is converted to ACD by multiplying by the global mean carbon concentration: 0.476 (Martin et al., 2018).

2.3.5 | POST PROCESSING

Estimates of height, cover, and ACD were minimally post-processed using simple heuristics. To reduce low noise, $cover < 5\%$ were set to zero. If canopy cover was zero at both the beginning and the end of the time series, then all annual cover values were set to zero. Where canopy cover was estimated as zero, canopy height and ACD were also set to zero.

2.4 | MODEL EVALUATION

The evaluation framework for this product includes two primary components: withheld data evaluation, and intercomparison. Withheld data evaluation refers to comparisons with samples of directly comparable observations, like airborne or spaceborne LiDAR data. Intercomparison evaluates modeled Diligence estimates against modeled estimates from external sources, like field plots and third party satellite observations. This distinction is particularly important when comparing carbon density or biomass density data.

2.4.1 | FOREST STRUCTURE EVALUATION

One third of the samples from the forest structure training data were withheld from training and used for evaluation ($n = 360,853$ tiles of shape 128x128). Model performance was evaluated using r^2, MAE, and $RMSE$ scores. Because training data were generated using uniform random geographic sampling, and oversampled at high spatial density ($2\ points \cdot km^{-2}$), the testing samples were not always spatially independent of the training samples. These data are thus referred to as withheld samples. Withheld performance metrics are therefore best characterized as training data performance, not as fully independent test validation.

Additionally, LiDAR data from NEON were withheld from regression model training and used to evaluate canopy height and canopy cover predictions. These include measurements over time and across a wide range of forest types in North America (Musinsky et al., 2022). These data were prepared using the standard LiDAR processing pipeline with some additional filtering. NEON site-years with persistent noise were removed using $70\ m$ as a maximum height filter (removing PUUM 2019, MOAB 2019, and REDB 2019 data). The resulting filtered dataset included 55 NEON sites, and 233 site-year pairs. Though excluded from forest structure model training, NEON data should also not be considered fully independent validation data, as these data were used to tune the time series model hyperparameters.

While computing r^2, $RMSE$, and MAE on the full population of withheld data describes global model performance, it may not necessarily describe local-scale performance. This may conceal an effect resembling Simpson's Paradox, where global variance is well-explained while local variance is not (Pearl, 2022). To evaluate how Diligence estimates reflect fine scale ($30\ m$) local variation, we computed site-year level r^2 for canopy height and cover for each NEON site-year. These r^2 values are "unpooled" in the sense that values are computed based on pixels from a single site in a single year. This is in contrast to "pooled" r^2 values, computed using pixels from all NEON sites and years.

Furthermore, the temporal consistency of site-level spatial averages were evaluated at sites with repeat lidar flights to characterize stability over time (Appendix C.1.1).

2.4.2 | ABOVEGROUND CARBON DENSITY EVALUATION

Out-of-sample predictive performance was evaluated using 10-fold spatial cross validation with the spatially-balanced GEDI L4A and ICESat-2 samples, preventing any geographic overlap between the train/val splits. The cross-validation mean and standard deviation of r^2, $RMSE$, MAE, and bias scores were evaluated. For prediction interval evaluation, the interval coverage percentage and mean interval width were evaluated.

ACD predictions were also average resampled and compared to the GEDI L4B data product version 2.1 (Dubayah et al., 2023). The L4B product is a $1\ km$ gridded dataset that uses L4A point estimates as samples to infer the mean and standard error of AGBD within each grid cell. It used a hybrid estimation approach designed to propagate uncertainty from a variety of sources, including sampling density and model parameter variance, providing statistically unbiased estimates of mean AGBD at scale (Patterson et al., 2019). Comparing Diligence predictions to GEDI estimates at both $30\ m$ and $1\ km$ resolutions show how prediction variance can be high at fine scales but decrease with spatial aggregation, matching the scaling dynamics of GEDI products.

2.5 | MODEL INTERCOMPARISONS

Intercomparisons evaluate the level of agreement between Diligence estimates and external estimates of either AGBD or ACD. Aboveground biomass is rarely directly measured, even in the field, and every biomass estimation method includes large uncertainties (Réjou-Méchain et al., 2019). Each method of biomass estimation has its merits and demerits, providing distinct insights into the drivers and distributions of aboveground biomass that should be evaluated. To help users navigate these complexities, a multi-scale, multi-method intercomparison with eight independent, publicly available datasets was performed.

Two notes should frame these comparisons. First, Diligence aboveground carbon estimates are proportional to aboveground biomass estimates based on a constant, the global mean carbon concentration of 0.476 (Martin et al., 2018). This simplifies conversions between biomass and carbon, facilitating intercomparisons against external estimates. Second, these analyses involve comparing two quantities that are both estimated from models, and are both subject to uncertainty. Consistency is primarily quantified using linear correlations (Pearson's r), rather than metrics such as r^2 that require one of the two datasets to be an error-free source of truth.

Some intercomparisons were designed to match recent analyses evaluating the quality of NASA-GEDI biomass predictions (Hunka et al., 2023; Dubayah et al., 2022a; Bruening et al., 2023). This included matching statistical analyses and figure styles. This satisfied two design goals: to provide direct comparisons to high-quality references, and to align the Forest Carbon Diligence product with global efforts to harmonize carbon MRV standards.

2.5.1 | SATELLITE PRODUCTS

Included are comparisons to two near-global, satellite-derived biomass products. First is GEDI L4B, which estimates mean AGBD at a 1 km scale using a sample of L4A waveforms (Patterson et al., 2019; Dubayah et al., 2023). The second is from ESA CCI Biomass version 6.0, using the 1 km resolution AGBD estimates from 2020 to align with the GEDI L4B spatial resolution and observation window of 2019-04 to 2023-03 (Santoro et al., 2023).

Diligence estimates were first compared to GEDI L4B and CCI data at the ecoregion-level, reproducing Hunka et al. (2023). Ecoregions were defined by the Terrestrial Ecoregions of the World dataset (Olson et al., 2001), subset to the ecoregions within the GEDI orbit (51.6° N to 51.6° S). Mean AGB estimates from GEDI L4B, CCI, and Diligence were compared for each ecoregion, as were the fraction of Diligence and CCI 1 km pixels that fell within the GEDI L4B 95% confidence intervals.

This intercomparison was repeated using another biomass dataset specifically calibrated to high-latitude forests, where GEDI does not provide coverage: a boreal forest biomass dataset based on ICESat-2 ATLAS and Harmonized Landsat/Sentinel data from 2020 (Duncanson et al., 2023). This comparison focuses exclusively on estimates north of 44° N, which is the lower latitude limit of the ICESat-2 estimates. Ecoregion averages were compared between Diligence, CCI, and ICESat-2 estimates for ecoregions intersecting the spatial bounds of the ICESat-2 product.

2.5.2 | NATIONAL FOREST INVENTORIES

Mean AGBD was computed at the country level then compared to the FAO Global Forest Resources Assessment and to GEDI L4B (FAO, 2020; Bruening et al., 2023; Armston et al., 2023). Diligence predictions were compared with all countries represented in the FAO report, though GEDI estimates were excluded for high latitude countries. Diligence predictions were sourced from 2020 to match the FAO estimates, while GEDI L4B estimates incorporated observations from the period of 2019-04 to 2023-03.

National forest inventories estimate biomass stocks using a variety of methods defined by each country, and some discrepancies between data sources are expected. These discrepancies can arise due to varying forest/non-

forest definitions, sampling density, and the degree of forest type representation in the GEDI training data, for example (Dubayah et al., 2022a). Nevertheless, comparing mean carbon density per country effectively evaluates the calibration of Diligence carbon estimates to national reporting standards.

2.5.3 | CENTRAL AFRICA AND SOUTH ASIA LiDAR ESTIMATES

Although airborne LiDAR is demonstrably sensitive to AGB, calibrating LiDAR-based models requires high density field sampling and careful error propagation (Réjou-Méchain et al., 2019; Valle et al., 2025). Furthermore, geographic LiDAR coverage is poor in many parts of the world, particularly in the tropics, limiting insights into biomass dynamics in undersampled regions.

Rodda et al. (2024) addressed these issues and recently published a dataset of AGB estimates over 13 sites in Cameroon, Gabon, India, and Thailand. The LiDAR data cover a total of 1,11,650 ha in the humid and dry tropics, and over 1,000 field plots were surveyed for calibration. These data were selected as an intercomparison target because these areas are poorly represented in other evaluation datasets outside of national forest inventories. Diligence data were resampled to 1 ha resolution and compared to the Rodda et al. estimates to evaluate biomass retrieval in the African and South Asian tropics.

2.5.4 | NORTH AMERICA PLOT DATA

Intercomparisons with two networks of plot data in North America — the U.S. FIA program and NEON — were used to evaluate Diligence predictions against dense field inventories of AGB at multiple spatial scales.

An aggregated FIA data product covering the conterminous U.S. combined field inventory data from 2009 to 2019, providing mean AGB estimates over a coarse, tessellated grid of 64,000 ha hexagons (Menlove and Healey, 2021). This product was analyzed because precise locations of FIA plots are withheld due to privacy concerns, and because this product was developed to support satellite- derived biomass validation (Woudenberg et al., 2010; Menlove and Healey, 2020). Mean Diligence AGB was computed over the years 2013 to 2019 to match the FIA time interval, and correlations between Diligence and FIA were computed to match the hex grid analyses by Dubayah et al. (2022a) and Bruening et al. (2023).

To evaluate fine-scale biomass predictions, NEON vegetation structure data were processed to provide plot-level AGB estimates (NEON, 2024). The NEON sampling design has plots of varying sizes — 20x20 m or 40x40 m — with smaller nested subplots. Plots were treated as the unit of analysis and only included large live stems ($\geq$ 10 cm DBH) mapped throughout the entire plot footprint. The biomass of each large stem was computed using allometric equations, summed across the plot, and divided by plot area to estimate AGBD (Gonzalez-Akre et al., 2022).

This analysis is considered an intercomparison because plot-level estimates are not error free, as stem-level biomass values were estimated using allometric regression models. Furthermore, these allometries are not necessarily the same as the allometries used in the GEDI L4 data products. However, these data provide an important comparison to a series of high-quality, independent, externally collected, precisely located field inventory plots.

2.5.5 | VOLUNTARY CARBON MARKET PROJECTS

Voluntary and jurisdictional carbon market standards bodies have not yet aligned on how to adopt remote sensing data for digital MRV. Field measurements are currently required to estimate carbon stocks at the project level; understanding whether remote sensing data can provide similar estimates merits a comparison of field and Diligence data in current offsets projects.

Project-level data was sourced from the California improved forest management offset project database, which includes inventory-derived estimates of initial carbon stocks for improved forest management projects in the CARB cap-and-trade program (Badgely et al.,

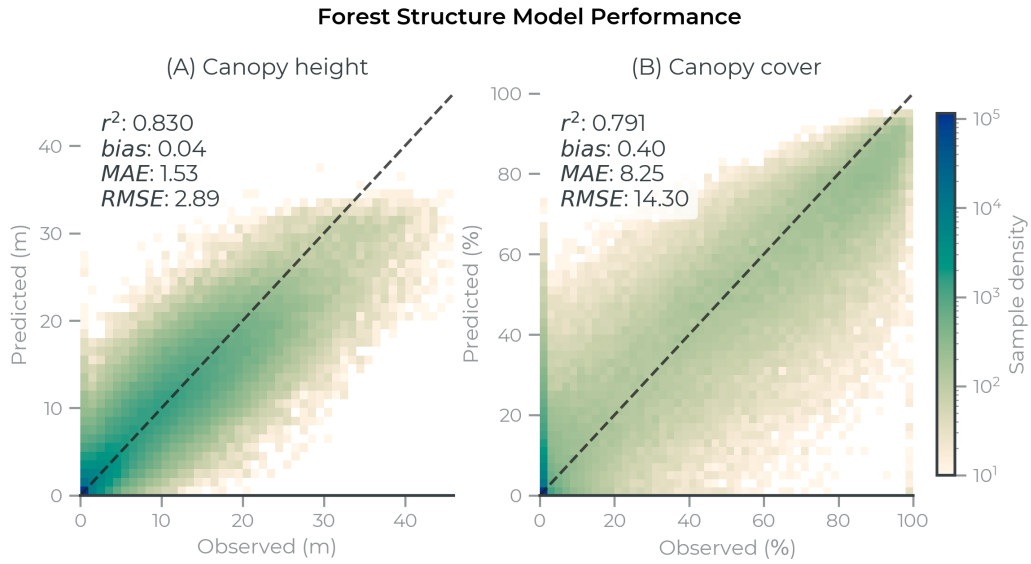

FIGURE 5 Model performance evaluated on withheld samples (n=360,853 tiles) for (A) mean canopy height and (B) canopy cover at 30 m resolution. Performance metrics were computed using the full withheld datasets but the plots were subset to 1 million random samples for visualization.

2021). The initial stock values are provided as estimates of mean CO_2 equivalent density (CO_2e) for 73 unique projects in 21 U.S. states. Although the original database contains 74 projects, one without a start and end date for the initial carbon stock assessment was excluded (ACR458). For each project, CO_2e was estimated from Diligence ACD values, and correlations between CARB and Diligence estimates from the same period were estimated.

3 | RESULTS

3.1 | MODEL EVALUATION

Model evaluation results are summarized below.

3.1.1 | FOREST STRUCTURE EVALUATION

The canopy height model has $RMSE = 2.89m$, $MAE = 1.53m$, $bias = 0.04m$, and $r^2 = 0.830$. The canopy cover model has $RMSE = 14.30\%$, $MAE = 8.25\%$, $bias = 0.4\%$, and $r^2 = 0.791$ (Fig. 5).

For uncertainty estimation, interval coverage of the empirical test set was 90% prediction intervals was 90.12% for canopy height and 90.03% for canopy cover. The $\hat{q}$ parameter — a scaler that widens the standard error of the prediction to ensure coverage — was 3.96 for canopy height and 4.10 for canopy cover. Overall, the mean interval width for canopy height is $8.4m$, and 39.5% for canopy cover.

For NEON, at the $30\ m$ pixel scale, pooling across all sites and years, canopy cover $r^2 = 0.83$ (Fig 6B), and canopy height $r^2 = 0.76$ (Fig 6D). Spatially averaging across sites reveals strong agreement between observed and estimated mean canopy cover ($r^2 = 0.93$, Fig 6A) and mean canopy height ($r^2 = 0.89$, Fig 6C). Diligence estimates are systematically lower for pixels with the highest values, and this negative bias persists even when averaging spatially to compute mean canopy height and mean canopy cover (Fig 6A, C).

On average, for any one site in any one year, a lower

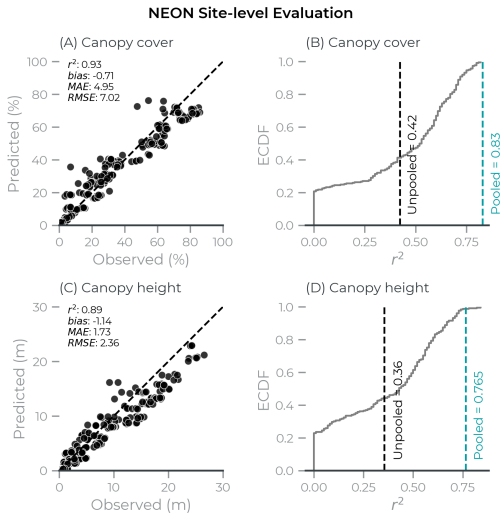

FIGURE 6 Site-level evaluation of mean canopy cover and canopy height across all NEON site-years.

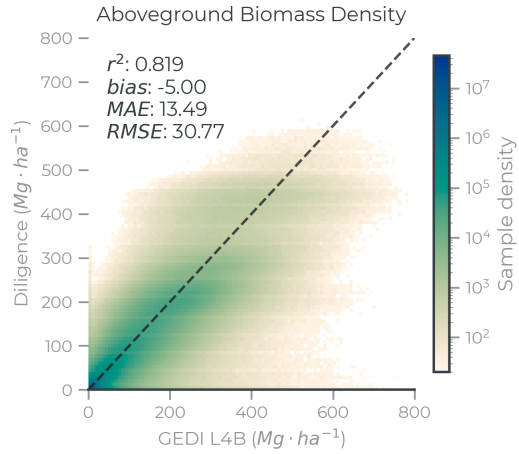

FIGURE 7 Aboveground biomass model performance evaluated against GEDI L4B data at 1 km resolution. A minimum of 20 points per grid cell were used for visualization.

fraction of local variation is explained than what might be expected based on pooled r^2 values. Mean unpooled canopy cover r^2 = 0.42, compared to a pooled r^2 = 0.83 (Fig. 6B). The mean among site years of unpooled canopy height r^2 = 0.36, compared to a pooled r^2 = 0.76 (Fig. 6D). This analysis shows how global metrics can diverge from local metrics, highlighting that within-region variance is generally harder to explain than among-region variance (Meyer and Pebesma, 2022).

3.1.2 | ABOVEGROUND CARBON DENSITY EVALUATION

Based on 10-fold geographic cross validation, the aboveground biomass model has a mean $RMSE$ = 55.27 $Mg \cdot ha^{-1}$ (sd = 2.18), mean MAE = 24.2 $Mg \cdot ha{-}1$ (sd = 0.87), mean $bias$ = −0.06 $Mg \cdot ha^{-1}$ (sd = 0.39), and a mean r^2 = 0.638 (sd = 0.01). Uncertainty estimation showed empirical interval coverage on withheld data was 92.07%, and the mean interval width is 100.9 $Mg \cdot ha^{-1}$.

Comparing mean aboveground biomass density at 1 km against GEDI L4B — which statistically aggregates L4A footprints and is not independent from the training data — reports model performance scores of $RMSE$ = 30.77 $Mg \cdot ha^{-1}$, MAE = 13.49 $Mg \cdot ha^{-1}$, mean $bias$ = −5.0 $Mg \cdot ha^{-1}$, and r^2 = 0.819 (Fig. 7). Further resampling to 1° grid cells shows strong agreement between Diligence and GEDI L4B (r = 0.98, $bias$ = −5.0 $Mg{\cdot}ha^{-1}$, $RMSE$ = 14.03 $Mg \cdot ha^{-1}$, MAE = 8.37 $Mg \cdot ha^{-1}$) but maps spatial patterns of disagreement, particularly in montane regions (Appendix C.1.3). These results demonstrate the benefits of spatial aggregation, reducing noise in both the model predictions and the L4A footprints.

3.2 | MODEL INTERCOMPARISONS

Model intercomparison results are summarized below.

3.2.1 | SATELLITE PRODUCTS

At the ecoregion level, Diligence, CCI, and GEDI L4B AGB estimates are all highly correlated (Fig. 8). Diligence is positively correlated with CCI AGB (r = 0.89) and with GEDI L4B (r = 0.98), and shows low over-

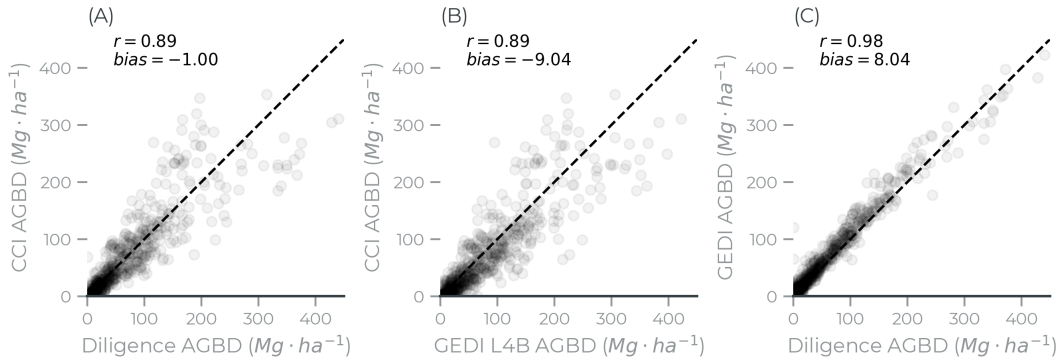

FIGURE 8 Ecoregion-level correlation plots between Diligence, CCI, and GEDI L4B. Each point is an ecoregion. Correlations are quantified as the Pearson correlation coefficient. The x and y variables change in each plot, and mean bias is quantified as the mean of $y - x$. (A) CCI biomass estimates have a 1 $Mg \cdot ha^{-1}$ negative bias compared to Diligence and (B) a 9 $Mg \cdot ha^{-1}$ negative bias compared to GEDI L4B. (C) This shows a positive bias in the GEDI L4B data compared to both datasets (8 $Mg \cdot ha^{-1}$ compared to Diligence).

all bias compared to each dataset (−1 $Mg \cdot ha^{-1}$ for CCI, 8 $Mg \cdot ha^{-1}$ for GEDI L4B). Geographically, both Diligence and GEDI estimates are mostly higher than CCI estimates in east and southeast Asia, the U.S., and southern Mexico. They are lower than CCI estimates in Canada and in the South American and Central African tropics (Fig. 9A, 9B).

Diligence estimates are slightly lower than GEDI L4B estimates in several regions, which is consistent with the slight negative overall bias (Fig. 8C). This trend is particularly apparent in montane ecoregions, likely due to terrain filtering during training data preparation (Appendix 2.1.2), which reduces systematic bias on steep slopes (Kutchartt et al., 2022).

Ecoregions with higher biomass tended to have a higher fraction of Diligence and CCI biomass estimates falling within the GEDI L4B 95% confidence interval (Appendix C.1.2). However, overall a fairly small fraction of Diligence and CCI values fell within the L4B 95% CI: just 28% for Diligence and 21% for CCI. Coverage was particularly low over non-forested regions. This may be due to the relatively narrow confidence intervals of the L4B product in grid cells with low sample density, or to the lack of error propagation in the relative height estimates (Patterson et al., 2019; Duncanson et al., 2022).

In high latitudes, both Diligence and CCI values were higher on average than the ICESat-2 derived estimates (Fig. 10). When evaluating the intersection of valid pixels across datasets, ecoregion-level correlations between ICESat-2 derived estimates and Diligence and CCI were both high ($r = 0.84$ and $r = 0.80$, respectively). The Diligence and CCI ecoregion means were also highly correlated ($r = 0.88$), such that the relative ordering of high vs. low biomass ecoregions was similar across all three data products. In addition, Diligence and ICESat-2 means were closer on average ($RMSE = 32.95\ Mg \cdot ha^{-1}$, $MAE = 24.03\ Mg \cdot ha^{-1}$) than CCI and ICESat-2 means ($RMSE = 40.66\ Mg \cdot ha^{-1}$, $MAE = 26.51\ Mg \cdot ha^{-1}$).

3.2.2 | NATIONAL FOREST INVENTORIES

At the country level, Diligence estimates are highly correlated with GEDI L4B estimates ($r = 0.98$ Fig. 11), and both Diligence and GEDI L4B show similar correlations with the FAO estimates for the year 2020 ($r = 0.75$ and $r = 0.76$, respectively). A table with country-level estimates is provided in Supplemental Table 4.

Four notable outliers are worth mentioning. Dili-

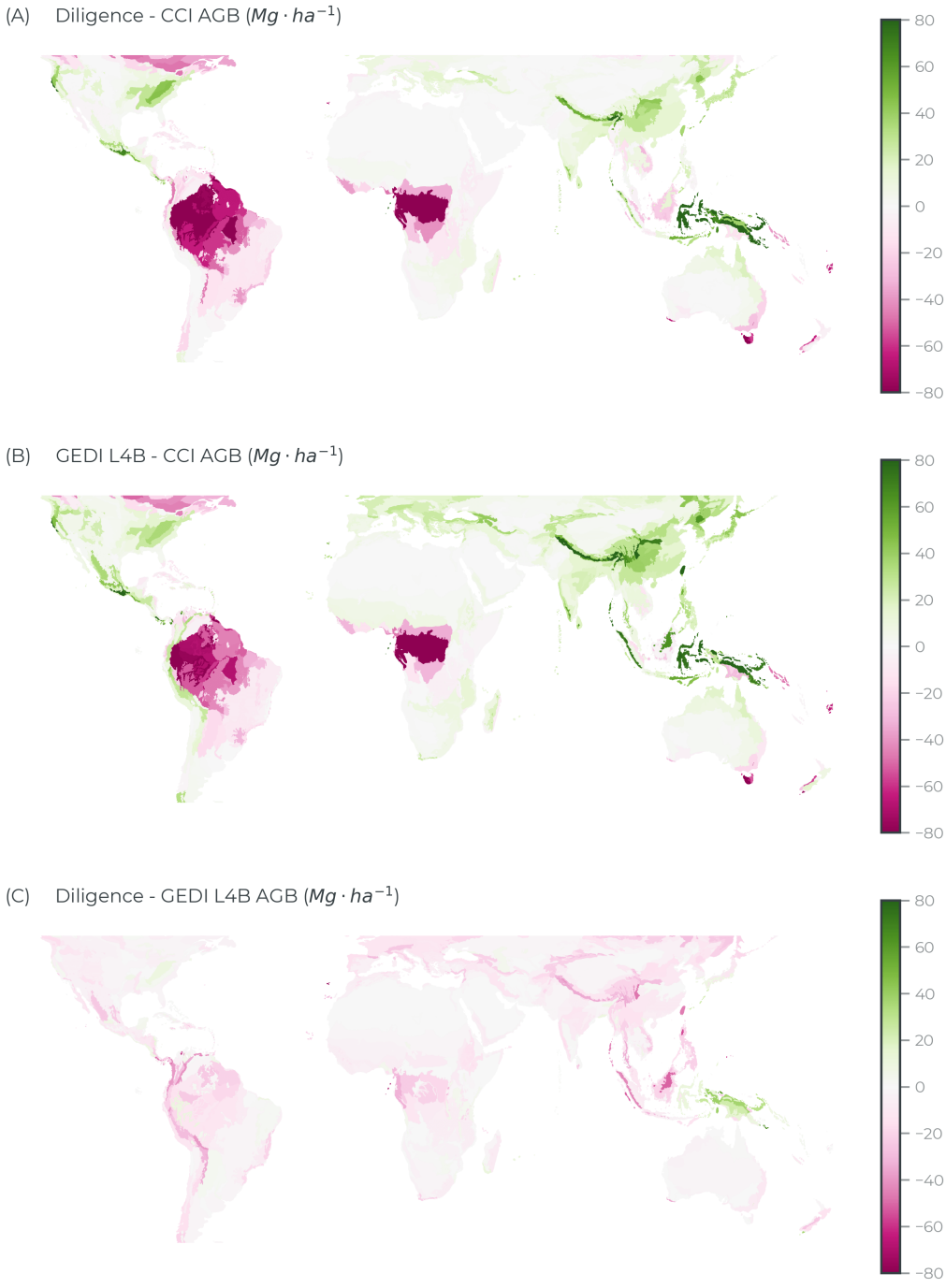

FIGURE 9 Differences in ecoregion-average AGBD between Diligence, CCI, and GEDI L4B. CCI Biomass values are systematically higher across the Amazon and Congo Basin ecoregions but lower in the Asian Paleotropics and the Himalayas (A, B). Diligence predictions show high overall agreement with GEDI L4B (C), mapping lower predictions that are consistent with the slight negative mean bias compared to L4B (Fig. 7).

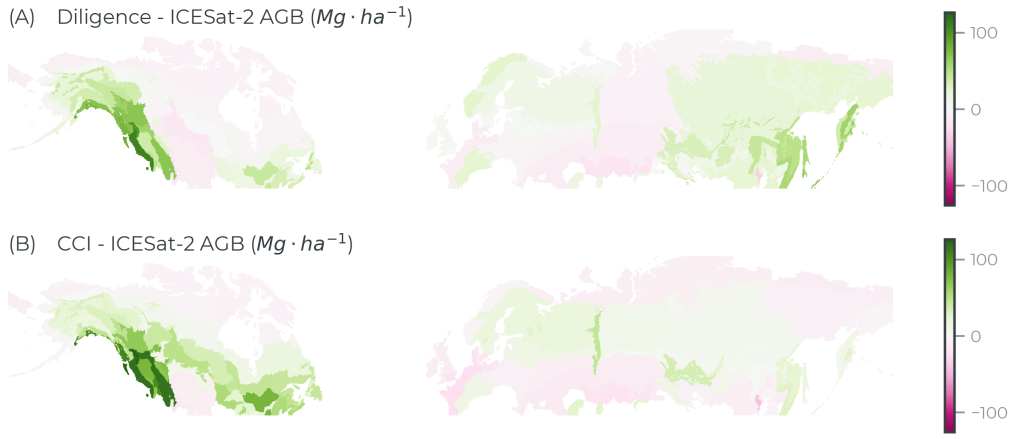

FIGURE 10 Differences in ecoregion-average AGBD between Diligence, CCI, and ICESat-2. (A) Difference between Diligence and ICESat-2 derived estimates. (B) Difference between CCI and ICESat-2 biomass. Both Diligence and CCI biomass estimates were higher in the high biomass regions of the Pacific Northwest, and lower in very high latitudes.

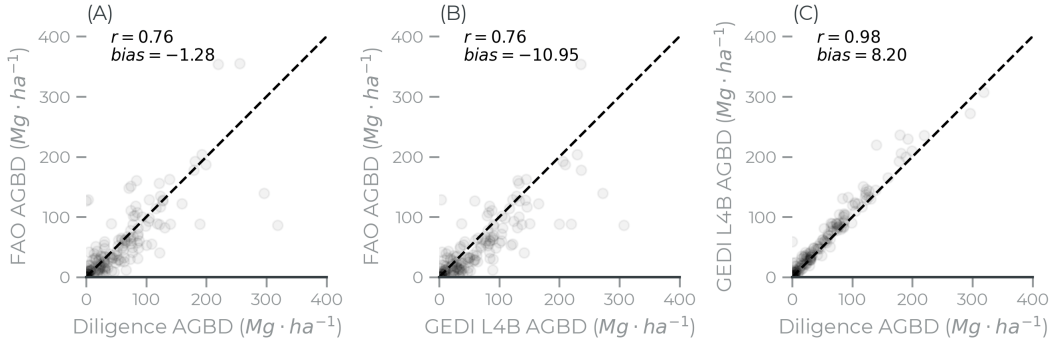

FIGURE 11 Country-level mean AGBD for the year 2020. Each point represents one country. Correlations are quantified as the Pearson correlation coefficient. The x and y variables change in each plot, and mean bias is quantified as the mean of $y - x$. (A) FAO biomass estimates have a 1.28 $Mg \cdot ha^{-1}$ negative bias compared to Diligence and (B) a 10.95 $Mg \cdot ha^{-1}$ negative bias compared to GEDI L4B. On average, Diligence and GEDI L4B estimate slightly higher carbon stocks than FAO national inventories, which often exclude non-forest lands.

gence estimates are much higher than FAO estimates in Indonesia, Papua New Guinea, and the Solomon Islands, predicting around 75% higher than the national average. This is consistent with the high residual differences between Diligence and GEDI and CCI in southeast Asia (Figure 12). Diligence estimates are much lower than FAO for the other two outliers, Guyana and Suriname. These are dense, forested countries in the carbon-rich Guyana shield region of the northern Amazon. Although Diligence show this region is one of the most carbon-dense in the world, the FAO AGBD estimates are more than twice as dense as Diligence estimates.

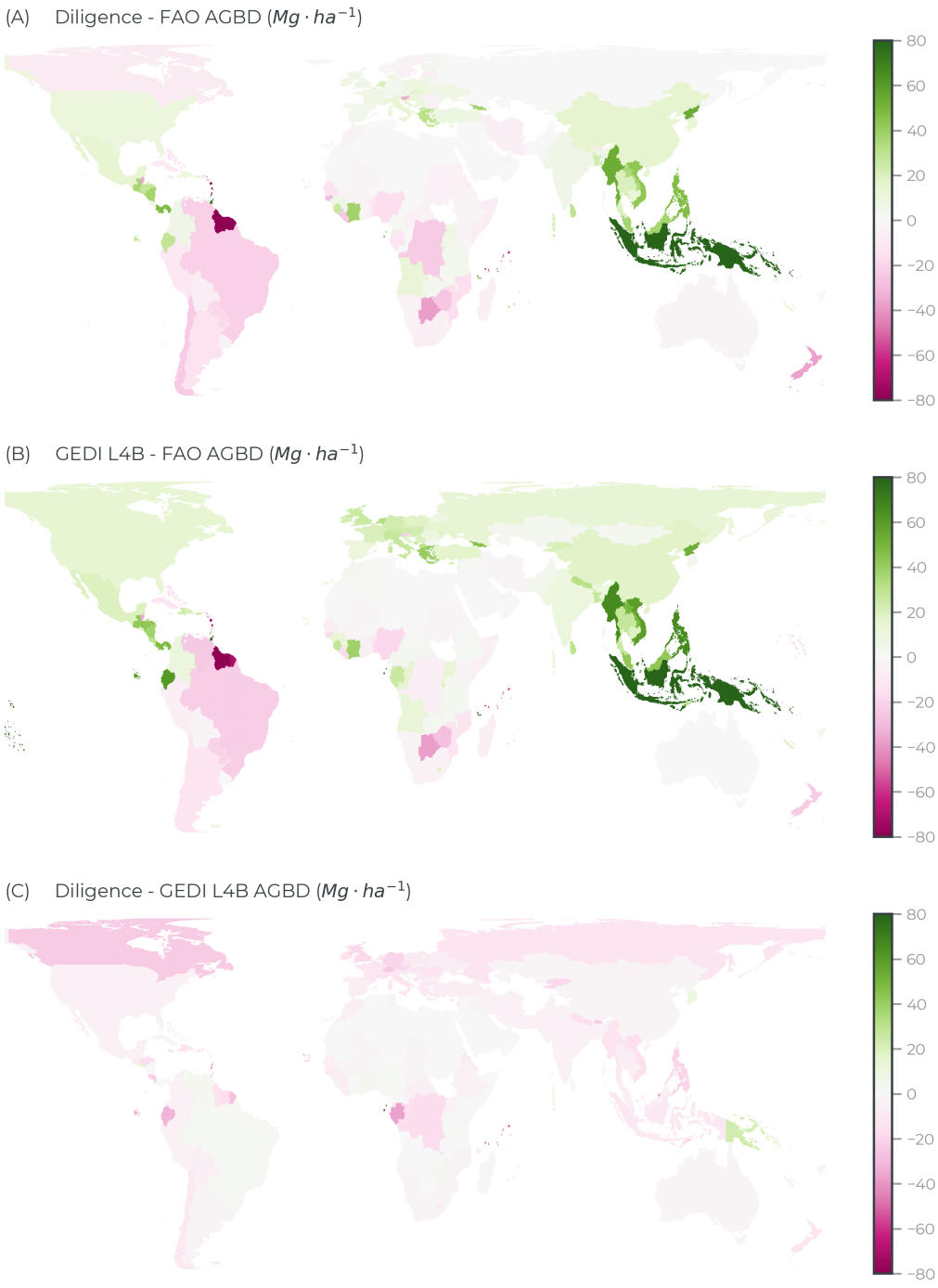

FIGURE 12 Differences in country-average AGBD between Diligence, FAO, and GEDI L4B. The direction of differences with FAO estimates are often directionally consistent across Diligence and GEDI estimates (A, B). Canada and Russia are notable anomalies, but these comparisons are incomplete because GEDI only makes measurements over a small fraction of land area in these countries. Country-level Diligence estimates are lower than GEDI in most cases, which is consistent with the finding that Diligence estimates have lower overall bias relative to FAO (C).

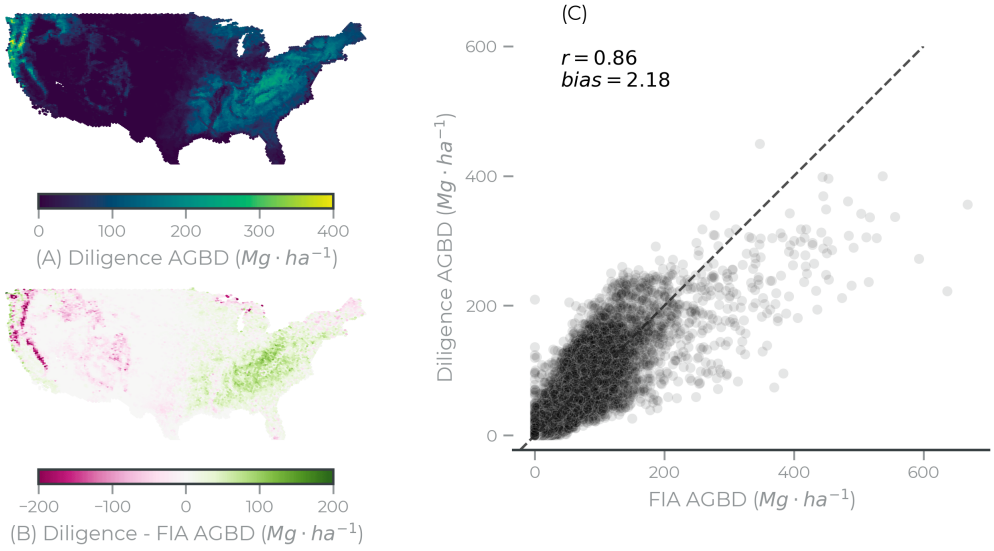

FIGURE 13 Comparison of mean aboveground biomass estimates from Diligence (A) and from the difference between Diligence and FIA (B). Estimates were aggregated to the FIA hexagon grid, where each hexagon is 64,000 ha in area. (C) Scatterplot of FIA vs. Diligence estimates, where each point represents one hexagon.

3.2.3 | CENTRAL AFRICA AND SOUTH ASIA LiDAR ESTIMATES

Predictions across Central Africa and South Asia (Fig 14A) showed a strong negative bias compared to LiDAR-derived estimates (Rodda et al., 2024). Site-level averages show strong positive correlation ($r = 0.93$) but a systematic negative bias ($bias = -88.9\ Mg$; Fig. 14B). These patterns persist at the pixel scale, showing positive correlations when pooled among all pixels ($r = 0.71$; Fig. 14C) with systematic negative bias ($bias = -87.3\ Mg$). Site-level analysis found lower unpooled correlations ($r = 0.5$), consistent with other results from densely sampled high-resolution data (Fig. 6, Fig. 15). Site-level correlations are explored in Appendix C.2.2.

The negative bias compared to LiDAR is consistent with the CCI results (Fig. 9). Diligence predictions are lower than CCI in Central Africa, where 8 of the 13 sites are located. This may also be consistent with the FAO intercomparison results, where Diligence estimates (192.4 $Mg \cdot ha^{-1}$ mean AGBD) are lower than the national inventory estimates for Gabon (203.8 $Mg \cdot ha^{-1}$ mean AGBD). However, the differences compared to FAO are much smaller, representing a -5.6% bias.

3.2.4 | NORTH AMERICAN PLOT DATA

Gridded FIA biomass estimates provide a dense, statistically representative sample of forests over a very large area. Overall agreement between FIA and Diligence estimates was high ($r = 0.86$), showing a small positive bias overall ($bias = 2.18\ Mg \cdot ha^{-1}$). Geographically, Diligence estimates tended to be systematically higher than FIA throughout much of the eastern U.S., particularly in Appalachia, and lower in western montane forests of the Sierra Nevada and Cascades ranges (Figure 13). These results are consistent with the findings in Bruening et al. (2023), who reported similar correlations ($r^2 = 0.81$) and a slightly higher mean bias ($bias = 10.48$) when comparing GEDI to FIA.

Diligence data were also compared to multi-year field plot estimates of AGBD from NEON, sourced from a network of sites across the U.S. (Fig. 15A). Overall, there is positive correspondence between plot-level estimates

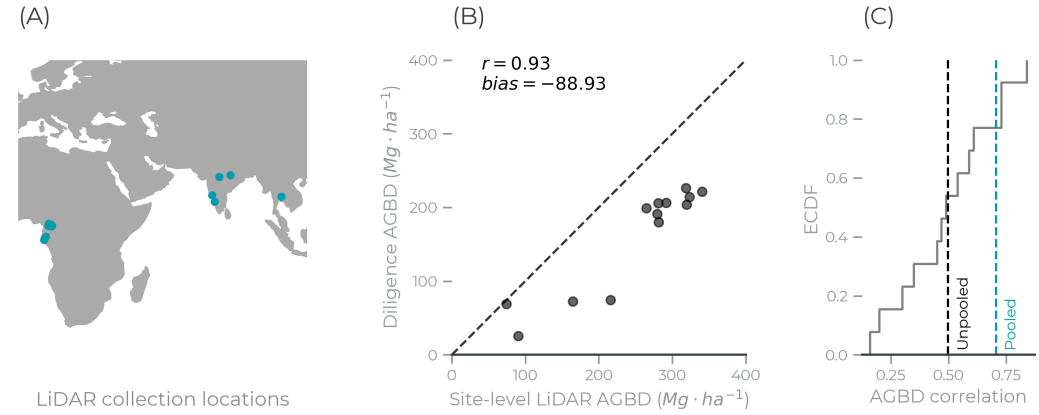

FIGURE 14 (A) Map of LiDAR collections in Cameroon, Gabon, India, and Thailand from Rodda et al. (2024). (B) Site-level correlations for the 13 LiDAR sites with field-calibrated AGBD. Bias is quantified as the mean values of Diligence minus LiDAR AGBD estimates. (C) Empirical cumulative distribution function for site-level correlations, with dashed lines indicating the overall value computed by pooling all sites together (blue) and the mean of unpooled site-level correlations (black)

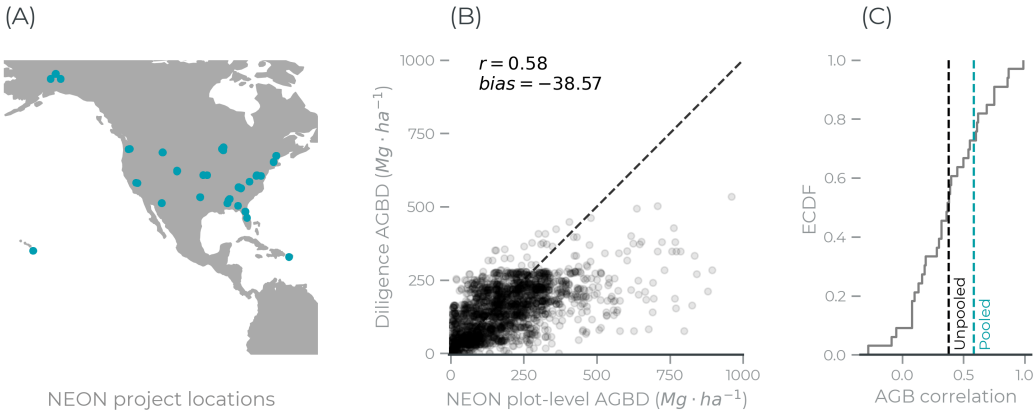

FIGURE 15 Map of NEON field plot locations in the U.S. (blue dots). (B) Field-derived aboveground biomass estimates (x-axis) and Diligence aboveground biomass estimates (y-axis), with a dashed 1:1 line. Each point is one NEON vegetation plot. (C) Empirical cumulative distribution function for site-level correlations, with dashed lines indicating the overall value computed by pooling all sites together (blue) and the mean of unpooled site-level correlations (black).

of aboveground biomass and Diligence estimates ($r = 0.59$, $bias = -38.57\ Mg \cdot ha^{-1}$; Figure 15B). The average site-level correlation between field-derived estimates and Diligence estimates was weaker than the pooled correlation among all sites ($r = 0.41$; Figure 15C), providing additional evidence that within-region variance is generally harder to explain than among-region variance (Fig. 6). Site-level correlations are further explored in Appendix C.2.1.

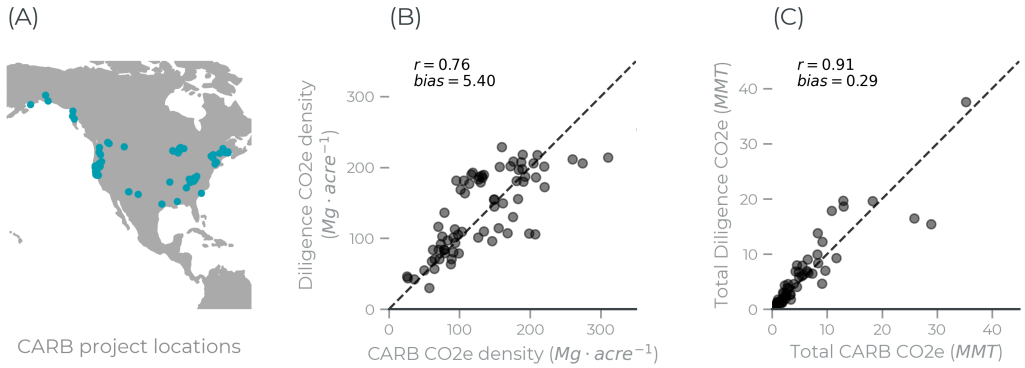

FIGURE 16 Map of CARB project centroids. (B) Project-level comparison of mean CO_2e ($Mg \cdot acre^{-1}$) between field-derived initial stock CARB values (x-axis) and Diligence derived estimates (y-axis). (C) Comparison of project-level initial stock CO_2e in units millions of metric tons (MMT) between CARB and Diligence derived estimates.

3.2.5 | VOLUNTARY CARBON MARKET PROJECTS

Diligence estimates are positively correlated with inventory-derived, project-level estimates of mean CO_2e ($r = 0.76$) with a small positive bias. Accounting for the area of each project, Diligence and CARB total CO_2e estimates are highly correlated ($r = 0.91$) and mean bias remains low ($bias = 0.29 MMT$).

Of the 73 Improved Forest Management projects, 22 projects (20.1%) of Diligence estimates were within 10% of the field-derived total stocks. Of those that fell outside of the 10% threshold, 35 (47.9%) were overestimated and 16 (21.9%) were underestimated by Diligence. There does not appear to be a pattern driven by project size (as measured by total stocks) or geography that determined whether Diligence overestimated or underestimated total carbon stocks (Appendix C.2.3).

4 | DISCUSSION

4.1 | DESIGNING FOR DIGITAL MRV

Forest Carbon Diligence provides annual data on aboveground carbon density, canopy cover, canopy height, and change. This multisensor fusion approach to forest mapping provides the central building blocks for forest carbon MRV (Weiner, 2015; Griscom et al., 2017), using multiple public EO missions to estimate forest carbon stocks as a function of changes in forest structure.

While new EO instruments and data products will continue to evolve and reduce measurement uncertainty, historically available data are critical for evaluating baseline carbon stocks and expected change rates over reference areas. Few upcoming products will cover the full land surface, provide consistent measurements over time with versioned releases, and with a 10+ year historical window. Forest Carbon Diligence data meet all of these requirements.

It will be critical to cross-calibrate novel carbon monitoring systems — like the ESA Biomass mission or high-resolution carbon estimates from nanosatellites — with historical EO data in order to reduce uncertainties in both past and future carbon estimates. The Diligence multi-sensor fusion approach combines data from multispectral, radar, and LiDAR instruments, providing a model for how to integrate technology systems to continuously improve spaceborne carbon estimations with well-calibrated uncertainty.

4.2 | CALIBRATION & UNCERTAINTY

Estimating forest carbon stocks is an inherently uncertain process for nondestructive methods, both in the

field and from EO. Even a perfect volumetric reconstruction of a forest with exact species identifications for every individual, an ill-posed problem itself (Mayr, 2004; De Queiroz, 2007), will still include uncertainty from variation in intraspecific wood density. Accepting imperfection means accepting that all field and EO methods will include varying levels of uncertainty when estimating the core components of forest carbon — wood volume and wood density — since they all rely on proxy variables like basal area, RH98, vegetation type, or mean canopy height. Each method makes trade-offs between precision, speed, cost, and scale. Terrestrial, airborne, and spaceborne LiDAR measurements represent this gradient, for example, with decreasing precision accommodated by increasing geographic coverage.

While spaceborne carbon estimation may have higher uncertainty at fine spatial scales, this does not mean that high uncertainty persists at all scales. Aggregating pixels over larger areas — field plots, carbon projects, protected areas, or states, for example — systematically decreases uncertainty when estimating the standard error of the mean or of the sum of total carbon stocks. What is most critical is that uncertainty measurements are well-calibrated; that multiple sources of uncertainty are propagated to the prediction intervals; that the spatial distribution of errors is quantified; and that any comparison between projects or between time periods robustly tests for differences based on this aggregated uncertainty.

Forest Carbon Diligence uses conformal inference to estimate pixel-level prediction intervals since these intervals reflect the empirical distribution of on-orbit GEDI/ICESat-2 data, propagating both measurement- and model-based sources of uncertainty. Prediction intervals are typically wide as a result, with the mean interval width estimated at 100.9 $Mg \cdot ha^{-1}$. High local uncertainty should be expected. Diligence predicts carbon density based on a series of proxy variables — mean canopy height and mean canopy cover, itself a proxy for basal area — which are derived from optical and radar satellite data. Precision will almost always be lower than field or airborne LiDAR carbon estimates at fine scales. Thus, estimates must be aggregated over larger areas to defensibly test for differences in carbon stocks (Valle et al., 2025).

Since there is no single error-free forest carbon estimation method, and an array of different methods are used in practice, another design goal for Diligence was to develop a carbon product that has low overall bias but high correlations among methods. Low overall bias does not mean low bias everywhere — bias may be high in any given area, such as negative bias in Central Africa and South Asia ($-88\ Mg \cdot ha^{-1}$; Fig. 14) or positive bias compared to CARB data ($+5.4\ Mg \cdot ha^{-1}$; Fig. 16). However, estimates of global carbon stocks and carbon fluxes are likely well-calibrated and representative of the land system as a whole. Areas with strong bias but high correlations such as Central Africa ($r = 0.71$) indicate that using local data to recalibrate Diligence estimates will help align the global product to local contexts. This may not address the problem of signal saturation in very high biomass forests (Appendix C.2.2), but the high uncertainty due to saturation will be empirically represented by wider prediction intervals (Romano et al., 2019).

Since GEDI and ICESat-2 were the calibration targets, Diligence generally propagates the biases of these products. The FAO country-scale intercomparisons found both Diligence and GEDI estimate higher carbon stocks in Ecuador, Indonesia, and Papua New Guinea than national estimates, and lower carbon stocks in French Guiana, Surinam, and New Zealand, for example (Fig. 12). This was also true for fine-scale patterns. Intercomparisons with NEON field plots found moderate correlations ($r = 0.58$) and negative bias ($-38.57\ Mg \cdot ha^{-1}$), while another study performed the same analysis with GEDI L4A data found a similar correlation ($r = 0.65$) and negative bias ($-31.65\ Mg \cdot ha^{-1}$) (Jia et al., 2024). Correlations between Diligence and CCI/FAO matched the correlations between GEDI and CCI/FAO, but overall bias was lower compared to these targets (Diligence $bias = 1.0$ to CCI, $bias = 1.8\ Mg \cdot ha^{-1}$ to FAO, while GEDI $bias = 10.0$ to CCI, $bias = 10.9\ Mg \cdot ha^{-1}$ to FAO), which is probably the result of filtering out noisy waveforms (Fig. 8, Fig. 11).

Spaceborne LiDAR data are valuable beyond providing a well-calibrated sample of forest carbon data across

the terrestrial biosphere. These data are also freely available for users to independently verify the claims in this manuscript, to recalibrate carbon models over specific regions, or to estimate downstream regression coefficients (Lu et al., 2024). Furthermore, advances in forest carbon science from new GEDI/ICESat-2 releases can flow into future Diligence versions, providing version provenance for each release. This level of transparency and commitment to adhering to global standards will be critical to advance interoperability among carbon monitoring systems.

4.3 | JURISDICTIONAL CARBON REPORTING

The Intergovernmental Panel on Climate Change Greenhouse Gas (IPCC GHG) inventory guidelines specify two methods for estimating changes in terrestrial carbon stocks from land use, land use change, and forestry (LULUCF).

First is the gain-loss method, where the net carbon stock change is estimated separately for emissions (carbon released to the atmosphere) and for removals (carbon sequestered by the biosphere). Emissions are estimated by multiplying activity data — the amount of forest area lost, gained, or maintained (ha) — by emission or removal factors relevant to each activity type ($tC \cdot ha^{-1}$). The net flux is the difference between total emissions and total removals. Second is the stock-difference method, where carbon stocks are measured by repeated inventories. The net flux is then estimated as the difference in stocks between inventories (Eggleston et al., 2006; Gibbs et al., 2025).

Forest Carbon Diligence data can support both gain-loss and stock-difference accounting. Gain-loss approaches can estimate initial carbon stocks using the ACD data, and the categorical change data — which estimates canopy cover lost, gained, or maintained — can be used to estimate annual activity data. Stock difference approaches can compute the difference in total carbon stocks between years after propagating uncertainties to estimate fluxes.

Each approach has benefits and limitations, and it is ultimately the prerogative of jurisdictions to select the reporting method that best represents their nationally determined contributions (NDCs) under IPCC guidelines. Forest Carbon Diligence was developed to support jurisdictional MRV by providing the foundational building blocks of data that can be tailored to the reporting requirements of each jurisdiction. However, IPCC-compliant flux estimates are not available off-the-shelf. Gain-loss approaches, for example, require additional emissions and removals data, and stock-difference methods would benefit from local calibration with National Forest Inventories (Pascual et al., 2025).

Future work with Diligence will focus on translating the core data sets to align with multiple jurisdictional reporting methods. This includes the ART-TREES carbon accounting reporting standard, which credits emissions reductions at the national and sub-national levels, and provides technical guidelines for integrating remote sensing data to estimate emissions and removals in accordance with IPCC GHG guidelines.

4.4 | VOLUNTARY OFFSET MARKETS

Directly estimating carbon stocks with EO technologies is currently not well supported by major carbon project developers or standards bodies. Proposals for integrating remote sensing typically require strong agreement with field plots. But rigid accuracy thresholds, such as requiring EO estimates to fall within 10% of field estimated carbon stocks, set a high bar for data producers to meet. It is not clear whether any current or future satellite-derived carbon maps will reach this level of agreement with field measurements. Even disagreements between field-based allometric models can exceed 10%, meaning that different field-based plot estimation methods would not meet such strict requirements (Clough et al., 2017; Réjou-Méchain et al., 2019).

Considering the expected uncertainties and biases of global carbon estimation — like geographic bias and prediction uncertainty — how might a standard best support the use of direct carbon estimation from EO? Using field data to recalibrate a global product to local conditions, quantifying the uncertainty of that calibration,

then testing that carbon fluxes can be reliably estimated net of uncertainty would be one straightforward solution. This was the basic approach of a recent proposal released for public comment from carbon crediting program ACR (ACR, 2025).

Establishing clear guidelines for quantifying project-level uncertainty, and ensuring that net changes must exceed prediction uncertainty, seems a promising and generic approach that could support multiple carbon estimation methods from EO. Projects that quantify carbon stocks using high-precision measurements, like terrestrial or airborne LiDAR, will estimate stocks with lower uncertainty, verify net fluxes over smaller areas, and will likely issue more credits — with higher upfront collection costs. Spaceborne estimation methods can estimate carbon stocks with lower precision and higher uncertainty, which means more area under management will be required and larger net gains will need to occur for credits to be issued. But this will come at lower upfront costs to developers.

The highly uncertain nature of forest carbon estimation merits the inclusion of multiple methods for estimating carbon stocks and fluxes. Credit issuance should reward rigor and precision, and also acknowledge that precision can change at different scales. Satellite carbon estimates may not currently estimate statistically significant carbon fluxes at the 30 m scale, but it should indeed be possible to detect significant changes with aggregation and thorough uncertainty quantification.

4.5 | ENVIRONMENTAL REGULATIONS AND DEFORESTATION MONITORING

Environmental regulations such as the EU Deforestation Regulation (EUDR) require companies to monitor and report deforestation linked to the supply chains of seven commodities, including mandated geolocation and forest status verification of source materials starting on December 31, 2020. The Diligence products provide key indicators for deforestation monitoring, including canopy cover and canopy cover change detection data. These products show strong alignment with reference LiDAR data (canopy cover r^2 = 0.79 for withheld data, r^2 = 0.83 for NEON data), making them valuable tools for compliance and due diligence. Evaluating the Diligence canopy cover change data was out of scope for this manuscript, but shows strong change detection performance compared to multiple benchmarks (Söthe et al. in prep.).

Diligence can support EUDR compliance by enabling annual assessments of canopy cover within sourcing areas, even in mixed-use and high-risk landscapes (Berger et al., 2025). Canopy height and carbon density estimates may also help differentiate forests from tree-crop commodities in tropical regions, given their distinct structural patterns, although this remains under exploration. While pixel-level saturation may affect estimations of the upper tails of canopy height and aboveground carbon density, this effect is much weaker for canopy cover (Fig. 5, Fig. 6). And while regional discrepancies with inventory data (e.g., in Indonesia or the Congo Basin) highlight the need for harmonized definitions, Diligence's consistent global coverage is ideal for EUDR risk screening and enforcement, providing a scalable layer for environmental due diligence, though not replacing field verification.

5 | CONCLUSIONS

Forest Carbon Diligence provides wall-to-wall maps of forest structure, forest carbon, forest change, and uncertainty at 30 m resolution annually over a 10+ year period. It was designed to support digital MRV needs for a variety of natural climate solutions, including jurisdictional carbon monitoring, voluntary carbon markets, environmental regulations, and deforestation monitoring. Model intercomparisons showed that Diligence data estimate carbon stocks with high correlations and low bias when compared to eight independent datasets from around the world.

Global, medium-resolution maps of forest structure, forest carbon, and forest change were identified as essential and aspirational products for global land surface mapping, and Forest Carbon Diligence seeks to meet the

needs and vision articulated by Radeloff et al. (2024). This paper advances the best practices for EO data providers to benchmark forest carbon data products via intercomparison, a critical need for aligning global carbon estimates (Hunka et al., 2023, 2024), and sets a new standard for quality assessment of canopy structure and forest carbon data products.

ACKNOWLEDGMENTS

These results describe version 1.3 of the Forest Carbon Diligence product. The authors thank Hemali Majithia, Jesus Martinez Manso and Pariya Pourmouhommadi for their contributions to the team during the development of this work. Thank you to Niels Andela, Phil Platts, and other colleagues for their feedback on prior version releases, whose feedback greatly improved the product. The findings and views described herein do not necessarily reflect those of Planet Labs PBC.

CONFLICT OF INTEREST

Forest Carbon Diligence is a commercially available product provided by Planet Labs PBC. The authors are current or former employees, as well as shareholders, of Planet Labs PBC. Joseph Mascaro is presently a contributor to the GEDI Competed Science Team, and Tara O'Shea is presently a contributor at the Woods Institute for the Environment; their primary contributions to this work occurred during their times at Planet Labs PBC.

REFERENCES

3DEP (2025) Applications & Visualization Services | U.S. Geological Survey. URL: https://www.usgs.gov/the-national-map-data-delivery/applications-visualization-services.

ACR (2025) Framework for Remotely Sensed Quantification of Forest Carbon. URL: https://acrcarbon.org/methodology/framework-for-remotely-sensed-quantification-of-forest-carbon/.

Akiba, T., Sano, S., Yanase, T., Ohta, T. and Koyama, M. (2019) Optuna: A Next-generation Hyperparameter Optimization Framework. In *Proceedings of the 25th ACM SIGKDD International Conference on Knowledge Discovery and Data Mining*.

Anderson, C. B. (2018) Biodiversity monitoring, earth observations and the ecology of scale. *Ecology Letters*, **21**, 1572–1585. URL: https://onlinelibrary.wiley.com/doi/10.1111/ele.13106.

Angelopoulos, A. N. and Bates, S. (2021) A Gentle Introduction to Conformal Prediction and Distribution-Free Uncertainty Quantification. URL: https://arxiv.org/abs/2107.07511. Publisher: arXiv Version Number: 6.

Armston, J., Dubayah, R., Healey, S., Yang, Z., Patterson, P., Saarela, S., Stahl, G., Duncanson, L., Kellner, J., Pascual, A. and Bruening, J. (2023) Global Ecosystem Dynamics Investigation (GEDI)GEDI L4B Country-level Summaries of Aboveground Biomass. URL: https://daac.ornl.gov/cgi-bin/dsviewer.pl?ds_id=2321. Artwork Size: 0 MB Medium: CSV Pages: 0 MB Version Number: 1.

Asner, G. P. (1998) Biophysical and Biochemical Sources of Variability in Canopy Reflectance. *Remote Sensing of Environment*, **64**, 234–253. URL: https://linkinghub.elsevier.com/retrieve/pii/S0034425798000145. Publisher: Elsevier BV.

Asner, G. P., Anderson, C. B., Martin, R. E., Knapp, D. E., Tupayachi, R., Sinca, F. and Malhi, Y. (2014a) Landscape-scale changes in forest structure and functional traits along an Andes-to-Amazon elevation gradient. *Biogeosciences*, **11**, 843–856. URL: https://bg.copernicus.org/articles/11/843/2014/. Publisher: Copernicus GmbH.

Asner, G. P., Knapp, D. E., Martin, R. E., Tupayachi, R., Anderson, C. B., Mascaro, J., Sinca, F., Chadwick, K. D., Higgins, M., Farfan, W., Llactayo, W. and Silman, M. R. (2014b) Targeted carbon conservation at national scales with high-resolution monitoring. *Proceedings of the National Academy of Sciences*, **111**. URL: https://pnas.org/doi/full/10.1073/pnas.1419550111.

Asner, G. P. and Mascaro, J. (2014) Mapping tropical forest carbon: Calibrating plot estimates to a simple LiDAR metric. *Remote Sensing of Environment*, **140**, 614–624. URL: https://linkinghub.elsevier.com/retrieve/pii/S003442571300360X.

Asner, G. P., Mascaro, J., Muller-Landau, H. C., Vieilledent, G., Vaudry, R., Rasamoelina, M., Hall, J. S. and van Breugel, M. (2012) A universal airborne LiDAR approach for tropical forest carbon mapping. *Oecologia*, **168**, 1147–1160. URL: http://link.springer.com/10.1007/s00442-011-2165-z.

Avitabile, V., Herold, M., Heuvelink, G. B. M., Lewis, S. L., Phillips, O. L., Asner, G. P., Armston, J., Ashton, P. S., Banin, L., Bayol, N., Berry, N. J., Boeckx, P., De Jong, B. H. J., DeVries, B., Girardin, C. A. J., Kearsley, E., Lindsell, J. A., Lopez-Gonzalez, G., Lucas, R., Malhi, Y., Morel, A., Mitchard, E. T. A., Nagy, L., Qie, L., Quinones, M. J., Ryan, C. M., Ferry, S. J. W., Sunderland, T., Laurin, G. V., Gatti, R. C., Valentini, R., Verbeeck, H., Wijaya, A. and Willcock, S. (2016) An integrated pan-tropical biomass map using multiple reference datasets. *Global Change Biology*, **22**, 1406–1420. URL: https://onlinelibrary.wiley.com/doi/10.1111/gcb.13139.

Baccini, A., Goetz, S. J., Walker, W. S., Laporte, N. T., Sun, M., Sulla-Menashe, D., Hackler, J., Beck, P. S. A., Dubayah, R., Friedl, M. A., Samanta, S. and Houghton, R. A. (2012) Estimated carbon dioxide emissions from tropical deforestation improved by carbon-density maps. *Nature Climate Change*, **2**, 182–185. URL: https://www.nature.com/articles/nclimate1354.

Baccini, A., Walker, W., Carvalho, L., Farina, M., Sulla-Menashe, D. and Houghton, R. A. (2017) Tropical forests are a net carbon source based on aboveground measurements of gain and loss. *Science*, **358**, 230–234. URL: https://www.science.org/doi/10.1126/science.aam5962.

Badgely, G., Freeman, J., Hamman, J. J., Haya, B. and Cullenward, D. (2021) California improved forest management offset project database. URL: https://zenodo.org/record/4630684.

Berger, K., Herold, M. and Szantoi, Z. (2025) Earth observation as enabler for implementing the EU regulation on deforestation-free products. *npj Climate Action*, **4**, 68. URL: https://doi.org/10.1038/s44168-025-00276-9.

Bhandary, R. R., Gallagher, K. S. and Zhang, F. (2021) Climate finance policy in practice: a review of the evidence. *Climate Policy*, **21**, 529–545. URL: https://www.tandfonline.com/doi/full/10.1080/14693062.2020.1871313.

Boettiger, C., Thomas, Q., Laney, C. and Lunch, C. (2025) *neonstore: NEON Data Store*. URL: https://github.com/cboettig/neonstore.

Bouvet, A., Mermoz, S., Le Toan, T., Villard, L., Mathieu, R., Naidoo, L. and Asner, G. P. (2018) An above-ground biomass map of African savannahs and woodlands at 25 m resolution derived from ALOS PALSAR. *Remote Sensing of Environment*, **206**, 156–173. URL: https://linkinghub.elsevier.com/retrieve/pii/S0034425717306053.

Brodrick, P. G., Davies, A. B. and Asner, G. P. (2019) Uncovering Ecological Patterns with Convolutional Neural Networks. *Trends in ecology & evolution*, **34**, 734–745. URL: http://dx.doi.org/10.1016/j.tree.2019.03.006. Publisher: Elsevier.

Brodzik, M. J., Billingsley, B., Haran, T., Raup, B. and Savoie, M. H. (2012) EASE-Grid 2.0: Incremental but Significant Improvements for Earth-Gridded Data Sets. *ISPRS International Journal of Geo-Information*, **1**, 32–45. URL: https://www.mdpi.com/2220-9964/1/1/32.

Bruening, J., May, P., Armston, J. and Dubayah, R. (2023) Precise and unbiased biomass estimation from GEDI data and the US Forest Inventory. *Frontiers in Forests and Global Change*, **6**, 1149153. URL: https://www.frontiersin.org/articles/10.3389/ffgc.2023.1149153/full.

Bühlmann, P. and Yu, B. (2003) Boosting With the L_2 Loss: Regression and Classification. *Journal of the American Statistical Association*, **98**, 324–339. URL: http://www.tandfonline.com/doi/abs/10.1198/016214503000125.

Campbell, J. B. (2011) *Introduction to Remote Sensing*. New York London: The Guilford Press, fifth edition edn.

Campbell, M. J., Dennison, P. E., Kerr, K. L., Brewer, S. C. and Anderegg, W. R. (2021) Scaled biomass estimation in woodland ecosystems: Testing the individual and combined capacities of satellite multispectral and lidar data. *Remote Sensing of Environment*, **262**, 112511. URL: https://linkinghub.elsevier.com/retrieve/pii/S0034425721002315.

Chave, J., Coomes, D., Jansen, S., Lewis, S. L., Swenson, N. G. and Zanne, A. E. (2009) Towards a worldwide wood economics spectrum. *Ecology letters*, **12**, 351–366. URL: http://dx.doi.org/10.1111/j.1461-0248.2009.01285.x.

Chen, Q., McRoberts, R. E., Wang, C. and Radtke, P. J. (2016) Forest aboveground biomass mapping and estimation across multiple spatial scales using model-based inference. *Remote Sensing of Environment*, **184**, 350–360. URL: https://linkinghub.elsevier.com/retrieve/pii/S0034425716302802.

Clough, B. J., Curzon, M. T., Domke, G. M., Russell, M. B. and Woodall, C. W. (2017) Climate-driven trends in stem wood density of tree species in the eastern United States: Ecological impact and implications for national forest carbon assessments. *Global Ecology and Biogeography*, **26**, 1153–1164. URL: https://onlinelibrary.wiley.com/doi/10.1111/geb.12625.

CMS (2025) Carbon Monitoring System (CMS). URL: https://daac.ornl.gov/cgi-bin/dataset_lister.pl?p=33.

Coffield, S. R., Vo, C. D., Wang, J. A., Badgley, G., Goulden, M. L., Cullenward, D., Anderegg, W. R. L. and Randerson, J. T. (2022) Using remote sensing to quantify the additional climate benefits of California forest carbon offset projects. *Global Change Biology*, **28**, 6789–6806. URL: https://onlinelibrary.wiley.com/doi/10.1111/gcb.16380.

Coomes, D. A., Dalponte, M., Jucker, T., Asner, G. P., Banin, L. F., Burslem, D. F., Lewis, S. L., Nilus, R., Phillips, O. L., Phua, M.-H. and Qie, L. (2017) Area-based vs tree-centric approaches to mapping forest carbon in Southeast Asian forests from airborne laser scanning data. *Remote Sensing of Environment*, **194**, 77–88. URL: https://linkinghub.elsevier.com/retrieve/pii/S0034425717301098.

Dalagnol, R., Galvão, L. S., Wagner, F. H., de Moura, Y. M., Gonçalves, N., Wang, Y., Lyapustin, A., Yang, Y., Saatchi, S. and Aragão, L. E. O. C. (2023) AnisoVeg: anisotropy and nadir-normalized MODIS multi-angle implementation atmospheric correction (MAIAC) datasets for satellite vegetation studies in South America. *Earth System Science Data*, **15**, 345–358. URL: https://essd.copernicus.org/articles/15/345/2023/.

De Queiroz, K. (2007) Species Concepts and Species Delimitation. *Systematic Biology*, **56**, 879–886. URL: https://academic.oup.com/sysbio/article/56/6/879/1653163. Publisher: Oxford University Press (OUP).

DEFRA (2025) Defra Survey Data Download. URL: https://environment.data.gov.uk/survey.

Disney, M., Burt, A. and Tymen, B. (2018) Weighing trees with lasers project: terrestrial laser scanner data; French Guiana, Cayenne, Nouragues Nature Reserve plot site. URL: https://catalogue.ceda.ac.uk/uuid/33592524dd9a4b2f897edbddb69b3381.

Dozat, T. (2016) Incorporating Nesterov Momentum into Adam. In *Proceedings of the 4th International Conference on Learning Representations*, 1–4.

Dubayah, R., Armston, J., Healey, S., Yang, Z., Patterson, P., Saarela, S., Stahl, G., Duncanson, L., Kellner, J., Bruening, J. and Pascual, A. (2023) Global Ecosystem Dynamics Investigation (GEDI) L4B Gridded Aboveground Biomass Density, Version 2.1. URL: https://daac.ornl.gov/cgi-bin/dsviewer.pl?ds_id=2299. Artwork Size: 0 MB Medium: COG Pages: 0 MB Version Number: 2.1.

Dubayah, R., Armston, J., Healey, S. P., Bruening, J. M., Patterson, P. L., Kellner, J. R., Duncanson, L., Saarela, S., Ståhl, G., Yang, Z., Tang, H., Blair, J. B., Fatoyinbo, L., Goetz, S., Hancock, S., Hansen, M., Hofton, M., Hurtt, G. and Luthcke, S. (2022a) GEDI launches a new era of biomass inference from space. *Environmental Research Letters*, **17**, 095001. URL: https://iopscience.iop.org/article/10.1088/1748-9326/ac8694.

Dubayah, R., Armston, J., Kellner, J., Duncanson, L., Healey, S., Patterson, P., Hancock, S., Tang, H., Bruening, J., Hofton, M., Blair, J. and Luthcke, S. (2022b) Global Ecosystem Dynamics Investigation (GEDI) L4A Footprint Level Aboveground Biomass Density, Version 2.1. URL: https://daac.ornl.gov/cgi-bin/dsviewer.pl?ds_id=2056. Artwork Size: 0 MB Medium: HDF5 Pages: 0 MB Version Number: 2.1.

Dubayah, R., Blair, J. B., Goetz, S., Fatoyinbo, L., Hansen, M., Healey, S., Hofton, M., Hurtt, G., Kellner, J., Luthcke, S., Armston, J., Tang, H., Duncanson, L., Hancock, S., Jantz, P., Marselis, S., Patterson, P. L., Qi, W. and Silva, C. (2020) The Global Ecosystem Dynamics Investigation: High-resolution laser ranging of the Earth's forests and topography. *Science of Remote Sensing*, **1**, 100002. URL: https://linkinghub.elsevier.com/retrieve/pii/S2666017220300018.

Duncanson, L., Kellner, J. R., Armston, J., Dubayah, R., Minor, D. M., Hancock, S., Healey, S. P., Patterson, P. L., Saarela, S., Marselis, S., Silva, C. E., Bruening, J., Goetz, S. J., Tang, H., Hofton, M., Blair, B., Luthcke, S., Fatoyinbo, L., Abernethy, K., Alonso, A., Andersen, H.-E., Aplin, P., Baker, T. R., Barbier, N., Bastin, J. F., Biber, P., Boeckx, P., Bogaert, J., Boschetti, L., Boucher, P. B., Boyd, D. S., Burslem, D. F., Calvo-Rodriguez, S., Chave, J., Chazdon, R. L., Clark, D. B., Clark, D. A., Cohen, W. B., Coomes, D. A., Corona, P., Cushman, K., Cutler, M. E., Dalling, J. W., Dalponte, M., Dash, J., de Miguel, S., Deng, S., Ellis, P. W., Erasmus, B., Fekety, P. A., Fernandez-Landa, A., Ferraz, A., Fischer, R., Fisher, A. G., García-Abril, A., Gobakken, T., Hacker, J. M., Heurich, M., Hill, R. A., Hopkinson, C., Huang, H., Hubbell, S. P., Hudak, A. T., Huth, A., Imbach, B., Jeffery, K. J., Katoh, M., Kearsley, E., Kenfack, D., Kljun, N., Knapp, N., Král, K., Krůček, M., Labrière, N., Lewis, S. L., Longo, M., Lucas, R. M., Main, R., Manzanera, J. A., Martínez, R. V., Mathieu, R., Memiaghe, H., Meyer, V., Mendoza, A. M., Monerris, A., Montesano, P., Morsdorf, F., Næsset, E., Naidoo, L., Nilus, R., O'Brien, M., Orwig, D. A., Papathanassiou, K., Parker, G., Philipson, C., Phillips, O. L., Pisek, J., Poulsen, J. R., Pretzsch, H., Rüdiger, C., Saatchi, S., Sanchez-Azofeifa, A., Sanchez-Lopez, N., Scholes, R., Silva, C. A., Simard, M., Skidmore, A., Stereńczak, K.,

Tanase, M., Torresan, C., Valbuena, R., Verbeeck, H., Vrska, T., Wessels, K., White, J. C., White, L. J., Zahabu, E. and Zgraggen, C. (2022) Aboveground biomass density models for NASA's Global Ecosystem Dynamics Investigation (GEDI) lidar mission. *Remote Sensing of Environment*, **270**, 112845. URL: https://linkinghub.elsevier.com/retrieve/pii/S0034425721005654.

Duncanson, L., Montesano, P., Neuenschwander, A., Thomas, N., Mandel, A., Minor, D., Guenther, E., Hancock, S., Feng, T., Barciauskas, A., Chang, G., Shah, S. and Satorius, B. (2023) Aboveground Biomass Density for High Latitude Forests from ICESat-2, 2020. URL: https://daac.ornl.gov/cgi-bin/dsviewer.pl?ds_id=2186. Artwork Size: 0 MB Medium: COG, CSV, GeoTIFF, ESRI Shapefile, GPKG Pages: 0 MB Version Number: 1.

Eggleston, H., Buendia, L., Miwa, K., Ngara, T. and Tanabe, K. (2006) 2006 IPCC Guidelines for National Greenhouse Gas Inventories.

ELVIS (2025) Elvis. URL: https://elevation.fsdf.org.au/.

European Space Agency and Airbus (2022) Copernicus DEM. URL: https://dataspace.copernicus.eu/explore-data/data-collections/copernicus-contributing-missions/collections-description/COP-DEM. Institution: European Space Agency.

FAO (2020) *Global Forest Resources Assessment 2020*. FAO. URL: http://www.fao.org/documents/card/en/c/ca9825en.

Fayad, I., Baghdadi, N. and Lahssini, K. (2022) An Assessment of the GEDI Lasers' Capabilities in Detecting Canopy Tops and Their Penetration in a Densely Vegetated, Tropical Area. *Remote Sensing*, **14**, 2969. URL: https://www.mdpi.com/2072-4292/14/13/2969.

Feldpausch, T. R., Lloyd, J., Lewis, S. L., Brienen, R. J. W., Gloor, M., Monteagudo Mendoza, A., Lopez-Gonzalez, G., Banin, L., Abu Salim, K., Affum-Baffoe, K., Alexiades, M., Almeida, S., Amaral, I., Andrade, A., Aragão, L. E. O. C., Araujo Murakami, A., Arets, E. J. M. M., Arroyo, L., Aymard C., G. A., Baker, T. R., Bánki, O. S., Berry, N. J., Cardozo, N., Chave, J., Comiskey, J. A., Alvarez, E., de Oliveira, A., Di Fiore, A., Djagbletey, G., Domingues, T. F., Erwin, T. L., Fearnside, P. M., França, M. B., Freitas, M. A., Higuchi, N., E. Honorio C., Iida, Y., Jiménez, E., Kassim, A. R., Killeen, T. J., Laurance, W. F., Lovett, J. C., Malhi, Y., Marimon, B. S., Marimon-Junior, B. H., Lenza, E., Marshall, A. R., Mendoza, C., Metcalfe, D. J., Mitchard, E. T. A., Neill, D. A., Nelson, B. W., Nilus, R., Nogueira, E. M., Parada, A., Peh, K. S.-H., Pena Cruz, A., Peñuela, M. C., Pitman, N. C. A., Prieto, A., Quesada, C. A., Ramírez, F., Ramírez-Angulo, H., Reitsma, J. M., Rudas, A., Saiz, G., Salomão, R. P., Schwarz, M., Silva, N., Silva-Espejo, J. E., Silveira, M., Sonké, B., Stropp, J., Taedoumg, H. E., Tan, S., ter Steege, H., Terborgh, J., Torello-Raventos, M., van der Heijden, G. M. F., Vásquez, R., Vilanova, E., Vos, V. A., White, L., Willcock, S., Woell, H. and Phillips, O. L. (2012) Tree height integrated into pantropical forest biomass estimates. *Biogeosciences*, **9**, 3381–3403. URL: https://bg.copernicus.org/articles/9/3381/2012/.

Fick, S. E. and Hijmans, R. J. (2017) WorldClim 2: new 1-km spatial resolution climate surfaces for global land areas. *International Journal of Climatology*, **37**, 4302–4315. URL: https://rmets.onlinelibrary.wiley.com/doi/10.1002/joc.5086.

Frantz, D. (2019) FORCE—Landsat + Sentinel-2 Analysis Ready Data and Beyond. *Remote Sensing*, **11**, 1124. URL: https://www.mdpi.com/2072-4292/11/9/1124.

Frantz, D., Haß, E., Uhl, A., Stoffels, J. and Hill, J. (2018) Improvement of the Fmask algorithm for Sentinel-2 images: Separating clouds from bright surfaces based on parallax effects. *Remote Sensing of Environment*, **215**, 471–481. URL: https://linkinghub.elsevier.com/retrieve/pii/S0034425718302037.

GeoHub (2025) Ontario Classified Point Cloud (Lidar-Derived). URL: https://geohub.lio.gov.on.ca/maps/mnrf::ontario-classified-point-cloud-lidar-derived/about.

GeoNB (2025) LiDAR Download. URL: https://geonb.snb.ca/li/.

Geoservices (2025) HD LiDAR | Geoservices. URL: https://geoservices.ign.fr/lidarhd.

GeoTiles (2025) GeoTiles: readymade geodata with a focus on the Netherlands. URL: https://geotiles.citg.tudelft.nl/.

Gibbs, D. A., Rose, M., Grassi, G., Melo, J., Rossi, S., Heinrich, V. and Harris, N. L. (2025) Revised and updated geospatial monitoring of 21st century forest carbon fluxes. *Earth System Science Data*, **17**, 1217–1243. URL: https://essd.copernicus.org/articles/17/1217/2025/.

Gonzalez-Akre, E., Piponiot, C., Lepore, M., Herrmann, V., Lutz, J. A., Baltzer, J. L., Dick, C. W., Gilbert, G. S., He, F., Heym, M., Huerta, A. I., Jansen, P. A., Johnson, D. J., Knapp, N., Král, K., Lin, D., Malhi, Y., McMahon, S. M., Myers, J. A., Orwig, D., Rodríguez-Hernández, D. I., Russo, S. E., Shue, J., Wang, X.,

Wolf, A., Yang, T., Davies, S. J. and Anderson-Teixeira, K. J. (2022) *allodb* : An R package for biomass estimation at globally distributed extratropical forest plots. *Methods in Ecology and Evolution*, **13**, 330–338. URL: https://besjournals.onlinelibrary.wiley.com/doi/10.1111/2041-210X.13756.

Gorelick, N., Hancher, M., Dixon, M., Ilyushchenko, S., Thau, D. and Moore, R. (2017) Google Earth Engine: Planetary-scale geospatial analysis for everyone. *Remote Sensing of Environment*, **202**, 18–27. URL: https://linkinghub.elsevier.com/retrieve/pii/S0034425717302900.

Griscom, B. W., Adams, J., Ellis, P. W., Houghton, R. A., Lomax, G., Miteva, D. A., Schlesinger, W. H., Shoch, D., Siikamäki, J. V., Smith, P., Woodbury, P., Zganjar, C., Blackman, A., Campari, J., Conant, R. T., Delgado, C., Elias, P., Gopalakrishna, T., Hamsik, M. R., Herrero, M., Kiesecker, J., Landis, E., Laestadius, L., Leavitt, S. M., Minnemeyer, S., Polasky, S., Potapov, P., Putz, F. E., Sanderman, J., Silvius, M., Wollenberg, E. and Fargione, J. (2017) Natural climate solutions. *Proceedings of the National Academy of Sciences of the United States of America*, **114**, 11645–11650. URL: http://dx.doi.org/10.1073/pnas.1710465114.

GSFC (2025) G-LiHT. URL: https://gliht.gsfc.nasa.gov/. Publisher: 610 WebDev.

Hansen, M. C., Potapov, P. V., Moore, R., Hancher, M., Turubanova, S. A., Tyukavina, A., Thau, D., Stehman, S. V., Goetz, S. J., Loveland, T. R., Kommareddy, A., Egorov, A., Chini, L., Justice, C. O. and Townshend, J. R. G. (2013) High-resolution global maps of 21st-century forest cover change. *Science*, **342**, 850–853. URL: http://dx.doi.org/10.1126/science.1244693.

Harris, N. L., Gibbs, D. A., Baccini, A., Birdsey, R. A., De Bruin, S., Farina, M., Fatoyinbo, L., Hansen, M. C., Herold, M., Houghton, R. A., Potapov, P. V., Suarez, D. R., Roman-Cuesta, R. M., Saatchi, S. S., Slay, C. M., Turubanova, S. A. and Tyukavina, A. (2021) Global maps of twenty-first century forest carbon fluxes. *Nature Climate Change*, **11**, 234–240. URL: https://www.nature.com/articles/s41558-020-00976-6. Publisher: Springer Science and Business Media LLC.

Hawkins, B. A. (2012) Eight (and a half) deadly sins of spatial analysis. *Journal of Biogeography*, **39**, 1–9. URL: https://onlinelibrary.wiley.com/doi/10.1111/j.1365-2699.2011.02637.x.

Holben, B. and Fraser, R. S. (1984) Red and near-infrared sensor response to off-nadiir viewing. *International Journal of Remote Sensing*, **5**, 145–160. URL: https://www.tandfonline.com/doi/full/10.1080/01431168408948795.

Hunka, N., Duncanson, L., Armston, J., Dubayah, R., Healey, S. P., Santoro, M., May, P., Araza, A., Bourgoin, C., Montesano, P. M., Neigh, C. S. R., Grantham, H., Potapov, P., Turubanova, S., Tyukavina, A., Richter, J., Harris, N., Urbazaev, M., Pascual, A., Suarez, D. R., Herold, M., Poulter, B., Wilson, S. N., Grassi, G., Federici, S., Sanz, M. J. and Melo, J. (2024) Intergovernmental Panel on Climate Change (IPCC) Tier 1 forest biomass estimates from Earth Observation. *Scientific Data*, **11**, 1127. URL: https://www.nature.com/articles/s41597-024-03930-9.

Hunka, N., Santoro, M., Armston, J., Dubayah, R., McRoberts, R., Næsset, E., Quegan, S., Urbazaev, M., Pascual, A., May, P. B., Minor, D., Leitold, V., Basak, P., Liang, M., Melo, J., Herold, M., Malága, N., Wilson, S., Montesinos, P. D., Arana, A., De La Cruz Paiva, R. E., Ferrand, J., Keoka, S., Guerra-Hernandez, J. and Duncanson, L. (2023) On the NASA GEDI and ESA CCI biomass maps: Aligning for uptake in the UNFCCC global stocktake. *Environmental Research Letters*. URL: https://iopscience.iop.org/article/10.1088/1748-9326/ad0b60.

IPCC (2023) *Climate Change 2021 – The Physical Science Basis: Working Group I Contribution to the Sixth Assessment Report of the Intergovernmental Panel on Climate Change*. Cambridge University Press, 1 edn. URL: https://www.cambridge.org/core/product/identifier/9781009157896/type/book.

Jia, D., Wang, C., Hakkenberg, C. R., Numata, I., Elmore, A. J. and Cochrane, M. A. (2024) Accuracy evaluation and effect factor analysis of GEDI aboveground biomass product for temperate forests in the conterminous United States. *GIScience & Remote Sensing*, **61**. URL: https://www.tandfonline.com/doi/full/10.1080/15481603.2023.2292374. Publisher: Informa UK Limited.

Johnson, J. M., Munasinghe, D., Eyelade, D. and Cohen, S. (2019) An integrated evaluation of the National Water Model (NWM)–Height Above Nearest Drainage (HAND) flood mapping methodology. *Natural Hazards and Earth System Sciences*, **19**, 2405–2420. URL: https://nhess.copernicus.org/articles/19/2405/2019/.

Jordan, C. F. (1969) Derivation of leaf-area index from quality of light on the Forest floor. *Ecology*, **50**, 663–666. URL: http://doi.wiley.com/10.2307/1936256. Publisher: Wiley.

Jucker, T., Bongalov, B., Burslem, D. F. R. P., Nilus, R., Dalponte, M., Lewis, S. L., Phillips, O. L., Qie, L. and Coomes, D. A. (2018) Topography shapes the structure, composition and function of tropical forest landscapes. *Ecology Letters*, **21**, 989–1000. URL: https://onlinelibrary.wiley.com/doi/10.1111/ele.12964.

Jucker, T., Caspersen, J., Chave, J., Antin, C., Barbier, N., Bongers, F., Dalponte, M., Van Ewijk, K. Y., Forrester, D. I., Haeni, M., Higgins, S. I., Holdaway, R. J., Iida, Y., Lorimer, C., Marshall, P. L., Momo, S., Moncrieff, G. R., Ploton, P., Poorter, L., Rahman, K. A., Schlund, M., Sonké, B., Sterck, F. J., Trugman, A. T., Usoltsev, V. A., Vanderwel, M. C., Waldner, P., Wedeux, B. M. M., Wirth, C., Wöll, H., Woods, M., Xiang, W., Zimmermann, N. E. and Coomes, D. A. (2017) Allometric equations for integrating remote sensing imagery into forest monitoring programmes. *Global Change Biology*, **23**, 177–190. URL: https://onlinelibrary.wiley.com/doi/10.1111/gcb.13388.

Kattenborn, T., Leitloff, J., Schiefer, F. and Hinz, S. (2021) Review on Convolutional Neural Networks (CNN) in vegetation remote sensing. *ISPRS journal of photogrammetry and remote sensing: official publication of the International Society for Photogrammetry and Remote Sensing*, **173**, 24–49. URL: https://www.sciencedirect.com/science/article/pii/S0924271620303488.

Kellndorfer, J. M., Walker, W. S., LaPoint, E., Kirsch, K., Bishop, J. and Fiske, G. (2010) Statistical fusion of lidar, InSAR, and optical remote sensing data for forest stand height characterization: A regional-scale method based on LVIS, SRTM, Landsat ETM+, and ancillary data sets. *Journal of Geophysical Research: Biogeosciences*, **115**, 2009JG000997. URL: https://agupubs.onlinelibrary.wiley.com/doi/10.1029/2009JG000997.

Kellner, J. R., Armston, J. and Duncanson, L. (2023) Algorithm Theoretical Basis Document for GEDI Footprint Aboveground Biomass Density. *Earth and Space Science*, **10**, e2022EA002516. URL: https://agupubs.onlinelibrary.wiley.com/doi/10.1029/2022EA002516.

Kennedy, R. E., Yang, Z. and Cohen, W. B. (2010) Detecting trends in forest disturbance and recovery using yearly Landsat time series: 1. LandTrendr — Temporal segmentation algorithms. *Remote Sensing of Environment*, **114**, 2897–2910. URL: https://linkinghub.elsevier.com/retrieve/pii/S0034425710002245.

Khosravipour, A., Skidmore, A. K., Isenburg, M., Wang, T. and Hussin, Y. A. (2014) Generating Pit-free Canopy Height Models from Airborne Lidar. *Photogrammetric Engineering & Remote Sensing*, **80**, 863–872.

Klemmer, K., Rolf, E., Robinson, C., Mackey, L. and Rußwurm, M. (2025) Satclip: Global, general-purpose location embeddings with satellite imagery. In *Proceedings of the AAAI Conference on Artificial Intelligence*, vol. 39, 4347–4355. Issue: 4.

Knipling, E. B. (1970) Physical and physiological basis for the reflectance of visible and near-infrared radiation from vegetation. *Remote Sensing of Environment*, **1**, 155–159. URL: https://linkinghub.elsevier.com/retrieve/pii/S0034425770800219.

Konings, A. G., Rao, K. and Steele-Dunne, S. C. (2019) Macro to micro: microwave remote sensing of plant water content for physiology and ecology. *The New phytologist*, **223**, 1166–1172. URL: http://dx.doi.org/10.1111/nph.15808.

Kump, L. R., Kasting, J. F. and Crane, R. G. (2010) *The earth system*. San Francisco, München: Prentice Hall, 3. ed edn.

Kutchartt, E., Pedron, M. and Pirotti, F. (2022) ASSESSMENT OF CANOPY AND GROUND HEIGHT ACCURACY FROM GEDI LIDAR OVER STEEP MOUNTAIN AREAS. *ISPRS Annals of the Photogrammetry, Remote Sensing and Spatial Information Sciences*, **V-3-2022**, 431–438. URL: https://isprs-annals.copernicus.org/articles/V-3-2022/431/2022/.

Lang, N., Jetz, W., Schindler, K. and Wegner, J. D. (2023) A high-resolution canopy height model of the Earth. *Nature Ecology & Evolution*, **7**, 1778–1789. URL: https://www.nature.com/articles/s41559-023-02206-6.

Lang, N., Kalischek, N., Armston, J., Schindler, K., Dubayah, R. and Wegner, J. D. (2022) Global canopy height regression and uncertainty estimation from GEDI LIDAR waveforms with deep ensembles. *Remote Sensing of Environment*, **268**, 112760. URL: https://linkinghub.elsevier.com/retrieve/pii/S0034425721004806.

Lefsky, M. A. (2010) A global forest canopy height map from the Moderate Resolution Imaging Spectroradiometer and the Geoscience Laser Altimeter System. *Geophysical Research Letters*, **37**, 2010GL043622. URL: https://agupubs.onlinelibrary.wiley.com/doi/10.1029/2010GL043622.

Lefsky, M. A., Cohen, W. B., Parker, G. G. and Harding, D. J. (2002) Lidar Remote Sensing for Ecosystem Studies. *BioScience*, **52**, 19. URL: https://academic.oup.com/bioscience/article/52/1/19-30/291259.

LGIA (2025) Basic data of the Digital Surface Model | Latvijas Ģeotelpiskās informācijas aģentūra. URL: https://www.lgia.gov.lv/en/Digit%C4%81lais%20virsmas%20modelis.

Li, S., Brandt, M., Fensholt, R., Kariryaa, A., Igel, C., Gieseke, F., Nord-Larsen, T., Oehmcke, S., Carlsen, A. H., Junttila, S., Tong, X., d'Aspremont, A. and Ciais, P. (2023) Deep learning enables image-based tree counting, crown segmentation, and height prediction at national scale. *PNAS Nexus*, **2**, pgad076. URL: https://academic.oup.com/pnasnexus/article/doi/10.1093/pnasnexus/pgad076/7073732.

Li, W., Niu, Z., Gao, S., Huang, N. and Chen, H. (2014) Correlating the Horizontal and Vertical Distribution of LiDAR Point Clouds with Components of Biomass in a Picea crassifolia Forest. *Forests*, **5**, 1910–1930. URL: https://www.mdpi.com/1999-4907/5/8/1910.

LidarBC (2025) LidarBC. URL: https://lidar.gov.bc.ca/.

Liu, A., Cheng, X. and Chen, Z. (2021) Performance evaluation of GEDI and ICESat-2 laser altimeter data for terrain and canopy height retrievals. *Remote Sensing of Environment*, **264**, 112571. URL: https://linkinghub.elsevier.com/retrieve/pii/S0034425721002911.

Liu, S., Csillik, O., Ordway, E. M., Chang, L.-L., Longo, M., Keller, M. and Moorcroft, P. R. (2025) Environmental drivers of spatial variation in tropical forest canopy height: Insights from NASA's GEDI spaceborne LiDAR. *Proceedings of the National Academy of Sciences*, **122**, e2401755122. URL: https://pnas.org/doi/10.1073/pnas.2401755122.

LSDB (2025) Elevation Data. URL: https://geoportaal.maaamet.ee/eng/spatial-data/elevation-data-p308.html.

Lu, K., Kluger, D. M., Bates, S. and Wang, S. (2024) Regression coefficient estimation from remote sensing maps. URL: https://arxiv.org/abs/2407.13659. Version Number: 7.

Lunch, C., Laney, C., Mietkiewicz, N., Sokol, E., Cawley, K. and NEON (National Ecological Observatory Network) (2024) neonUtilities: Utilities for Working with NEON Data. URL: https://CRAN.R-project.org/package=neonUtilities.

LVIS (2025) Land, Vegetation, and Ice Sensor (LVIS). URL: https://lvis.gsfc.nasa.gov/Data/GE.html.

Ma, L., Hurtt, G., Tang, H., Lamb, R., Lister, A., Chini, L., Dubayah, R., Armston, J., Campbell, E., Duncanson, L., Healey, S., O'Neil-Dunne, J., Ott, L., Poulter, B. and Shen, Q. (2023) Spatial heterogeneity of global forest aboveground carbon stocks and fluxes constrained by spaceborne lidar data and mechanistic modeling. *Global Change Biology*, gcb.16682. URL: https://onlinelibrary.wiley.com/doi/10.1111/gcb.16682.

Malhi, Y., Girardin, C. A. J., Goldsmith, G. R., Doughty, C. E., Salinas, N., Metcalfe, D. B., Huaraca Huasco, W., Silva-Espejo, J. E., Del Aguilla-Pasquell, J., Farfán Amézquita, F., Aragão, L. E. O. C., Guerrieri, R., Ishida, F. Y., Bahar, N. H. A., Farfan-Rios, W., Phillips, O. L., Meir, P. and Silman, M. (2017) The variation of productivity and its allocation along a tropical elevation gradient: a whole carbon budget perspective. *New Phytologist*, **214**, 1019–1032. URL: https://nph.onlinelibrary.wiley.com/doi/10.1111/nph.14189. Publisher: Wiley.

Marifatul Haq, S., Rashid, I., Soares Calixto, E., Ali, A., Kumar, M., Srivastava, G., Bussmann, R. W. and Ahmad Khuroo, A. (2022) Unravelling patterns of forest carbon stock along a wide elevational gradient in the Himalaya: Implications for climate change mitigation. *Forest Ecology and Management*, **521**, 120442. URL: https://linkinghub.elsevier.com/retrieve/pii/S0378112722004364. Publisher: Elsevier BV.

Martin, A. R., Doraisami, M. and Thomas, S. C. (2018) Global patterns in wood carbon concentration across the world's trees and forests. *Nature Geoscience*, **11**, 915–920. URL: https://www.nature.com/articles/s41561-018-0246-x.

Marvin, D. C., Asner, G. P., Knapp, D. E., Anderson, C. B., Martin, R. E., Sinca, F. and Tupayachi, R. (2014) Amazonian landscapes and the bias in field studies of forest structure and biomass. *Proceedings of the National Academy of Sciences*, **111**. URL: https://pnas.org/doi/full/10.1073/pnas.1412999111.

Marvin, D. C., Sleeter, B. M., Cameron, D. R., Nelson, E. and Plantinga, A. J. (2023) Natural climate solutions provide robust carbon mitigation capacity under future climate change scenarios. *Scientific Reports*, **13**, 19008. URL: https://www.nature.com/articles/s41598-023-43118-6.

Mascaro, J., Detto, M., Asner, G. P. and Muller-Landau, H. C. (2011) Evaluating uncertainty in mapping forest carbon with airborne LiDAR. *Remote Sensing of Environment*, **115**, 3770–3774. URL: https://linkinghub.elsevier.com/retrieve/pii/S0034425711002720.

Matasci, G., Hermosilla, T., Wulder, M. A., White, J. C., Coops, N. C., Hobart, G. W., Bolton, D. K., Tompalski, P. and Bater, C. W. (2018) Three decades of forest structural dynamics over Canada's forested ecosystems using Landsat time-series and lidar plots. *Remote Sensing of Environment*, **216**, 697–714. URL: https://linkinghub.elsevier.com/retrieve/pii/S0034425718303572.

Mayr, E. (2004) Another look at the species problem. In *What Makes Biology Unique?*, 171–194. Cambridge University Press, 1 edn. URL: https://www.cambridge.org/core/product/identifier/CBO9780511617188A017/type/book_part.

Menlove, J. and Healey, S. (2021) Forest Aboveground Biomass from FIA Plots across the Conterminous USA, 2009-2019. URL: https://daac.ornl.gov/cgi-bin/dsviewer.pl?ds_id=1873. Artwork Size: 0 MB Medium: KMZ Shapefile, ESRI Shapefile Pages: 0 MB Version Number: 1.

Menlove, J. and Healey, S. P. (2020) A Comprehensive Forest Biomass Dataset for the USA Allows Customized Validation of Remotely Sensed Biomass Estimates. *Remote Sensing*, **12**, 4141. URL: https://www.mdpi.com/2072-4292/12/24/4141.

Meyer, H. and Pebesma, E. (2022) Machine learning-based global maps of ecological variables and the challenge of assessing them. *Nature Communications*, **13**, 2208. URL: https://www.nature.com/articles/s41467-022-29838-9.

Mitchard, E. T. A., Feldpausch, T. R., Brienen, R. J. W., Lopez-Gonzalez, G., Monteagudo, A., Baker, T. R., Lewis, S. L., Lloyd, J., Quesada, C. A., Gloor, M., Ter Steege, H., Meir, P., Alvarez, E., Araujo-Murakami, A., Aragão, L. E. O. C., Arroyo, L., Aymard, G., Banki, O., Bonal, D., Brown, S., Brown, F. I., Cerón, C. E., Chama Moscoso, V., Chave, J., Comiskey, J. A., Cornejo, F., Corrales Medina, M., Da Costa, L., Costa, F. R. C., Di Fiore, A., Domingues, T. F., Erwin, T. L., Frederickson, T., Higuchi, N., Honorio Coronado, E. N., Killeen, T. J., Laurance, W. F., Levis, C., Magnusson, W. E., Marimon, B. S., Marimon Junior, B. H., Mendoza Polo, I., Mishra, P., Nascimento, M. T., Neill, D., Núñez Vargas, M. P., Palacios, W. A., Parada, A., Pardo Molina, G., Peña-Claros, M., Pitman, N., Peres, C. A., Poorter, L., Prieto, A., Ramirez-Angulo, H., Restrepo Correa, Z., Roopsind, A., Roucoux, K. H., Rudas, A., Salomão, R. P., Schietti, J., Silveira, M., De Souza, P. F., Steininger, M. K., Stropp, J., Terborgh, J., Thomas, R., Toledo, M., Torres-Lezama, A., Van Andel, T. R., Van Der Heijden, G. M. F., Vieira, I. C. G., Vieira, S., Vilanova-Torre, E., Vos, V. A., Wang, O., Zartman, C. E., Malhi, Y. and Phillips, O. L. (2014) Markedly divergent estimates of Amazon forest carbon density from ground plots and satellites. *Global Ecology and Biogeography*, **23**, 935–946. URL: https://onlinelibrary.wiley.com/doi/10.1111/geb.12168. Publisher: Wiley.

Mitchard, E. T. A., Saatchi, S. S., Woodhouse, I. H., Nangendo, G., Ribeiro, N. S., Williams, M., Ryan, C. M., Lewis, S. L., Feldpausch, T. R. and Meir, P. (2009) Using satellite radar backscatter to predict above-ground woody biomass: A consistent relationship across four different African landscapes. *Geophysical Research Letters*, **36**, 2009GL040692. URL: https://agupubs.onlinelibrary.wiley.com/doi/10.1029/2009GL040692.

Mitchell, A. L., Rosenqvist, A. and Mora, B. (2017) Current remote sensing approaches to monitoring forest degradation in support of countries measurement, reporting and verification (MRV) systems for REDD+. *Carbon Balance and Management*, **12**, 9. URL: https://cbmjournal.biomedcentral.com/articles/10.1186/s13021-017-0078-9.

Montesano, P., Neuenschwander, A., Guenther, E. and Duncanson, L. (2024) ICESat-2 Derived 30 m Along-Track Boreal Aboveground Biomass Density, Version 1. URL: http://nsidc.org/data/IS2ATBABD/versions/1.

Moreno-Martinez, A., Camps-Valls, G., Kattge, J., Robinson, N., Reichstein, M., van Bodegom, P., Kramer, K., Cornelissen, J. H. C., Reich, P., Bahn, M., Niinemets, U., Peñuelas, J., Craine, J. M., Cerabolini, B. E. L., Minden, V., Laughlin, D. C., Sack, L., Allred, B., Baraloto, C., Byun, C., Soudzilovskaia, N. A. and Running, S. W. (2018) A methodology to derive global maps of leaf traits using remote sensing and climate data. *Remote sensing of environment*, **218**, 69–88. URL: https://www.sciencedirect.com/science/article/pii/S0034425718304176.

Musinsky, J., Goulden, T., Wirth, G., Leisso, N., Krause, K., Haynes, M. and Chapman, C. (2022) Spanning scales: The airborne spatial and temporal sampling design of the National Ecological Observatory Network. *Methods in Ecology and Evolution*, **13**, 1866–1884. URL: https://besjournals.onlinelibrary.wiley.com/doi/10.1111/2041-210X.13942.

Mutanga, O., Masenyama, A. and Sibanda, M. (2023) Spectral saturation in the remote sensing of high-density vegetation traits: A systematic review of progress, challenges, and prospects. *ISPRS Journal of Photogrammetry and Remote Sensing*, **198**, 297–309.

URL: https://linkinghub.elsevier.com/retrieve/pii/S0924271623000709.

National Ecological Observatory Network (2025) *geoNEON: Geolocation Data Access for NEON Data*. URL: https://github.com/NEONScience/NEON-geolocation.

NEON (2024) Vegetation structure (DP1.10098.001): RELEASE-2024. URL: https://data.neonscience.org/data-products/DP1.10098.001/RELEASE-2024. Artwork Size: 2.2 GB Pages: 2.2 GB.

— (2025) Discrete return LiDAR point cloud (DP1.30003.001): RELEASE-2025. URL: https://data.neonscience.org/data-products/DP1.30003.001/RELEASE-2025. Artwork Size: 12.1 TB Pages: 12.1 TB.

Ni-Meister, W., Lee, S., Strahler, A. H., Woodcock, C. E., Schaaf, C., Yao, T., Ranson, K. J., Sun, G. and Blair, J. B. (2010) Assessing general relationships between aboveground biomass and vegetation structure parameters for improved carbon estimate from lidar remote sensing. *Journal of Geophysical Research: Biogeosciences*, **115**, 2009JG000936. URL: https://agupubs.onlinelibrary.wiley.com/doi/10.1029/2009JG000936.

NLS (2025) Laser scanning data - National Land Survey of Finland. URL: https://asiointi.maanmittauslaitos.fi/karttapaikka/tiedostopalvelu/laserkeilausaineisto_05?lang=en.

Olson, D. M., Dinerstein, E., Wikramanayake, E. D., Burgess, N. D., Powell, G. V. N., Underwood, E. C., D'amico, J. A., Itoua, I., Strand, H. E., Morrison, J. C., Loucks, C. J., Allnutt, T. F., Ricketts, T. H., Kura, Y., Lamoreux, J. F., Wettengel, W. W., Hedao, P. and Kassem, K. R. (2001) Terrestrial Ecoregions of the World: A New Map of Life on Earth. *BioScience*, **51**, 933. URL: https://academic.oup.com/bioscience/article/51/11/933-938/227116.

Ometto, J., Gorgens, E. B., Pereira, F. R. d. S., Sato, L., Assis, M. L. R., Cantinho, R., Longo, M., Jacon, A. D. and Keller, M. (2023) L1A - Discrete airborne LiDAR transects collected by EBA in the Brazilian Amazon (Mato Grosso, Amazonas e Pará). URL: https://zenodo.org/record/7636454.

OpenTopography (2025) OpenTopography - Data Catalog. URL: https://portal.opentopography.org/dataCatalog.

Ottinger, M. and Kuenzer, C. (2020) Spaceborne L-Band Synthetic Aperture Radar Data for Geoscientific Analyses in Coastal Land Applications: A Review. *Remote Sensing*, **12**, 2228. URL: https://www.mdpi.com/2072-4292/12/14/2228.

Pascual, A., May, P. B., Cárdenas-Martínez, A., Guerra-Hernández, J., Hunka, N., Bruening, J. M., Healey, S. P., Armston, J. D. and Dubayah, R. O. (2025) Calibration of GEDI footprint aboveground biomass models in Mediterranean forests with NFI plots: A comparison of approaches. *Journal of Environmental Management*, **375**, 124313. URL: https://linkinghub.elsevier.com/retrieve/pii/S0301479725002890.

Pasquarella, V. J., Arévalo, P., Bratley, K. H., Bullock, E. L., Gorelick, N., Yang, Z. and Kennedy, R. E. (2022) Demystifying LandTrendr and CCDC temporal segmentation. *International Journal of Applied Earth Observation and Geoinformation*, **110**, 102806. URL: https://linkinghub.elsevier.com/retrieve/pii/S1569843222000085.

Patterson, P. L., Healey, S. P., Ståhl, G., Saarela, S., Holm, S., Andersen, H.-E., Dubayah, R. O., Duncanson, L., Hancock, S., Armston, J., Kellner, J. R., Cohen, W. B. and Yang, Z. (2019) Statistical properties of hybrid estimators proposed for GEDI—NASA's global ecosystem dynamics investigation. *Environmental Research Letters*, **14**, 065007. URL: https://iopscience.iop.org/article/10.1088/1748-9326/ab18df.

Pauls, J., Zimmer, M., Kelly, U. M., Schwartz, M., Saatchi, S., Ciais, P., Pokutta, S., Brandt, M. and Gieseke, F. (2024) Estimating Canopy Height at Scale. URL: http://arxiv.org/abs/2406.01076. ArXiv:2406.01076 [cs].

Pearl, J. (2022) Comment: Understanding Simpson's Paradox. In *Probabilistic and Causal Inference* (eds. H. Geffner, R. Dechter and J. Y. Halpern), 399–412. New York, NY, USA: ACM, 1 edn. URL: https://dl.acm.org/doi/10.1145/3501714.3501738.

Phaisangittisagul, E. (2016) An Analysis of the Regularization Between L2 and Dropout in Single Hidden Layer Neural Network. In *2016 7th International Conference on Intelligent Systems, Modelling and Simulation (ISMS)*, 174–179. Bangkok, Thailand: IEEE. URL: http://ieeexplore.ieee.org/document/7877209/.

Ploton, P., Mortier, F., Réjou-Méchain, M., Barbier, N., Picard, N., Rossi, V., Dormann, C., Cornu, G., Viennois, G., Bayol, N., Lyapustin, A., Gourlet-Fleury, S. and Pélissier, R. (2020) Spatial validation reveals poor predictive performance of large-scale ecological mapping models. *Nature communications*, **11**, 4540. URL: http://dx.doi.org/10.1038/s41467-020-18321-y.

Poggio, L., De Sousa, L. M., Batjes, N. H., Heuvelink, G. B. M., Kempen, B., Ribeiro, E. and Rossiter, D. (2021) SoilGrids 2.0: producing soil information for the globe with quantified spatial uncertainty. *SOIL*, **7**, 217–240. URL: https://soil.copernicus.org/articles/7/217/2021/.

Potapov, P., Li, X., Hernandez-Serna, A., Tyukavina, A., Hansen, M. C., Kommareddy, A., Pickens, A., Turubanova, S., Tang, H., Silva, C. E., Armston, J., Dubayah, R., Blair, J. B. and Hofton, M. (2021) Mapping global forest canopy height through integration of GEDI and Landsat data. *Remote Sensing of Environment*, **253**, 112165. URL: https://linkinghub.elsevier.com/retrieve/pii/S0034425720305381.

Qiu, S., Zhu, Z., Olofsson, P., Woodcock, C. E. and Jin, S. (2023) Evaluation of Landsat image compositing algorithms. *Remote Sensing of Environment*, **285**, 113375. URL: https://www.sciencedirect.com/science/article/pii/S0034425722004813.

Radeloff, V. C., Roy, D. P., Wulder, M. A., Anderson, M., Cook, B., Crawford, C. J., Friedl, M., Gao, F., Gorelick, N., Hansen, M., Healey, S., Hostert, P., Hulley, G., Huntington, J. L., Johnson, D. M., Neigh, C., Lyapustin, A., Lymburner, L., Pahlevan, N., Pekel, J.-F., Scambos, T. A., Schaaf, C., Strobl, P., Woodcock, C. E., Zhang, H. K. and Zhu, Z. (2024) Need and vision for global medium-resolution Landsat and Sentinel-2 data products. *Remote Sensing of Environment*, **300**, 113918. URL: https://linkinghub.elsevier.com/retrieve/pii/S0034425723004704.

Rodda, S. R., Fararoda, R., Gopalakrishnan, R., Jha, N., Réjou-Méchain, M., Couteron, P., Barbier, N., Alfonso, A., Bako, O., Bassama, P., Behera, D., Bissiengou, P., Biyiha, H., Brockelman, W. Y., Chanthorn, W., Chauhan, P., Dadhwal, V. K., Dauby, G., Deblauwe, V., Dongmo, N., Droissart, V., Jeyakumar, S., Jha, C. S., Kandem, N. G., Katembo, J., Kougue, R., Leblanc, H., Lewis, S., Libalah, M., Manikandan, M., Martin-Ducup, O., Mbock, G., Memiaghe, H., Mofack, G., Mutyala, P., Narayanan, A., Nathalang, A., Ndjock, G. O., Ngoula, F., Nidamanuri, R. R., Pélissier, R., Saatchi, S., Sagang, L. B., Salla, P., Simo-Droissart, M., Smith, T. B., Sonké, B., Stevart, T., Tjomb, D., Zebaze, D., Zemagho, L. and Ploton, P. (2024) LiDAR-based reference aboveground biomass maps for tropical forests of South Asia and Central Africa. *Scientific Data*, **11**, 334. URL: https://www.nature.com/articles/s41597-024-03162-x.

Romano, Y., Patterson, E. and Candes, E. (2019) Conformalized quantile regression. *Advances in neural information processing systems*, **32**.

Ronneberger, O., Fischer, P. and Brox, T. (2015) U-Net: Convolutional Networks for Biomedical Image Segmentation. In *Medical Image Computing and Computer-Assisted Intervention – MICCAI 2015* (eds. N. Navab, J. Hornegger, W. M. Wells and A. F. Frangi), vol. 9351, 234–241. Cham: Springer International Publishing. URL: http://link.springer.com/10.1007/978-3-319-24574-4_28. Series Title: Lecture Notes in Computer Science.

Roy, D., Wulder, M., Loveland, T., C.E., W., Allen, R., Anderson, M., Helder, D., Irons, J., Johnson, D., Kennedy, R., Scambos, T., Schaaf, C., Schott, J., Sheng, Y., Vermote, E., Belward, A., Bindschadler, R., Cohen, W., Gao, F., Hipple, J., Hostert, P., Huntington, J., Justice, C., Kilic, A., Kovalskyy, V., Lee, Z., Lymburner, L., Masek, J., McCorkel, J., Shuai, Y., Trezza, R., Vogelmann, J., Wynne, R. and Zhu, Z. (2014) Landsat-8: Science and product vision for terrestrial global change research. *Remote Sensing of Environment*, **145**, 154–172. URL: https://linkinghub.elsevier.com/retrieve/pii/S003442571400042X. Publisher: Elsevier BV.

Réjou-Méchain, M., Barbier, N., Couteron, P., Ploton, P., Vincent, G., Herold, M., Mermoz, S., Saatchi, S., Chave, J., de Boissieu, F., Féret, J.-B., Takoudjou, S. M. and Pélissier, R. (2019) Upscaling Forest Biomass from Field to Satellite Measurements: Sources of Errors and Ways to Reduce Them. *Surveys in Geophysics*, **40**, 881–911. URL: http://link.springer.com/10.1007/s10712-019-09532-0.

Réjou-Méchain, M., Tanguy, A., Piponiot, C., Chave, J. and Hérault, B. (2017) biomass : an r package for estimating above-ground biomass and its uncertainty in tropical forests. *Methods in Ecology and Evolution*, **8**, 1163–1167. URL: https://besjournals.onlinelibrary.wiley.com/doi/10.1111/2041-210X.12753.

Saatchi, S. S., Harris, N. L., Brown, S., Lefsky, M., Mitchard, E. T. A., Salas, W., Zutta, B. R., Buermann, W., Lewis, S. L., Hagen, S., Petrova, S., White, L., Silman, M. and Morel, A. (2011) Benchmark map of forest carbon stocks in tropical regions across three continents. *Proceedings of the National Academy of Sciences*, **108**, 9899–9904. URL: https://pnas.org/doi/full/10.1073/pnas.1019576108.

Santoro, M. (2018) GlobBiomass - global datasets of forest biomass. URL: https://doi.pangaea.de/10.1594/PANGAEA.894711. Artwork Size: 174 data points Pages: 174 data points.

Santoro, M., Cartus, O., Lucas, R. and Kay, H. (2023) CCI Biomass Algorithm Theoretical Basis Document Version 4.0. URL: https://climate.esa.int/media/documents/D2_2_Algorithm_Theoretical_Basis_Document_ATBD_V4.0_20230317.pdf.

Shimada, M., Isoguchi, O., Tadono, T. and Isono, K. (2009) PALSAR Radiometric and Geometric Calibration. *IEEE transactions on geoscience and remote sensing: a publication of the IEEE Geoscience and Remote Sensing Society*, **47**, 3915–3932. URL: http://dx.doi.org/10.1109/TGRS.2009.2023909. Publisher: ieeexplore.ieee.org.

Simard, M., Pinto, N., Fisher, J. B. and Baccini, A. (2011) Mapping forest canopy height globally with spaceborne lidar. *Journal of Geophysical Research*, **116**, G04021. URL: http://doi.wiley.com/10.1029/2011JG001708.

Singh, M., Evans, D., Coomes, D. A., Friess, D. A., Suy Tan, B. and Samean Nin, C. (2016) Incorporating Canopy Cover for Airborne-Derived Assessments of Forest Biomass in the Tropical Forests of Cambodia. *PLOS ONE*, **11**, e0154307. URL: https://dx.plos.org/10.1371/journal.pone.0154307.

Skakun, S., Wevers, J., Brockmann, C., Doxani, G., Aleksandrov, M., Batič, M., Frantz, D., Gascon, F., Gómez-Chova, L., Hagolle, O., López-Puigdollers, D., Louis, J., Lubej, M., Mateo-García, G., Osman, J., Peressutti, D., Pflug, B., Puc, J., Richter, R., Roger, J.-C., Scaramuzza, P., Vermote, E., Vesel, N., Zupanc, A. and Žust, L. (2022) Cloud Mask Intercomparison eXercise (CMIX): An evaluation of cloud masking algorithms for Landsat 8 and Sentinel-2. *Remote Sensing of Environment*, **274**, 112990. URL: https://linkinghub.elsevier.com/retrieve/pii/S0034425722001043.

Stanke, H., Finley, A. O., Weed, A. S., Walters, B. F. and Domke, G. M. (2020) rFIA: An R package for estimation of forest attributes with the US Forest Inventory and Analysis database. *Environmental Modelling & Software*, **127**, 104664. URL: https://linkinghub.elsevier.com/retrieve/pii/S1364815219311089.

Steckel, J. C., Jakob, M., Flachsland, C., Kornek, U., Lessmann, K. and Edenhofer, O. (2017) From climate finance toward sustainable development finance. *WIREs Climate Change*, **8**, e437. URL: https://wires.onlinelibrary.wiley.com/doi/10.1002/wcc.437.

Sun, L., Wei, J., Wang, J., Mi, X., Guo, Y., Lv, Y., Yang, Y., Gan, P., Zhou, X., Jia, C. and Tian, X. (2016) A Universal Dynamic Threshold Cloud Detection Algorithm (UDTCDA) supported by a prior surface reflectance database: UDTCDA, Surface Reflectance Database. *Journal of Geophysical Research: Atmospheres*, **121**, 7172–7196. URL: http://doi.wiley.com/10.1002/2015JD024722.

Tadono, T., Ishida, H., Oda, F., Naito, S., Minakawa, K. and Iwamoto, H. (2014) Precise Global DEM Generation by ALOS PRISM. *ISPRS Annals of the Photogrammetry, Remote Sensing and Spatial Information Sciences*, **II-4**, 71–76. URL: https://isprs-annals.copernicus.org/articles/II-4/71/2014/.

Takougoum Sagang, L. B., Favrichon, S., Dalagnol, R., Ordway, E. M., Medjibe, V., Manfoumbi, F., Obame, C., Wagner, F., George-Chacon, S., White, L. and Saatchi, S. (2024) Unveiling spatial variations of high forest live biomass carbon stocks of Gabon using advanced remote sensing techniques. *Environmental Research Letters*, **19**, 074038. URL: https://iopscience.iop.org/article/10.1088/1748-9326/ad5572.

Tang, H., Stoker, J., Luthcke, S., Armston, J., Lee, K., Blair, B. and Hofton, M. (2023) Evaluating and mitigating the impact of systematic geolocation error on canopy height measurement performance of GEDI. *Remote Sensing of Environment*, **291**, 113571. URL: https://linkinghub.elsevier.com/retrieve/pii/S0034425723001220.

Taylor, P., Asner, G., Dahlin, K., Anderson, C., Knapp, D., Martin, R., Mascaro, J., Chazdon, R., Cole, R., Wanek, W., Hofhansl, F., Malavassi, E., Vilchez-Alvarado, B. and Townsend, A. (2015) Landscape-Scale Controls on Aboveground Forest Carbon Stocks on the Osa Peninsula, Costa Rica. *PLOS ONE*, **10**, e0126748. URL: https://dx.plos.org/10.1371/journal.pone.0126748. Publisher: Public Library of Science (PLoS).

Valle, D., Haneda, L., Izbicki, R., Kamimura, R. A., Pereira De Azevedo, B., Gomes, S. H., Sanchez, A., Silva, C. A. and Almeida, D. R. (2025) Nonparametric quantification of uncertainty in multistep upscaling approaches: A case study on estimating forest biomass in the Brazilian Amazon. *Science of Remote Sensing*, **11**, 100180. URL: https://linkinghub.elsevier.com/retrieve/pii/S2666017224000646.

Vaswani, A., Shazeer, N., Parmar, N., Uszkoreit, J., Jones, L., Gomez, A. N., Kaiser, L. and Polosukhin, I. (2017) Attention Is All You Need. URL: https://arxiv.org/abs/1706.03762. Version Number: 7.

Wagner, F. H., Dalagnol, R., Silva-Junior, C. H. L., Carter, G., Ritz, A. L., Hirye, M. C. M., Ometto, J. P. H. B. and Saatchi, S. (2023) Mapping Tropical Forest Cover and Deforestation with Planet NICFI Satellite Images and Deep Learning in Mato Grosso State (Brazil) from 2015 to 2021.

Remote Sensing, **15**, 521. URL: https://www.mdpi.com/2072-4292/15/2/521.

Wang, X., Cheng, X., Gong, P., Huang, H., Li, Z. and Li, X. (2011) Earth science applications of ICESat/GLAS: a review. *International Journal of Remote Sensing*, **32**, 8837–8864. URL: https://www.tandfonline.com/doi/full/10.1080/01431161.2010.547533.

Weiner, J. (2015) Towards an Effective System of Monitoring, Reporting, and Verification. In *Towards a Workable and Effective Climate Regime* (eds. S. Barrett, C. Carraro and De Melo, Jamie), 183–200. London: Centre for Economic Policy Research. OCLC: 946211319.

Wenger, S. J. and Olden, J. D. (2012) Assessing transferability of ecological models: an underappreciated aspect of statistical validation. *Methods in Ecology and Evolution*, **3**, 260–267. URL: https://besjournals.onlinelibrary.wiley.com/doi/10.1111/j.2041-210X.2011.00170.x.

White, J. C., Wulder, M. A., Hobart, G. W., Luther, J. E., Hermosilla, T., Griffiths, P., Coops, N. C., Hall, R. J., Hostert, P., Dyk, A. and Guindon, L. (2014) Pixel-Based Image Compositing for Large-Area Dense Time Series Applications and Science. *Canadian Journal of Remote Sensing*, **40**, 192–212. URL: http://www.tandfonline.com/doi/full/10.1080/07038992.2014.945827.

Williams, M. L., Mitchell, A. L., Milne, A. K., Danaher, T. and Horn, G. (2022) Addressing critical influences on L-band radar backscatter for improved estimates of basal area and change. *Remote Sensing of Environment*, **272**, 112933. URL: https://linkinghub.elsevier.com/retrieve/pii/S0034425722000475.

Woodcock, C. E., Loveland, T. R., Herold, M. and Bauer, M. E. (2020) Transitioning from change detection to monitoring with remote sensing: A paradigm shift. *Remote Sensing of Environment*, **238**, 111558. URL: https://linkinghub.elsevier.com/retrieve/pii/S0034425719305784.

Woudenberg, S. W., Conkling, B. L., O'Connell, B. M., LaPoint, E. B., Turner, J. A. and Waddell, K. L. (2010) The Forest Inventory and Analysis Database: Database description and users manual version 4.0 for Phase 2. *Tech. Rep. RMRS-GTR-245*, U.S. Department of Agriculture, Forest Service, Rocky Mountain Research Station, Ft. Collins, CO. URL: https://www.fs.usda.gov/treesearch/pubs/37446.

Zeng, Y., Chen, X., Zhang, Y., Bai, L. and Han, J. (2019) Dense-U-Net: densely connected convolutional network for semantic segmentation with a small number of samples. In *Tenth International Conference on Graphics and Image Processing (ICGIP 2018)*, vol. 11069, 110692B. International Society for Optics and Photonics. URL: https://www.spiedigitallibrary.org/conference-proceedings-of-spie/11069/110692B/Dense-U-Net--densely-connected-convolutional-network-for-semantic/10.1117/12.2524406.short.

Zhang, Y., Liang, S. and Yang, L. (2019) A Review of Regional and Global Gridded Forest Biomass Datasets. *Remote Sensing*, **11**, 2744. URL: https://www.mdpi.com/2072-4292/11/23/2744.

Zhu, X., Nie, S., Wang, C., Xi, X., Lao, J. and Li, D. (2022) Consistency analysis of forest height retrievals between GEDI and ICESat-2. *Remote Sensing of Environment*, **281**, 113244. URL: https://linkinghub.elsevier.com/retrieve/pii/S0034425722003509.

Zhu, Z. and Woodcock, C. E. (2014) Continuous change detection and classification of land cover using all available Landsat data. *Remote Sensing of Environment*, **144**, 152–171. URL: https://linkinghub.elsevier.com/retrieve/pii/S0034425714000248.

Provider	Total Area (km^2)
USGS (3DEP)	1,791,493
ICSM (ELVIS)	612,435
INPE (Ometto et al., 2023)	372,231
Ontario (GeoHub)	330,481
Finland (NLS)	181,240
OpenTopography	155,956
NASA (GSFC; CMS; LVIS)	109,689
British Columbia (LidarBC)	75,874
New Brunswick (GeoNB)	66,981
Estonia (LSDB)	56,729
France (Geoservices)	55,372
Netherlands (GeoTiles)	47,676
Latvia (LGIA)	38,150
NEON	37,055
UK (DEFRA)	35,128
CEDA (Disney et al., 2018)	1,009

TABLE 2 Airborne LiDAR data sources used to develop the Forest Carbon Diligence forest structure and time series models.

A | APPENDIX: SOURCE DATA

A.1 | AIRBORNE LiDAR DATA

Airborne LiDAR data were accessed from a variety of publicly available sources, provided under open licenses for use (Table 2). Area estimates represent the total area of data processed and available in the processed LiDAR data catalog.

Provider	Wood density source	Plot count	Precise geolocation	Size (m^2)
USFS FIA	Provided	339,247	No	672
France NFI	BIOMASS	39,056	No	707
Italy NFI	BIOMASS	6,893	No	531
NEON	BIOMASS	6,198	Yes	100 to 400
Mexico NFI	GWD Database	1,675	Yes	1600
Forest Observation System	Provided	1,260	No	2500 to 10000
Barro Colorado Island 50ha	BIOMASS	1,250	Yes	400
Para Brazil, CMS	BIOMASS	756	Yes	400
SWAMP	GWD Database	161	Yes	154 to 314
AfriSAR	Provided	120	Yes	2500
TropSOC	Provided	78	Yes	1600

TABLE 3 Sources of field estimates of wood density, Lorey's height, AGB, and other plot-level measurements.

A.2 | FIELD PLOT DATA

Field inventory data on wood density ($g \cdot cm^{-3}$) were compiled from a series of public sources with varying levels of completeness. If plot-level means were provided, those values were used. When stem-level data were available, plot-level basal area-weighted means were calculated. When wood density was not provided directly, stem-level wood densities were estimated via species-specific or genus-specific values of wood density using the R BIOMASS package and the Global Wood Density (GWD) Database (Chave et al., 2009; Réjou-Méchain et al., 2017).

US-FIA data were processed using the rFIA package (Stanke et al., 2020). NEON data were processed using the neonstore, geoNEON, and neonUtilities R packages (Lunch et al., 2024; Boettiger et al., 2025; National Ecological Observatory Network, 2025).

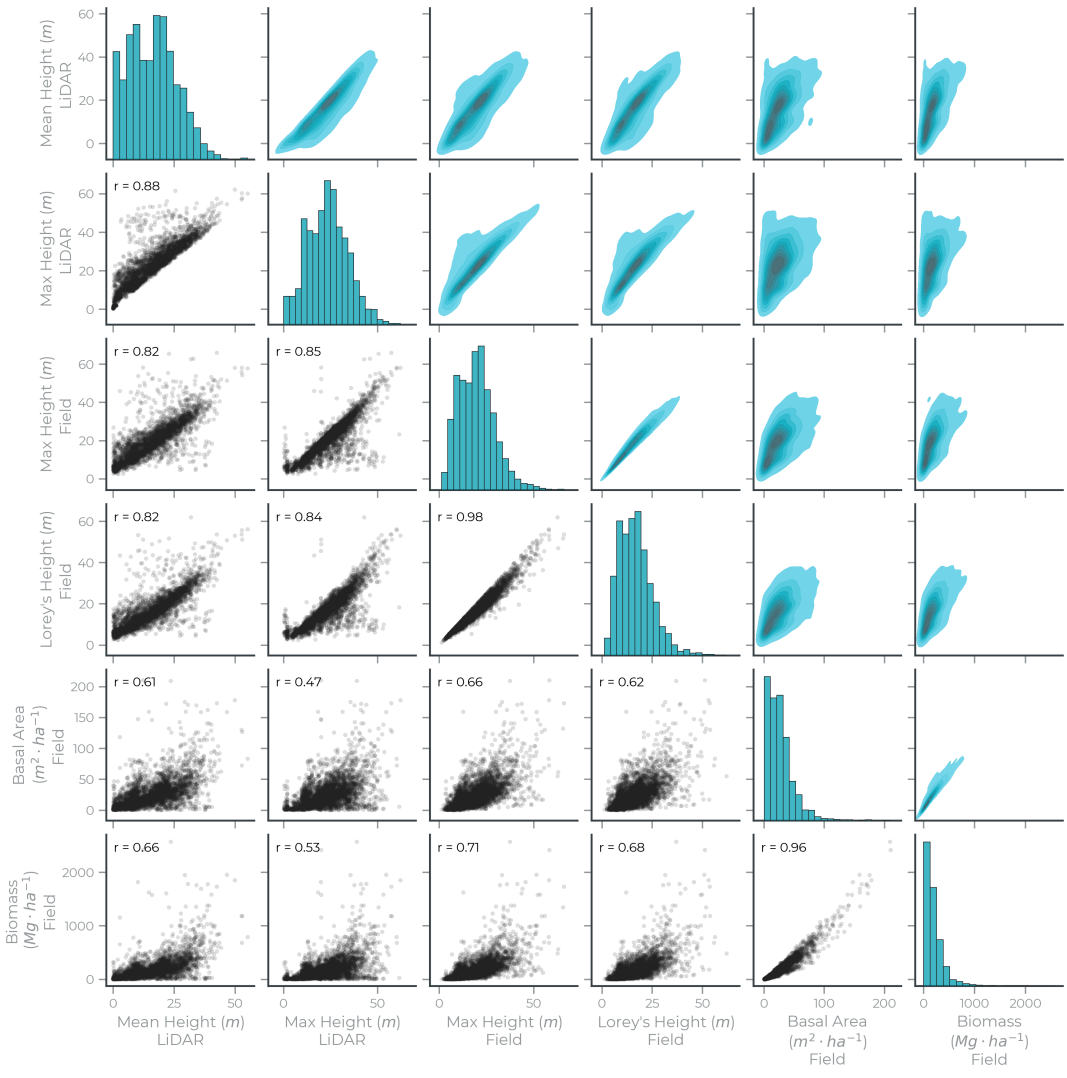

FIGURE 17 Pair plots showing correlations between field- and LiDAR-derived metrics of forest structure over the NEON field sites with coincident LiDAR coverage. Scatter plots in the lower left quadrants quantify correlations with Person's r. Each point represents one plot-year measurement, as plots can be re-surveyed in the field and with LiDAR. Histograms along the diagonal show the distributions of each variable. The upper right quadrant shows kernel density estimates for each pair of variables.

B | APPENDIX: METHODS

B.1 | CANOPY HEIGHT ESTIMATION METHODS

There are multiple methods for quantifying canopy height at the plot level in the field and with airborne LiDAR. In order to select which LiDAR derived metric Diligence would report, correlations were evaluated between multiple canopy height metrics, basal area, and aboveground biomass (Fig. 17). These data were extracted from temporally matched field and LiDAR observations from NEON, providing a dense collection of observations across ecological gradients in North America.

Mean canopy height was selected as the LiDAR metric because it showed higher correlations with both basal area ($r = 0.61$) and aboveground biomass ($r = 0.66$) compared to maximum canopy height ($r = 0.47$, $r = 0.53$ respectively). LiDAR mean canopy height and Lorey's height are comparable in their correlations to basal area and biomass. This is mechanistically plausible because high-resolution height rasters compute discrete height estimates for every pixel in an area, including parts of the crown outside of the peak, and computing the mean over a plot implicitly weights by crown area.

B.2 | SPACEBORNE LiDAR WAVEFORM PROCESSING

GEDI L4A observations were accessed from product version 2.1 (Dubayah et al., 2022b). The following filters were applied to the GEDI L4A observations:

- Low quality observations were removed using the filter `l4_quality_flag = 1`.
- Observations over persistent water were removed using the filter `landsat_water_persistence > 10`.
- Non-degraded geolocations were retained, filtered using `degrade_flag = 0`.
- Sun angle was used to retain nighttime observations, as solar radiance increases noise in ground detections using the filter `solar_elevation < 0` (Liu et al., 2021).
- Only power beams were retained, as coverage beams underestimate canopy height on average (Fayad et al., 2022).
- Terrain data was used to retain observations with `slope < 30`, as canopy height is overestimated on steep slopes (Kutchartt et al., 2022).
- Locations with high geolocation error were identified and removed using temporal clustering (Tang et al., 2023).

Additional tile-level, cluster-based filtering was applied to remove time periods with outliers. First, the GEDI L2A RH98 value for each L4A shot was obtained. Then, for each tile, shots were assigned a cluster ID based on time differences between consecutive shots. The first shot was assigned to cluster one. For the remaining shots in the tile, if the time difference between shot $_i$ and shot $_{i+1}$ was less than one hour, then shot $_{i+1}$ was assigned to the same cluster as shot $_i$. Otherwise shot $_{i+1}$ was assigned to a new cluster.

Next, Diligence canopy height values – produced independently of GEDI data – were extracted and the median RH98 was calculated for each 1 m vertical height bin. A shot was considered an outlier if the RH98 value was ten times greater than the median RH98 for the canopy height bin, or if RH98 exceeded 100 m. Clusters of shots containing three or more outliers were removed, followed by filtering of outlier shots that exist in retained clusters.

Altogether, GEDI filtering retained 30% of the 1,977 million ingested L4A shots, resulting in a dataset of just over 586 million shots.

Estimates of aboveground biomass derived from ICESat-2 were also ingested, providing spatial coverage over high latitude forests outside of the bounds of GEDI data (Montesano et al., 2024). ICESat-2 data do not contain precise shot-level collection time information, so we use independent point-wise outlier detection and filtering, again removing $RH98 > 100$ or $RH98 > 10x$ median RH98 for a given canopy height with each tile. Filtering retained the vast majority of ICESat-2 data, removing only 1,000 of the 15 million ingested waveforms.

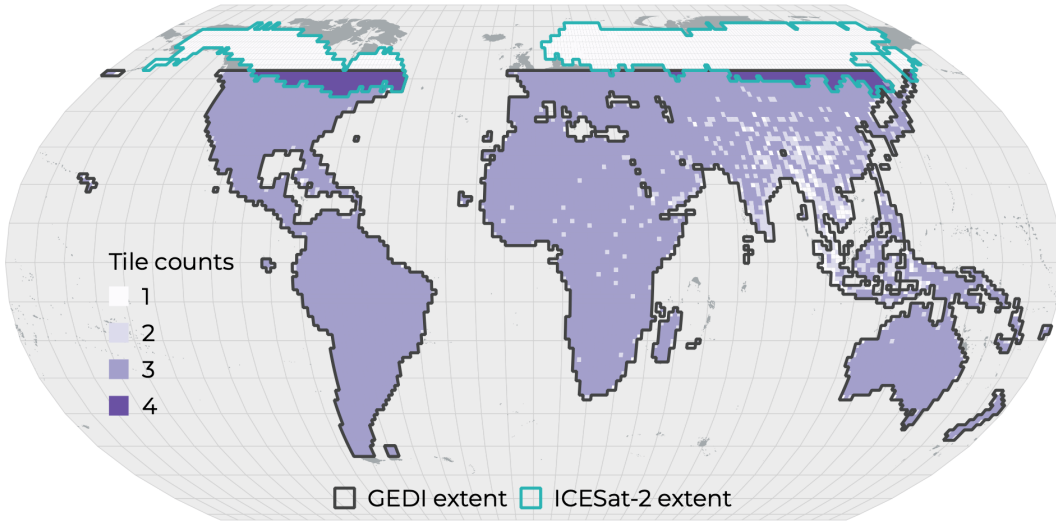

FIGURE 18 Geographic coverage and tile counts for spaceborne LiDAR observations. Observations were quality filtered and organized by tile ID and year. ICESat-2 data were provided for one year, overlapping in coverage with GEDI in parts of North America and Asia. GEDI data provides coverage over multiple years, though some tiles may not include data for every year due to quality filtering. Steep slopes and cloudy conditions reduced coverage in the Himalayas, for example.

Finally, spatially balanced random sampling was used to reduce the impact of over-sampled regions, retaining up to 5,000 randomly selected waveforms per year per tile for each dataset. This resulted in a final dataset size of 81.6 million waveforms.

B.3 | CUSTOM CLOUD MASKING

All cloud classification models balance omission and commission errors (Skakun et al., 2022). During data preprocessing, the Landsat cloud masks from FMask were qualitatively found to show higher omission rates than the Sentinel-2 masks (i.e., more clouds were labeled as clear). The Diligence product prioritized a more inclusive cloud mask, decreasing omission errors at the expense of increasing commission errors. This was achieved by creating an ensemble masking approach.

First, a series of spectral indices and thresholds defined by Sun et al. (2016) were calculated. For each pixel, 11 threshold values were computed, and the pixel-wise average of these binary threshold scores was used as a cloud fraction score. Second, a custom Naive Bayes classifier was fitted using PCA-transformed reflectance data and a series of manually labeled cloud spectra. These labeled spectra were selected ad hoc from a series of scenes where FMask omissions rates were high. The balanced accuracy and F1 scores for this model were 0.87 each, though this number should not be interpreted as globally representative since the sample size was small and not systematic. Third, the pixel-wise average of the cloud fraction score and the classifier prediction probability score was calculated, and pixels with scores >0.5 were labeled as clouds in addition to the pixels labeled by FMask.

Additional thresholds were used to remove cloud shadows and atmospheric haze. Cloud shadows were masked based on the overall brightness of a pixel. Brightness was estimated by computing the average sur-

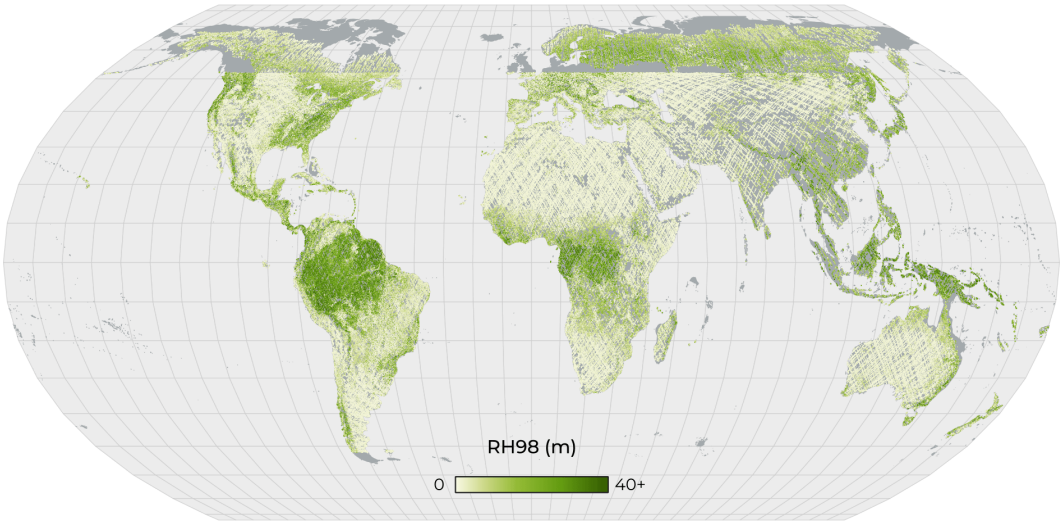

FIGURE 19 Random geographic sample of 1 million RH98 observations.

face reflectance of the green, red, SWIR-1 and SWIR-2 bands, and pixels with <3% average reflectance were flagged as shadow. The blue band was excluded to minimize the influence of residual atmospheric haze. The near infrared band was excluded to minimize strong near infrared scattering from adjacent sunlit canopies (Holben and Fraser, 1984). Haze was classified using the aerosol optical depth (AOD) scores estimated by FORCE, which is a unitless metric. Pixels with scores >0.3 were flagged as moderate haze, and pixels with scores >0.45 were flagged as high haze.

This multistep cloud classification method imposed stricter pixel inclusion thresholds but greatly reduced cloud, shadow, and haze coverage in the downstream mosaics.

B.4 | BEST PIXEL COMPOSITE SCORES

Best pixel algorithms compute a series of pixel-level quality metrics, which are used to rank which pixel will be selected for the final mosaic. The algorithm for this product ranked pixels to maximize similarity in observation conditions, preferring well-illuminated, leaf-on, cloud-free measurements. These criteria were adapted from (White et al., 2014), which established a scoring method specific to Canada. These rules were modified to match the sensors included in this analysis and to better generalize across latitudes. The following scores were computed for each pixel in each scene:

Solar elevation score. Canopy reflectance is highly influenced by observation and illumination geometry, and normalizing solar elevation improves optical estimates of forest structure (Dalagnol et al., 2023). Latitudes near the poles also include days with very low sun angles during satellite overpasses, which should be excluded from analysis. The solar elevation score was calculated by scaling the observed solar elevation to a 0-1 range, normalized from 20° to 72.5°. Annual solar elevation trends and their normalized scores are shown in Fig. 20.

Day of year score. The phenology of photosynthesis roughly follows solar illumination patterns, where growth rates typically increase with warming temperatures in spring, driven in part by rising mid-day solar elevation (Kump et al., 2010). But ranking by solar eleva-

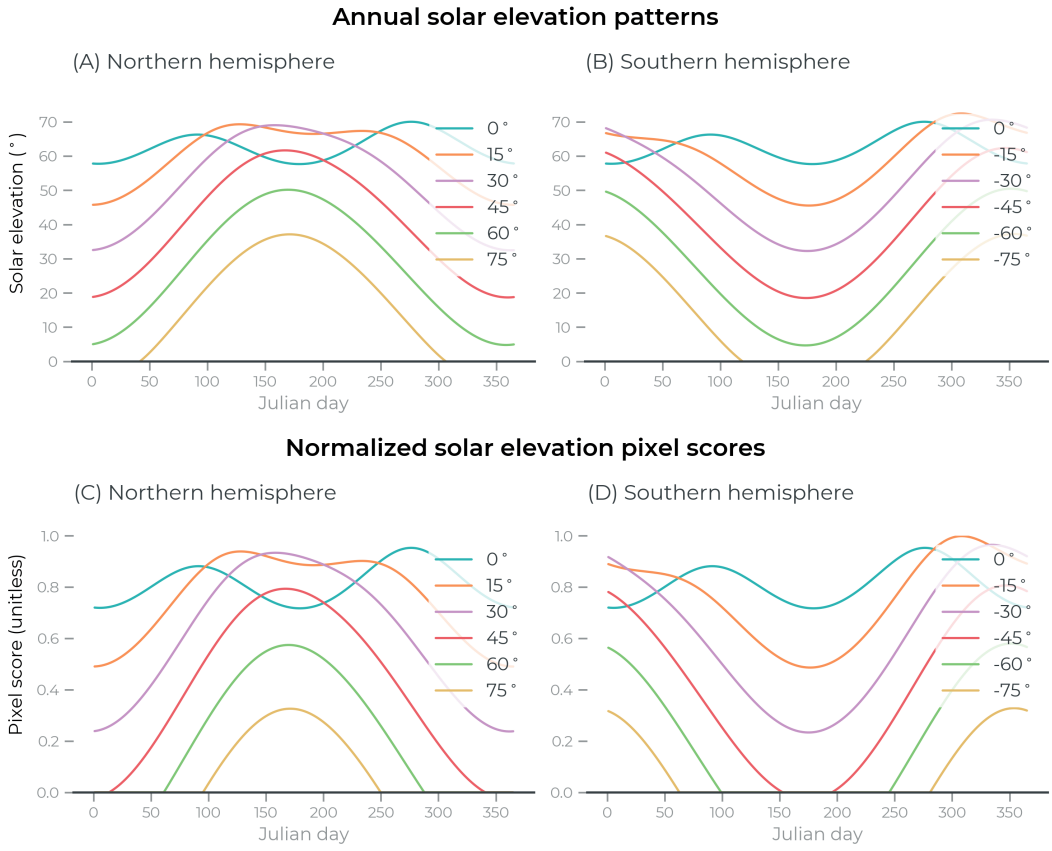

FIGURE 20 Top: modeled solar elevation across latitudes in the (A) northern and (B) southern hemispheres. Bottom: normalized solar elevation scores for these same collection latitudes in (C) northern and (D) southern hemispheres. All plots were generated using a fixed longitude (−63°) and during the nominal Sentinel-2 overpass time (10:30 am Mean Local Solar Time)

tion alone does not necessarily guarantee leaf-on conditions. Solar elevation trends are cyclical, meaning sun angles can match during peak spring greenness and fall senescence.

The day of year score represents a ranking for expected peak greenness, which varies by latitude. For each latitude, a normal distribution is initialized, specifying the width of the distribution in days and the peak start date. Distribution width increases closer to the equator, specifying a longer period of expected peak greenness since many tropical ecosystems are typically evergreen. The peak start date was specified to match expected spring peak dates: March for the northern hemisphere, October for the southern hemisphere. These estimates are general heuristics, and were not empirically fitted to match observed green-up patterns. Example day of year scores are shown in Fig. 21.

Sensor score. Sentinel-2 observations were ranked higher than Landsat observations. Sentinel-2 data are provided at higher nominal resolution and resampled to 30m, which increases measurement signal (Campbell, 2011). Residual cross-track BRDF effects were lower for Sentinel-2 following normalization by FORCE (Frantz, 2019), and the quality of the cloud mask was found to

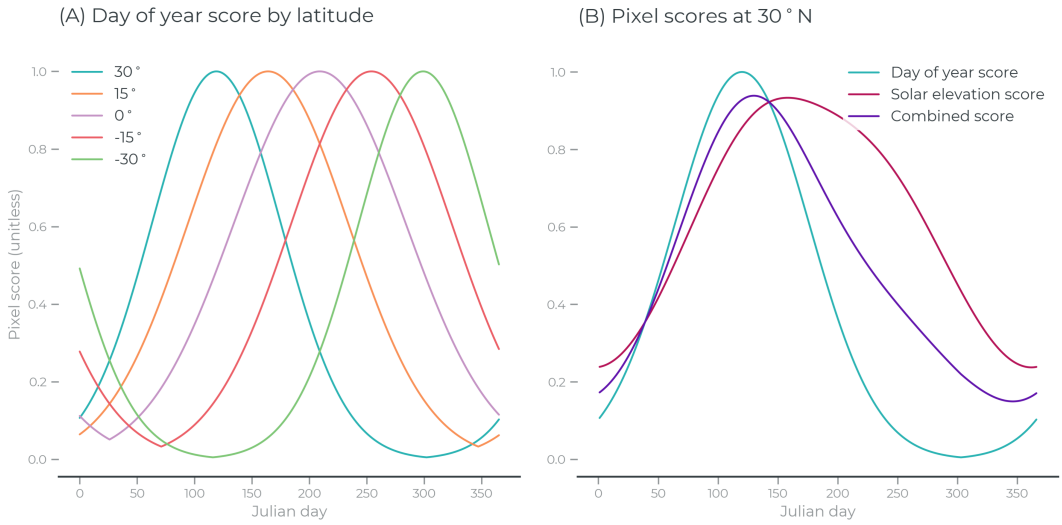

FIGURE 21 (A) Day of year scores for a gradient of latitudes show the expected dates of peak greenness from the northern to southern hemisphere. (B) The solar elevation score and day of year score for 30° *N* are jointly plotted to illustrate how these scores combine to prioritize consistent illumination conditions and leaf on conditions.

be higher (Frantz et al., 2018). Unmasked smoke and haze was found to be more common in Landsat scenes. The sensor score applied to Sentinel-2 scenes was 1.0, while Landsat scenes were assigned a score of 0.25.

Clear observation mask. Pixels flagged as nodata, cloud, cirrus, shadow, or high haze in the scene mask were removed from analysis (Appendix 2.2). A radial buffer of 60 *m* was applied around cloud detections, and a buffer of 120 *m* was applied around cirrus detections. Pixels within these buffer radii were also masked from the analysis.

Final score. The annual surface reflectance mosaics were processed on a per-quad basis, which iterated over all scenes that intersected a quad within that year. Pixel scores for each scene were calculated as the average of the solar elevation, day of year, and sensor scores. The mosaic was populated with the surface reflectance data from the highest ranking pixel scores as each scene was processed. The pixel scores themselves, as well as the day of year for the top ranked pixel, were both retained as QA layers.

B.5 | WOOD DENSITY MODEL

Global estimates of wood density were generated at 1 km resolution via a gradient boosted regression model. Field-estimated wood density was the response variable, and principal component-transformed climate, plant trait, topography, and soils data were the feature variables.

396,694 publicly-accessible field inventory plots were used for training, including data from national forest inventories, ecological monitoring networks, research consortiums, and open data repositories (Appendix A.2). Climate data were sourced from WorldClim 2 (Fick and Hijmans, 2017). Plant functional trait data were sourced from Moreno-Martinez et al. (2018). Topography data were sourced from the Copernicus GLO-30 Height Above Nearest Drainage product (Johnson et al., 2019). Soil data were sourced from SoilGrids 2.0 (Poggio et al., 2021). To address covariance within the feature data, the inputs were normalized then transformed using principal component analysis.

A gradient boosting regression tree model was fitted using the PCA components and strong L2 regularization,

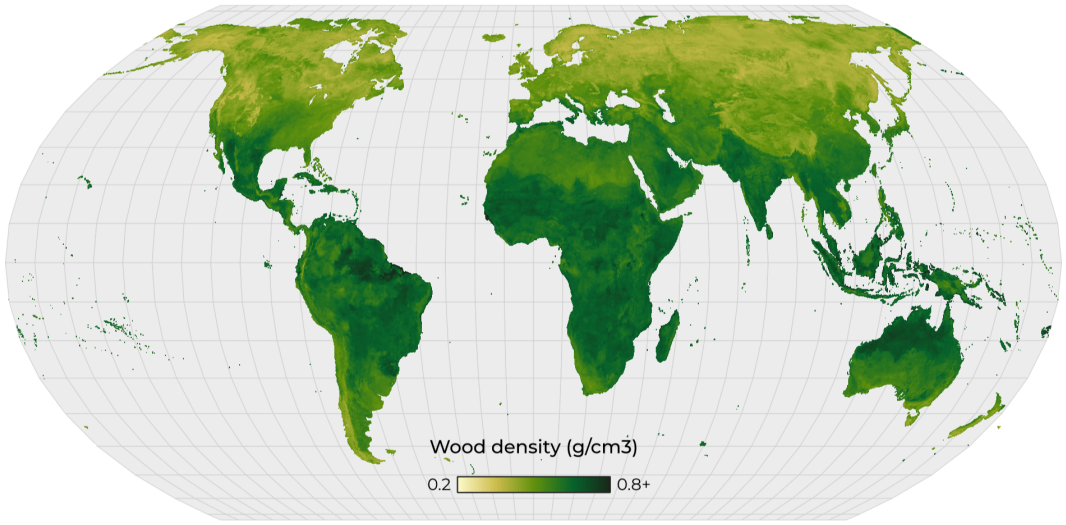

FIGURE 22 Global map of community-level wood density. Predictions were generated for the full terrestrial surface regardless of tree density, as these predictions best represent bioclimatic-driven wood density estimates instead of species assembly-driven estimates.

techniques intended to minimize prediction bias and reduce overfitting (Bühlmann and Yu, 2003; **?**). To reduce the sample bias introduced by plot count differences across datasets, inverse frequency sample weights were computed based on the frequency of samples from each source. This was designed to normalize the contributions from each field dataset. Models were fit using spatially explicit leave-one-group-out cross validation, where groups were specified using unique IDs from the H3 hierarchical hexagonal grid system.

Cross-validation scores show moderate performance for local-scale prediction ($r^2 = 0.06$, $RMSE = 0.21\ g \cdot cm^3$, $MAE = 0.17\ g \cdot cm^3$). The low but positive r^2 score indicates the model can effectively predict the mean but not explain the variance in the response variable, resulting in generally plausible global performance (Fig. 22). This might be interpreted to mean that $1\ km$ features are effective at capturing the macro-ecological drivers of wood density variation, but not for capturing local-scale variation. Nearby field plots often contain species assemblages with large differences in wood density that would not be locally explained by climate, soil, or topography, but might be with finer-scale plant trait data (Jucker et al., 2018).

C | APPENDIX: RESULTS

C.1 | MODEL EVALUATION

C.1.1 | TEMPORAL CONSISTENCY

Repeat NEON LiDAR collections permit comparisons of forest structure estimates over time. To qualitatively evaluate how observed and estimated canopy height varies over time, site-level averages were calculated at NEON sites with repeat lidar coverage. Site level mean height is shown in Figure 23. Some sites show consistent values (MCRA, TEAK), whereas others show higher year-to-year variation in Diligence predictions (e.g., SOAP). For some sites, consistent biases can be seen for all years where Diligence predictions are systematically low (SERC, UNDE), or systematically high (RMNP, NIWO).

Similar relationships are observed between observed and estimated mean canopy cover at the site level (Fig. 24). For instance, many time series align well with observed values (WREF, SERC), whereas others show high variation in Diligence predictions due to variation in the satellite observation conditions (SJER). As with mean height, some sites show biases in mean canopy cover, such as systematically high (RMNP) and systematically low estimates (UNDE).

C.1.2 | GEDI L4B CONFIDENCE INTERVAL EVALUATION

The GEDI L4B product provides an estimate of 95% confidence intervals. Hunka et al. (2023) analyzed the fraction of CCI pixels within these confidence intervals to quantify the agreement between products. This analysis was reproduced, finding higher agreement between Diligence and GEDI (Figure 25).

C.1.3 | GEDI L4B ONE-DEGREE RMSE EVALUATION

Although there is strong agreement between Diligence and GEDI L4B at the 1° scale (r = 0.98, $bias$ = −5.0, $RMSE$ = 14.03, MAE = 8.37), there is also spatial variation in agreement between the two datasets. The greatest discrepancies between Diligence and GEDI L4B AGB were observed in southeast Asia, particularly in the island of Papua. Estimates also diverged over major mountain ranges like the Himalayas and Andes, where L4A footprints on steep slopes were filtered out for Diligence but remain in the L4B data. Agreement is consistently high over deserts and sparsely vegetated regions.

C.2 | MODEL INTERCOMPARISON

C.2.1 | NEON SITE-LEVEL CORRELATIONS

Site level relationships between the NEON plots and Diligence AGB values are visualized in Figure 27. Although correlations are positive, most sites show considerably more variation among the plot-level AGB estimates than among the corresponding Diligence AGB estimates. These relationships highlight an important challenge to fine-scale comparisons between field- and satellite-derived AGB estimates. Although Diligence estimates are consistent over time, considerable variation in field-measured carbon over successive visits reduces the level of agreement at the site scale.

C.2.2 | REGIONAL LiDAR SITE-LEVEL CORRELATIONS

Rodda et al. (2024) provided over 1 million *ha* of field calibrated, LiDAR-derived aboveground biomass data. These sites were selected from globally underrepresented regions in Central Africa and South Asia. Correlations for each site at 1 *ha* scale were plotted in Figure 28. These panels show prediction saturation in high biomass forests as well as a systematic negative bias (discussed in Section 3.2.3).

C.2.3 | CARBON OFFSET PROJECT UNCERTAINTY BOUNDS

Residual error rates for each CARB project plotted along with total carbon stocks for each project to show the

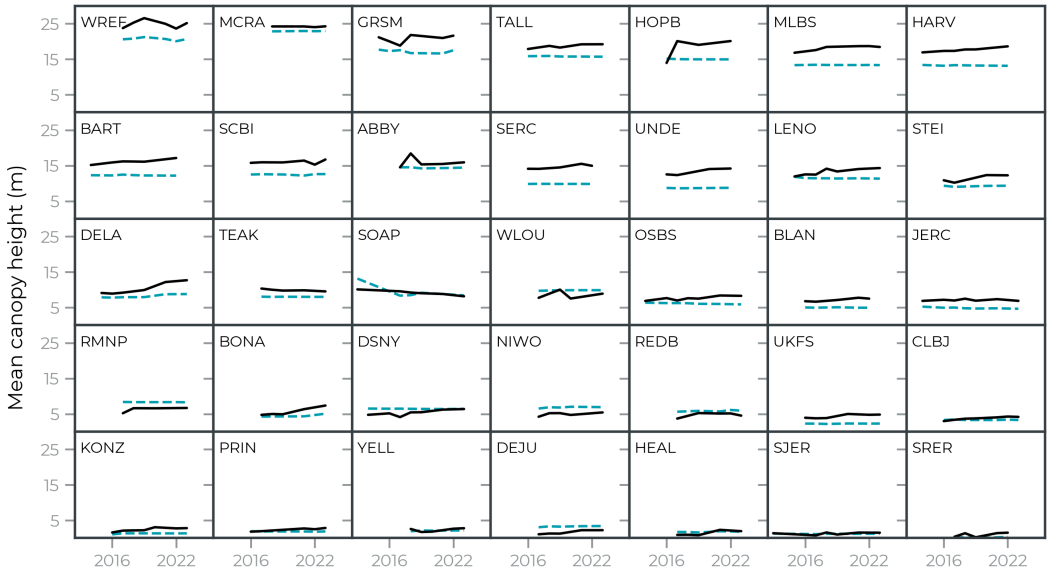

FIGURE 23 Time series of observed (black solid line) and predicted (blue dashed line) site-level mean canopy height (*m*) by year. Values represent averages over the spatial footprint of each NEON site. Panels are labeled with the four letter NEON site code.

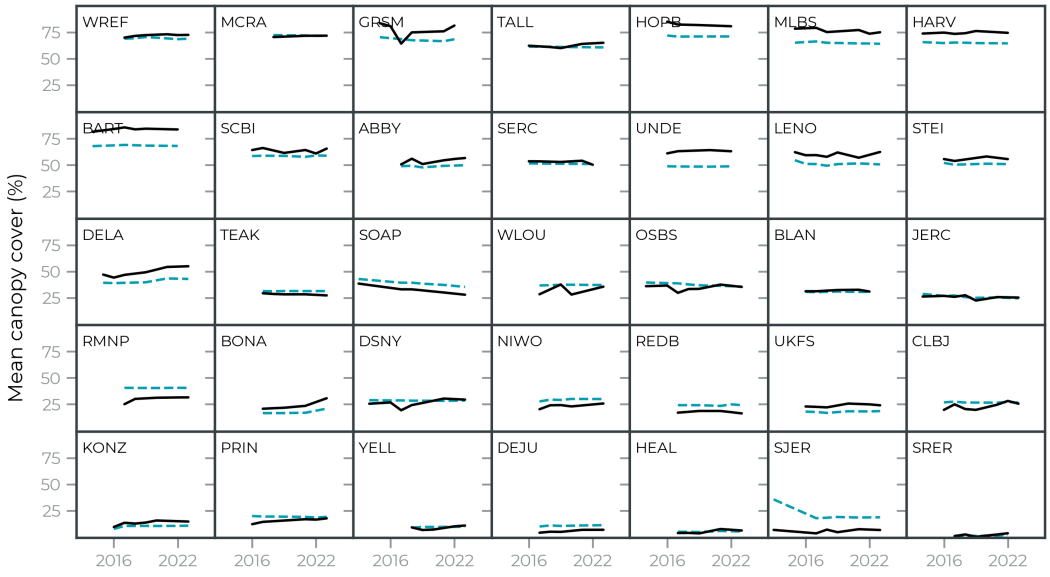

FIGURE 24 Time series of observed (black solid line) and predicted (blue dashed line) site-level mean canopy cover (%) by year. Values represent averages over the spatial footprint of each NEON site. Panels are labeled with the four letter NEON site code.

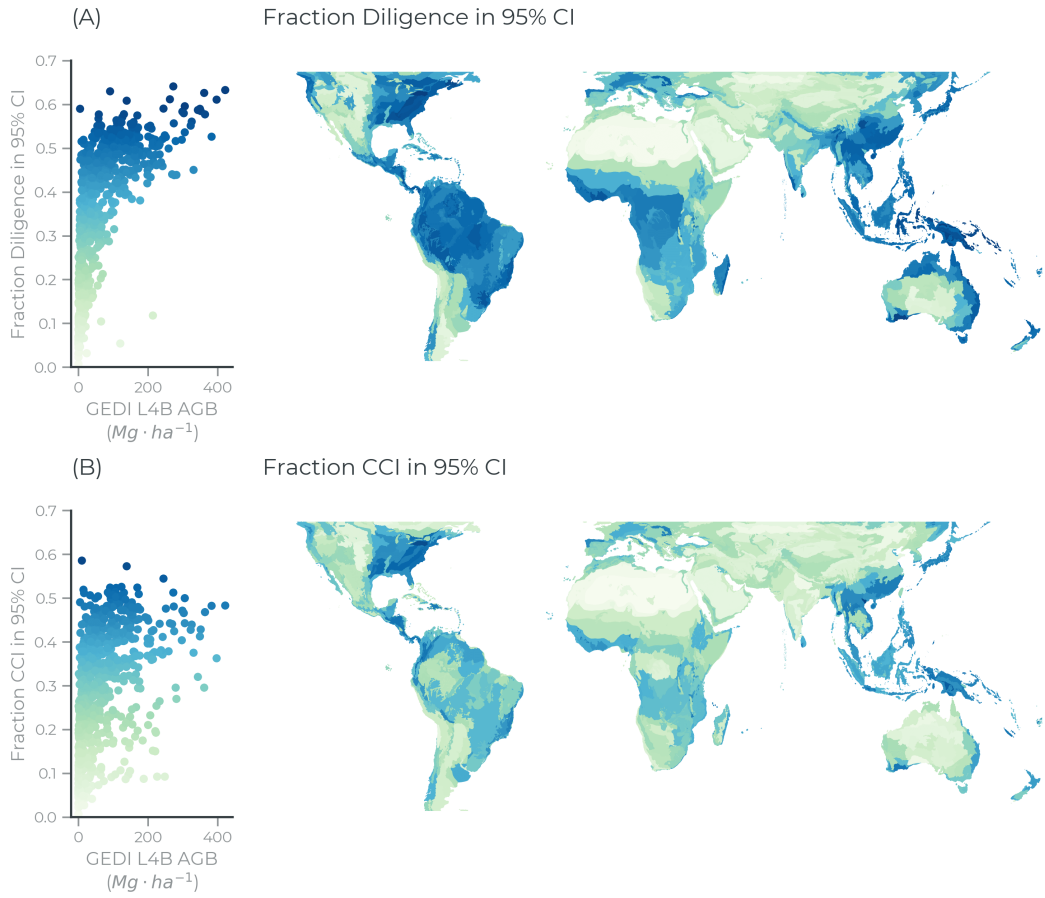

FIGURE 25 Fraction of Diligence (A) and CCI (B) data falling within the 95% CI at the ecoregion level. The scatterplot on the left shows the relationship between ecoregion-mean GEDI L4B AGB (x-axis) and the fraction of Diligence or CCI estimates within the 95% CI from GEDI L4B (y-axis). The right side of the plot shows a map of this fraction, following the same color map.

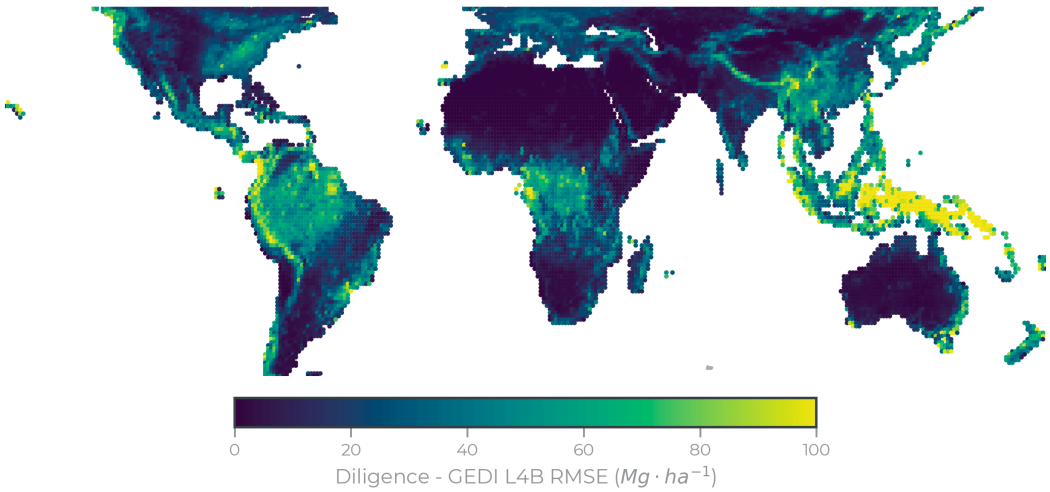

FIGURE 26 Root mean squared error of GEDI L4B aboveground biomass data for 1° grid cells. Pixel-level squared errors were computed for each 1 km grid cell with L4B data, then the square root was computed after average resampling the squared errors to 1°.

fraction of projects within ±25% uncertainty (Fig. 29).

FIGURE 27 Site-specific scatterplots showing relationships between plot-level AGBD estimates (x-axis) and Diligence AGBD estimates (y-axis). Four letter NEON site codes are the subplot titles. A dashed 1:1 line, the Pearson correlation coefficient, and mean bias are provided in each subplot.

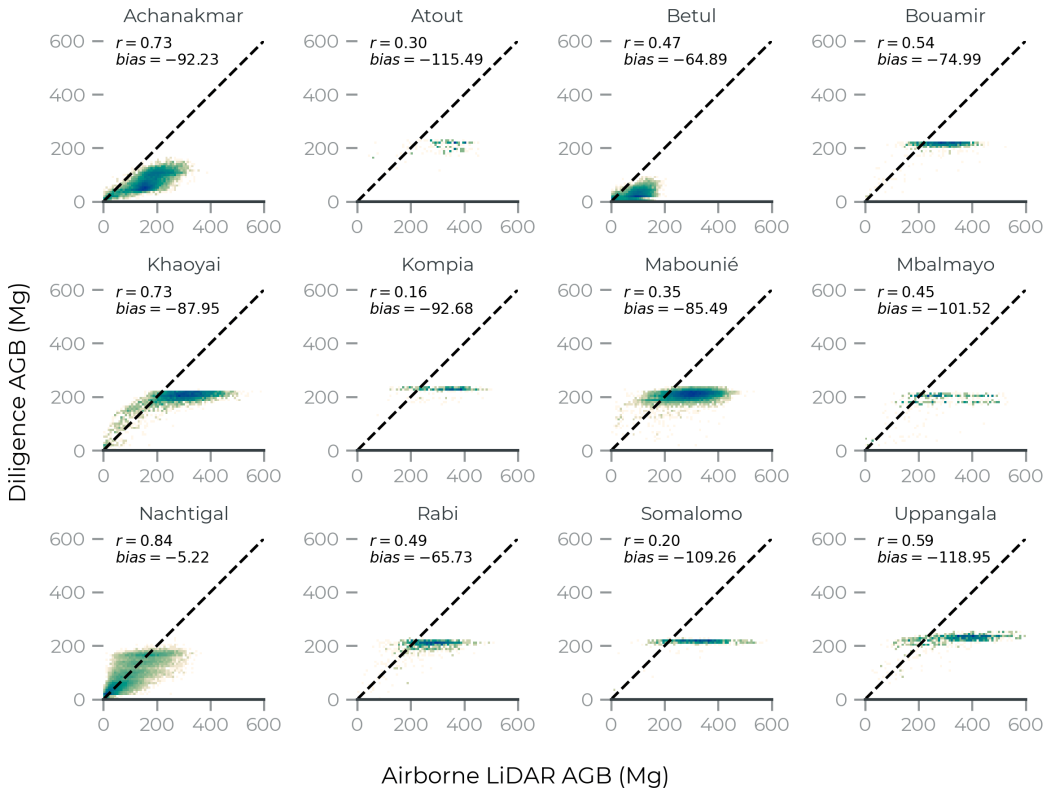

FIGURE 28 Site-specific 2D histograms showing relationships between pixel-level AGB estimates from airborne LiDAR (x-axis; Rodda et al. 2024) and Diligence AGB at 1 *ha* resolution. Site names are the subplot titles. A dashed 1:1 line, the Pearson correlation coefficient, and mean bias are provided in each subplot.

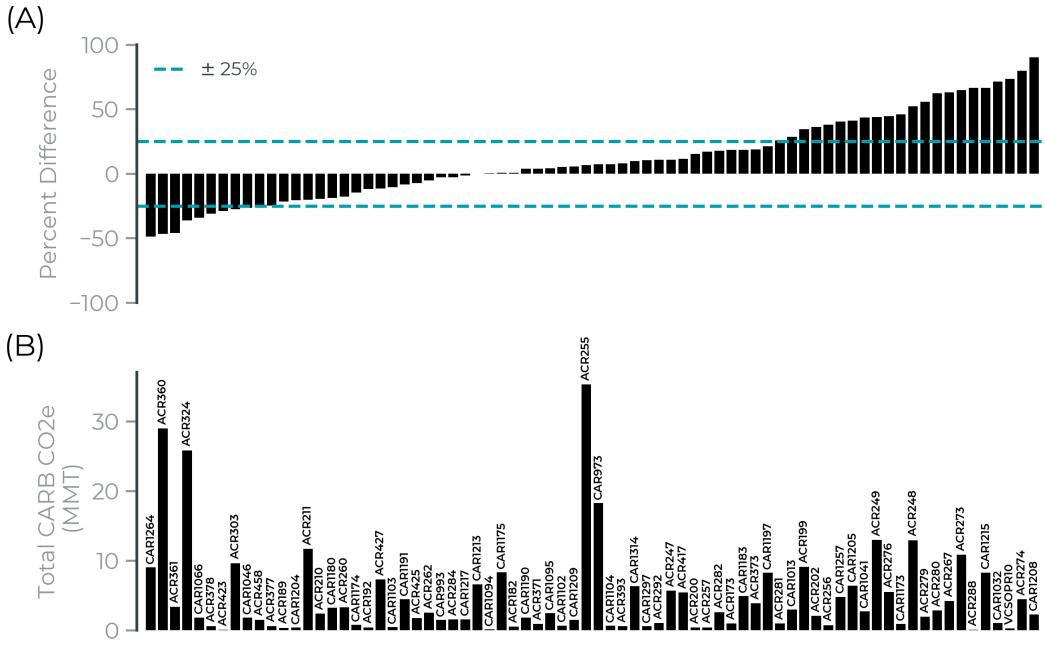

FIGURE 29 (A) Percent difference between Diligence and CARB field-derived total stocks for each project, where negative percentages indicate an underestimate and positive percentages indicate an overestimate by Diligence compared to CARB. Dashed blue lines denote a ±25% difference. (B) CARB field-derived total carbon stocks for each project. Each bar is labeled with the project ID.

Country	ISO3	FAO AGBD ($Mg \cdot ha^{-1}$)	Diligence AGBD ($Mg \cdot ha^{-1}$)	GEDI AGBD ($Mg \cdot ha^{-1}$)	Forest cover (%)	Area (km^2)
Algeria	DZA	0.24	0.49	0.97	0.8	2,308,010
Andorra	AND	52.43	52.76	80.72	34	451
Angola	AGO	16.19	29.48	29.28	53.4	1,246,896
Antigua and Barbuda	ATG	38.75	13.21	11.21	18.5	436
Argentina	ARG	19.39	5.13	6.87	10.4	2,779,056
Australia	AUS	14.65	12.45	14.2	17.4	7,688,097
Austria	AUT	81.41	86.29	105.35	47.3	83,947
Bahamas	BHS	20.27	4.7	3.94	50.9	13,377
Bangladesh	BGD	9.09	31.8	35.62	14.5	139,370
Belarus	BLR	67.43	68.56	75.85	43.2	207,069
Belize	BLZ	118.13	82.12	83.73	56	22,041
Benin	BEN	28.79	15.84	18.25	27.8	115,282
Bhutan	BTN	192.53	180.89	205.78	71.5	38,762
Bolivia	BOL	61.59	53.55	60.33	46.9	1,084,352
Botswana	BWA	41.79	4.25	4.17	26.9	577,868
Brazil	BRA	102.15	80.86	79.54	59.4	8,509,120
British Virgin Islands	VGB	50.68	15.96	35.27	24.1	168
Brunei	BRN	178.1	179.29	236.01	72.1	5,777
Bulgaria	BGR	64.73	58.14	64.01	35.9	111,587
Burkina Faso	BFA	10.86	6.23	9	22.7	272,948
Burundi	BDI	13	31.05	33.16	10.9	26,933
Cabo Verde	CPV	10.78	0.46	23.91	11.3	4,091
Cambodia	KHM	31.68	44.8	50.26	45.7	181,694
Cameroon	CMR	114.05	115.69	116.71	43	466,033
Canada	CAN	34.5	25.26	49.43	38.2	9,954,758
Central African Republic	CAF	77.72	73.79	80.51	35.8	620,199
Chad	TCD	3.12	2.86	4.34	3.4	1,269,951
Chile	CHL	53.7	29.57	40.38	24.5	752,381
China	CHN	15.11	30.96	32.37	23.3	9,349,124
Colombia	COL	98.15	104.99	109.13	53.3	1,137,247
Comoros	COM	11.68	66.24	88.51	17.7	1,674
Republic of the Congo	COG	127.76	127.53	143.51	64.3	341,735
Costa Rica	CRI	116.5	123.33	146.06	59.4	51,187
Côte d'Ivoire	CIV	8.43	46.16	47.13	8.9	321,548
Croatia	HRV	60.3	74.19	77.18	34.7	57,065
Cuba	CUB	35.4	24.22	23.42	31.2	110,711
Curaçao	CUW	0.12	8.09	5.28	0.2	437

TABLE 4 Country-level AGBD estimates from FAO, Diligence, and GEDI L4B. This table excludes countries smaller than 150 km^2. Countries with neither Diligence nor GEDI data were also excluded. If only one of Diligence or GEDI was missing, that entry was left blank.

Country	ISO3	FAO AGBD ($Mg \cdot ha^{-1}$)	Diligence AGBD ($Mg \cdot ha^{-1}$)	GEDI AGBD ($Mg \cdot ha^{-1}$)	Forest cover (%)	Area (km^2)
Cyprus	CYP	7.83	18.77	33.17	18.7	5,720
Czechia	CZE	56.6	63.89	77.06	34.7	78,840
North Korea	PRK	31.2	85.55	84.03	50.1	122,703
Democratic Republic of the Congo	COD	128.55	104.5	121.81	55.6	2,328,879
Denmark	DNK	16.93	24.69		15	43,141
Djibouti	DJI	0.22	0.02	2.23	0.3	22,371
Dominican Republic	DOM	36.7	46.35	56.07	44.4	48,092
Ecuador	ECU	89.08	117.86	150.34	50.3	256,348
Egypt	EGY	0.05	0.1	0.34	0	983,791
El Salvador	SLV	32.01	62.82	49.98	28.2	20,423
Equatorial Guinea	GNQ	187.23	198.99	209.81	87.3	26,957
Eritrea	ERI	7.58	0.35	9.54	10.4	120,453
Estonia	EST	65	59.24		56.1	45,494
Swaziland	SWZ	22	21.46	21.86	28.9	17,381
Ethiopia	ETH	18.49	15.92	20.44	15.2	1,129,020
Falkland Islands	FLK	0	0.02	7.71	0	12,390
Fiji	FJI	126.54	127.05	133.05	62.4	18,952
Finland	FIN	44.07	47.53		73.7	336,885
France	FRA	42.69	50.78	62.3	31.5	549,518
French Guiana	GUF	355.36	255.15	283.06	97.4	83,301
French Polynesia	PYF	60.81	0	177.24	40.8	4,030
Gabon	GAB	203.87	192.38	229.78	91.3	264,551
Gambia	GMB	10.02	5.31	12.52	24	10,667
Georgia	GEO	48.47	86.95	94.34	40.6	69,846
Germany	DEU	60.6	64.2	84.07	32.7	357,822
Ghana	GHA	33.92	30.83	28.3	35.1	239,475
Greece	GRC	10.36	42.14	51.6	30.3	132,564
Grenada	GRD	56.95	84.66	99.97	52.1	360
Guadeloupe	GLP	147.67	70.54	71.34	42.6	1,649
Guatemala	GTM	40.84	76.69	83.56	32.9	109,149
Guinea	GIN	33.04	39.34	47.08	25.2	244,815
Guinea-Bissau	GNB	59.15	30.4	42.13	70.4	33,879
Guyana	GUY	466.78	177.91	192.56	93.6	209,743
Haiti	HTI	11.91	21.48	36.64	12.6	27,113
Honduras	HND	60.09	88.15	103.4	56.8	112,292
Hungary	HUN	24.83	35.65	48.51	22.7	93,039
Iceland	ISL	0.12	0.63		0.5	102,220
India	IND	16.67	23.34	27.11	24.3	2,978,346
Indonesia	IDN	87.81	188.8	199.82	49.1	1,890,085
Iran	IRN	9.09	2.32	6.82	6.6	1,621,750
Iraq	IRQ	0.97	0.63	2.55	1.9	436,474

Country	ISO3	FAO AGBD ($Mg \cdot ha^{-1}$)	Diligence AGBD ($Mg \cdot ha^{-1}$)	GEDI AGBD ($Mg \cdot ha^{-1}$)	Forest cover (%)	Area (km^2)
Ireland	IRL	12.67	19.91	34.03	11.4	70,263
Italy	ITA	35.97	50.09	62.51	32.5	300,729
Jamaica	JAM	87.36	77.58	90.23	55.1	11,002
Jordan	JOR	0.62	0.23	1.36	1.1	89,186
Kazakhstan	KAZ	1.06	1.47	3.96	1.3	2,730,539
Kenya	KEN	12.71	10.34	10.59	6.3	585,999
Kyrgyzstan	KGZ	3.41	5.45	24.61	6.9	197,452
Laos	LAO	87.36	122.21	137.03	71.9	229,869
Latvia	LVA	70.28	62.3		54.9	64,710
Lebanon	LBN	8.58	13.74	23.43	14	10,239
Lesotho	LSO	0.84	3.5	18.36	1.1	30,547
Liberia	LBR	162.44	138.81	144.86	79.1	95,920
Libya	LBY	0.06	0.09	0.13	0.1	1,616,051
Liechtenstein	LIE	101.51	78.44	104.22	41.9	160
Lithuania	LTU	47.04	51.49		35.1	65,016
Luxembourg	LUX	65.96	73.39	89.01	36.5	2,582
Madagascar	MDG	34.87	29.74	28.72	21.4	591,443
Malawi	MWI	18.71	22.78	20.99	23.8	117,924
Malaysia	MYS	122.1	159.26	165.24	58.2	329,571
Maldives	MDV	3.69	28.65	19.33	2.7	279
Mali	MLI	5.05	2.05	3.39	10.9	1,251,200
Marshall Islands	MHL	69		45.5	52.2	283
Martinique	MTQ	150.95	73.88	77.59	49.3	1,118
Mauritania	MRT	0.16	0.1	0.34	0.3	1,041,167
Mauritius	MUS	23.72	48.71	35.91	19.1	2,026
México	MEX	17.72	32.33	36.53	33.8	1,951,297
Mongolia	MNG	5.01	3.98	7.62	9.1	1,566,259
Montenegro	MNE	59.56	67.6	84.27	61.5	13,335
Morocco	MAR	5.13	1.88	7.73	12.9	413,477
Mozambique	MOZ	47.37	30.5	33.97	46.7	787,463
Myanmar	MMR	54.87	108.56	122.02	43.7	669,268
Namibia	NAM	5.44	2.29	4.15	8.1	824,056
Nepal	NPL	71.63	86.41	103.07	41.6	147,661
Netherlands	NLD	6.05	26.45	39.21	11	37,686
New Caledonia	NCL	66.93	78.43	85.24	45.8	18,823
New Zealand	NZL	110.7	73.98	87.15	37.6	268,727
Nicaragua	NIC	25.77	63.05	63.46	28.3	128,180
Niger	NER	0.33	0.26	0.67	0.9	1,183,664
Nigeria	NGA	32	15.69	13.36	23.7	908,397
North Macedonia	MKD	28.45	52.71	59.7	39.7	24,910
Norway	NOR	25.7	23.48		40	325,064
Oman	OMN	0.01	0.15	0.6	0	309,121

Country	ISO3	FAO AGBD ($Mg \cdot ha^{-1}$)	Diligence AGBD ($Mg \cdot ha^{-1}$)	GEDI AGBD ($Mg \cdot ha^{-1}$)	Forest cover (%)	Area (km^2)
Pakistan	PAK	3.64	4.1	8.34	4.8	792,380
Panama	PAN	82.25	130.65	130.25	56.7	75,447
Papua New Guinea	PNG	139.35	295.86	272.14	79.2	463,590
Paraguay	PRY	28.31	9.71	7.34	40.5	399,298
Peru	PER	134.37	123.47	128.39	56.5	1,292,460
Philippines	PHL	52.98	99.89	119.31	24.1	295,813
Poland	POL	51.41	59.98	69.1	31	312,401
Puerto Rico	PRI	45.07	61.36	70.14	56	8,970
Qatar	QAT	0	0.27	0.46	0	11,583
South Korea	KOR	84.96	98.64	89.81	64.5	100,519
Moldova	MDA	10.97	15.08	30.54	11.8	33,906
Réunion	REU	49.02	76.68	69.89	39.2	2,513
Romania	ROU	62.49	58.77	71.46	30.1	238,340
Russia	RUS	38.5	38.68	52.35	49.8	16,925,751
Rwanda	RWA	16.34	27.06	28.73	11.2	25,279
Saint Kitts and Nevis	KNA	88.85	41.43	36.91	42.3	267
Saint Lucia	LCA	100.11	92.57	132.59	34	614
Saint Pierre and Miquelon	SPM	1.39	11.75	15.46	5.3	227
Saint Vincent and the Grenadines	VCT	160.36	83.45	130.65	73.2	398
São Tomé and Príncipe	STP	87.85	140.2	219.36	54.1	1,002
Saudi Arabia	SAU	0.12	0.09	0.45	0.5	1,923,052
Senegal	SEN	18.54	4.35	10.84	41.9	196,893
Serbia	SRB	48.87	59.84	68.8	31.1	78,232
Seychelles	SYC	126.6		59.1	73.3	489
Sierra Leone	SLE	28.8	54.84	58.02	35.1	72,600
Singapore	SGP	29.76	42.51	47.23	21.9	695
Slovakia	SVK	68.54	85.21	90.88	40.1	49,097
Slovenia	SVN	155.56	121.17	132.57	61.5	19,956
Solomon Islands	SLB	86.33	318.75	307.43	90.1	28,504
Somalia	SOM	9.77	2.76	3.53	9.5	633,528
South Africa	ZAF	12.04	5.45	8.11	14.1	1,219,705
Spain	ESP	20.77	24.85	32.62	37.2	506,041
Sri Lanka	LKA	26.67	56.75	56.61	33.7	65,839
Sudan	SDN	5.51	1.36	2.42	9.8	1,872,133
Suriname	SUR	353.49	219.54	235.34	97.4	146,426
Sweden	SWE	49.78	45.86		68.7	449,999
Switzerland	CHE	62	63.88	89.41	32.1	41,234
Syria	SYR	1.42	1.07	2.25	2.8	186,929

Country	ISO3	FAO AGBD ($Mg \cdot ha^{-1}$)	Diligence AGBD ($Mg \cdot ha^{-1}$)	GEDI AGBD ($Mg \cdot ha^{-1}$)	Forest cover (%)	Area (km^2)
Thailand	THA	55.43	74.99	82.6	38.9	513,926
Timor-Leste	TLS	92.92	104.21	123.8	61.9	14,917
Togo	TGO	26.89	20.09	22.67	22.2	56,906
Trinidad and Tobago	TTO	40.11	121.97	141.12	44.5	5,160
Tunisia	TUN	2.66	1.74	3.02	4.5	154,869
Turkey	TUR	13.89	22.46	30.38	28.9	780,702
Turks and Caicos Islands	TCA	14.65	1.87	1.52	11.1	991
Uganda	UGA	11.19	19.26	23.95	11.7	241,421
Ukraine	UKR	23.42	30.46	38.25	16.7	601,365
United Arab Emirates	ARE	3.33	0.18	0.43	4.5	71,107
United Kingdom	GBR	15.16	21.92	40.65	13.2	245,237
Tanzania	TZA	25.09	29.64	28.51	51.6	940,533
United States	USA	32.06	43.18	47.1	33.9	9,472,697
Virgin Islands, U.S.	VIR	29.87	20.89	27.95	56.9	362
Uruguay	URY	11.26	7.66	10.86	11.6	177,607
Venezuela	VEN	107.3	84.95	82.33	52.4	912,365
Vietnam	VNM	29.61	73.09	89.47	47.2	329,285
Western Sahara	ESH	1	0	0	2.5	267,327
Zambia	ZMB	26.52	29.91	30.01	60.3	751,176
Zimbabwe	ZWE	42.83	17.63	15.04	45.1	390,039